

NO_x Emissions Constraints from GEMS NO₂ Retrievals: Inversion Methodology and Air Quality Model Evaluation in Bangkok using ASIA-AQ Multi-Platform Observations

Julianna A. Christopoulos¹, Pablo E. Saide^{1,2}, Manas R. Mohanty¹, Nattamon Maneenoi¹, Jhoon Kim³, Laura Judd⁴, Katherine R. Travis⁴, Savitri Garivait^{5,6}, Agapol Junpen^{5,6}, Kazuyuki Miyazaki^{7,8}, Jinkyul Choi^{7,8}, Takashi Sekiya^{9,8}, David Peterson^{10,9}, Theodore M. McHardy^{10,9}, Nicholas Gapp^{11,10}, Jason M. St. Clair^{12,13,11,12}, Erin Delaria^{14,15,13,14}, Glenn M. Wolfe^{12,11}, Abby Sebol^{15,14}, Alessandro Franchin^{16,15}, Changmin Cho^{16,15}, Morgan L. Silverman^{4,17,14,16}, James H. Crawford⁴

¹Department of Atmospheric and Oceanic Sciences, University of California, [Los Angeles](#), Los Angeles, CA, USA

²Institute of the Environment and Sustainability, University of California, Los Angeles, [Los Angeles](#), CA, USA

³Department of Atmospheric Sciences, Yonsei University, Seoul, South Korea

⁴NASA Langley Research Center, Hampton, VA, USA

⁵The Joint Graduate School of Energy and Environment, King Mongkut's University of Technology, Thonburi, Thailand

⁶Center of Excellence on Energy Technology and Environment, PERDO, Ministry of Higher Education, Science, Research and Innovation, Bangkok, Thailand

⁷Jet Propulsion Laboratory ([JPL](#)), California Institute of Technology, Pasadena, [91109](#) CA, USA

⁸[Joint Institute for Regional System Science and Engineering \(JIFRESSE\), University of California, Los Angeles, Los Angeles, CA, USA](#)

^{9,8}Japan Agency for Marine-Earth Science and Technology, Yokohama, Japan

^{10,9}U.S. Naval Research Laboratory, Monterey, CA, USA

^{11,10}Science Applications International Corporation, Monterey, CA

^{12,11}Atmospheric Chemistry and Dynamics Laboratory, NASA Goddard Space Flight Center, Greenbelt, USA

^{13,12}GESTAR II, University of Maryland Baltimore County, Baltimore, USA

^{14,13}ESSIC, University of Maryland, College Park, ~~postal-code~~, USA

^{15,14}Department of Atmospheric and Oceanic Science, University of Maryland, College Park, USA

^{16,15}Atmospheric Chemistry Observations and Modeling Laboratory, NSF National Center for Atmospheric Research, Boulder, CO, USA

^{17,16}Science Systems and Applications, Inc. Hampton, VA, USA

Correspondence to: Julianna A. Christopoulos (juliechristo@g.ucla.edu)

37

38

39

40 **Abstract.** Nitrogen Dioxide (NO₂) is a key component of tropospheric chemistry and air quality, yet large uncertainties persist
41 in regional NO_x emissions across rapidly developing megacities in Southeast Asia. Observations from the Geostationary
42 Emissions Monitoring Spectrometer (GEMS) provide new constraints on anthropogenic NO₂ variability, while the 2024 NASA
43 Airborne and Satellite Investigation of Asian Air Quality (ASIA-AQ) campaign, offers an extensive, independent dataset for
44 model evaluation. Here, we examine air quality in Bangkok using coarse (20 km) and high-resolution (4 km) WRF-Chem
45 simulations during ASIA-AQ. We develop a top-down framework that uses hourly GEMS NO₂ columns to derive constraints
46 on the daytime cycle of NO_x emissions. Emissions are first estimated from GEMS using a Cross-Sectional Flux (CSF) inversion
47 and then incorporated into WRF-Chem through a novel optimization that reshapes the magnitude and daytime structure of
48 NO_x while accounting for lifetime and satellite vertical sensitivity. GEMS-constrained NO_x emissions for March 2024 are
49 estimated to range from 2.7 to 4.3 kT month⁻¹ after accounting for known low biases in the GEMS retrievals. GEMS-
50 constrained NO_x emissions for March 2024 are estimated at 2.7 kT month⁻¹ over Bangkok, approximately 75% lower than
51 EDGAR v5. Re-running WRF-Chem with the updated emissions leads to substantial improvements in modeled NO₂
52 magnitude and temporal variability when evaluated against independent ground-based, Pandora, and airborne measurements.
53 Remaining negative biases are consistent with a systematic low bias in the GEMS v3 NO₂- product product that cannot be
54 diagnosed using satellite data alone, highlighting the importance of multi-platform evaluation using independent observations.
55 Together, these results demonstrate the value of hourly geostationary observations combined with high-resolution modeling
56 as a scalable pathway for improving urban NO_x emissions estimates and air quality simulations in Southeast Asia.

57 1 Introduction

58 The troposphere contains a variety of pollutants and aerosols that degrade air quality and affect human health (Chen and Chen,
59 2021; Fuller et al., 2022; Shetty et al., 2023). Nitrogen oxides (NO_x = NO + NO₂) are primary pollutants with significant
60 variability in space and time (Seinfeld and Pandis, 2016). Information on NO_x sources is crucial in defining its concentration
61 and distribution (Miyazaki et al., 2019). Nitrogen dioxide (NO₂) is fundamental to air quality and atmospheric chemistry, as it
62 is the primary precursor to surface ozone (O₃) and nitrate aerosols (Pörtner et al., 2022) and is independently linked to the
63 development of pediatric asthma (Anenberg et al., 2022). It is thus inherent that NO₂, and its sources, are well quantified and
64 studied to gain insights into its environmental impact.

65

66 Over the past two decades, satellite observations of tropospheric NO₂ have revealed substantial regional variability in
67 emissions, particularly over industrial and urban areas (Goldberg et al., 2024; Park et al., 2025; Rey-Pommier et al., 2025).
68 While strict air quality policies in North America and Europe have resulted in significant NO₂ reductions, many developing

69 regions, especially the megacities of Southeast Asia, have seen increases (Elguindi et al., 2020; Georgoulas et al., 2019;
70 Miyazaki et al., 2017; Park et al., 2025; Sicard et al., 2023). Thailand, for example, has undergone rapid industrialization,
71 urbanization, and economic growth over the past 30 years, with most of this development occurring in the Bangkok
72 Metropolitan Region (BMR) (Thailand Office of the National Economic and Social Development Board, World Bank, 2017)
73 (Uttamang et al., 2018). This has led to increased emissions from vehicular traffic and industrial activity, resulting in a
74 sustained degradation of air quality (Uttamang et al., 2018). Since the mid 1990s, the BMR has frequently exceeded Thailand's
75 National Ambient Air Quality Standards (NAAQS) for particulate matter (PM) ($25 \mu\text{g m}^{-3}$) and O_3 (100 ppb), particularly
76 during the dry season (February-May) (Kumar et al., 2012; Uttamang et al., 2018, 2020, 2023). Within the BMR, there have
77 been initiatives to reduce health impacts and exposure related to $\text{PM}_{2.5}$. For example, the National Agenda Action Plan on
78 "Solving the Pollution Problems of Particulate Matter" motivated implementation measures in transport, industry, and waste
79 sectors (Aung et al., 2025). However, achieving the air quality standard has remained an issue. Modeling studies have shown
80 that O_3 levels typically peak between January and March, coinciding with increased solar radiation, higher temperatures,
81 elevated humidity, and prevailing northeasterly winds during the Northeast monsoon season. These meteorological conditions,
82 combined with rising emissions, often contribute to O_3 pollution episodes in the region (Uttamang et al., 2020). A key limitation
83 of these air quality modeling studies is the uncertainty in bottom-up anthropogenic emissions inventories, which remain a
84 significant source of error. In the BMR, uncertainties in regional emissions can be as large as a factor of 2 or higher (Bond et
85 al., 2004, 2007; Smith et al., 2011; Uttamang et al., 2020). These emissions uncertainties limit our ability to accurately simulate
86 pollutant concentrations and assess the effectiveness of emission control strategies. Thus, to address this issue, new
87 observational capabilities that can directly capture emission variability at fine spatial ($< 10 \text{ km}$) and temporal (hourly) scales
88 are needed.

89
90 We are currently entering a new era of satellite atmospheric composition monitoring with the launch of three geostationary
91 (GEO) imaging spectrometers covering a large component of the Northern Hemisphere. The Geostationary Environmental
92 Monitoring Spectrometer, GEMS (Kim et al., 2020), Tropospheric Emissions: Monitoring of Pollution, TEMPO (Zoogman et
93 al., 2017), and Sentinel-4 (Gulde et al., 2017), now provide unprecedented spatial and temporal resolution of atmospheric
94 constituents. These instruments offer hourly observations that resolve daytime variability of key pollutants, including NO_2 .
95 Until now, most studies of top-down NO_x emissions have relied on once-daily measurements from low Earth orbit (LEO)
96 satellites (i.e., OMI, TROPOMI) requiring assumptions about diurnal emission and chemistry patterns that introduce
97 uncertainties when coupled with chemical transport models, particularly those arising from coarse spatial resolution ($> 20 \text{ km}$),
98 emissions inventories, and chemical mechanisms (Park et al., 2025). Although these measurements have been invaluable for
99 global and long-term NO_x assessments, they cannot fully capture the pronounced sub-daily variability in NO_2 driven by
100 emissions, chemistry, and transport. GEO satellites now provide the capability to directly observe this hourly variability (Park
101 et al., 2025). For example, using 12 km WRF-Chem simulations Hsu et al. (2026) showed that TEMPO-derived top-down NO_x

emissions are broadly consistent with TROPOMI and bottom-up inventories, but noted coarse model resolution (e.g., 12 km) can limit the representation of coastal meteorology and chemical nonlinearity.

GEMS was the first UV-visible hyper-spectrometer in geostationary orbit and was launched on GEO-KOMPSAT-2B on February 18, 2020. GEMS measurements allow the observation of air quality constituents (e.g., NO₂, SO₂, O₃, HCHO, CHOCHO, and aerosols) at a spatial resolution of 3.5 x 7.7 km² at the center of its field of regard and was the first space-based instrument to provide hourly observations of these species. The GEMS field of regard covers 20 countries in Asia, E-W from Japan to India, and N-S from Mongolia to Indonesia (Kim et al., 2020; Park et al., 2025). Recent work has demonstrated the potential of GEMS and air quality models to estimate top-down NO_x emissions over major Asian cities during the summertime (de Foy and Schauer, 2022; Park et al., 2024, 2025). These studies highlight the need for comprehensive validation involving independent observations. The Airborne and Satellite Investigation of Asian Air Quality, ASIA-AQ, has provided an excellent opportunity to conduct extensive validation of air pollutants across multiple Asian megacities, including Bangkok (ASIA-AQ White Paper | ASIA-AQ, 2025).

In this manuscript, we aim to address these gaps specifically near Bangkok, Thailand by deriving emissions and examining fine- (4 km) and coarse- (20 km) resolution Weather Research and Forecasting model coupled with Chemistry (WRF-Chem) simulations driven by them during mid-March 2024. First, we derive daytime hourly NO_x emissions from GEMS over the BMR in March 2024. Next, we use the GEMS emissions to constrain hourly model emissions through a novel optimization technique. To conclude, we assess model performance using GEMS and independently with ground-monitor information, Pandora site measurements, and airborne measurements collected during the ASIA-AQ campaign.

2 Model configuration and experimental design

To simulate air quality over the BMR, we use a regional simulation of WRF-Chem v4.2.2 in a research configuration (Table 1; Fig. 1) (Agarwal et al., 2024; Anav et al., 2024; Gao and Zhou, 2024; Skamarock et al., 2019). The model setup follows previous WRF-Chem implementations in the Korea-United States Air Quality field study (KORUS-AQ) for air quality studies over the Seoul Metropolitan Area (Choi et al., 2020; Goldberg et al., 2019; Lennartson et al., 2018; Park et al., 2021; Saide et al., 2020). The model was driven by reanalysis meteorology, [NCEP Final Reanalysis \(NCEP FNL\)](#), ~~Final Operational Global Analysis data (FNL)~~, and Copernicus Modeling Service (CAMS) chemical boundary conditions (Commerce, 2000; Inness et al., 2019). [Meteorology was constrained using four-dimension data assimilation \(FDDA\) via grid nudging applied to model domains using the 0.25° NCEP FNL reanalysis fields to improve large-scale wind representation.](#) A two-domain approach with one-way nesting was incorporated to gauge strengths between coarse- and high- resolution simulations. D01 (20 km)

133 spans a large portion of the GEMS field of regard, covering primary transboundary pollution sources (e.g., deserts in
 134 China/India, anthropogenic emissions from China/India). A nested 4 km domain (D02) is centered over Bangkok (Fig. 1).

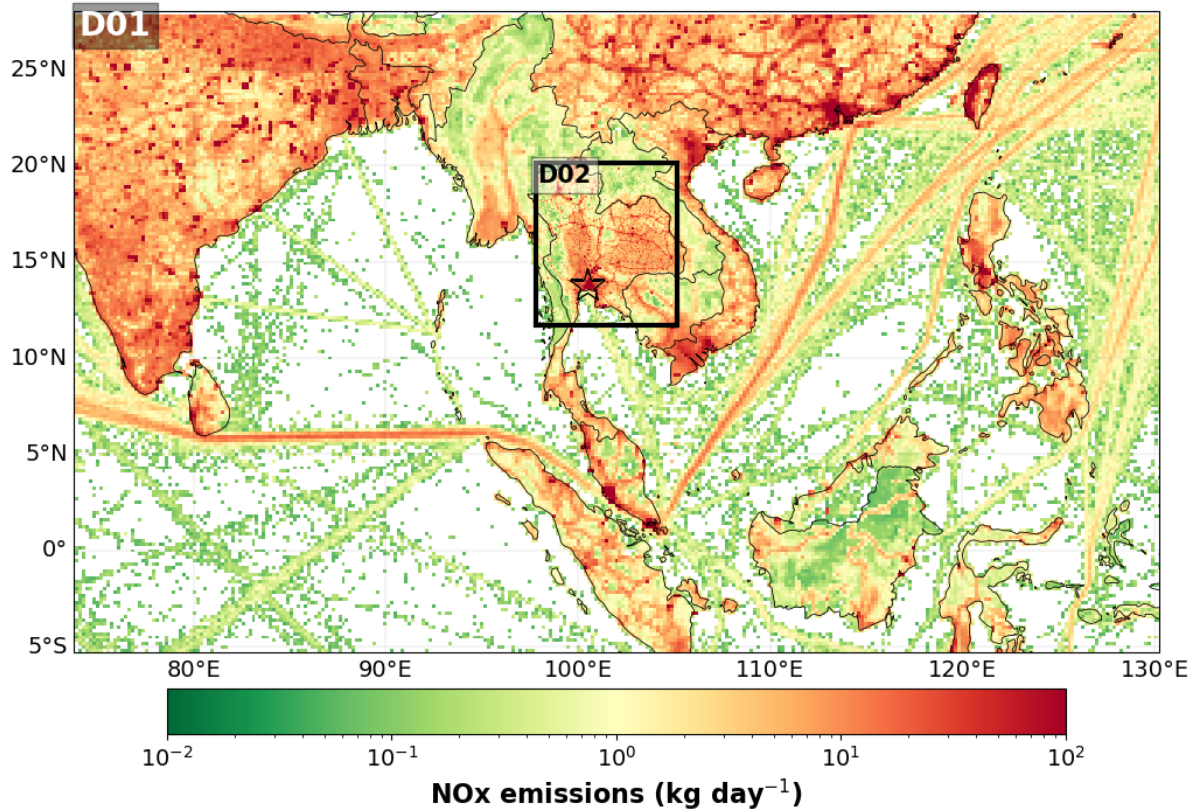
135
 136 Original anthropogenic emissions of trace gases and primary aerosols were based on the Emissions Database for Global
 137 Atmospheric Research (EDGAR v5) (Crippa et al., 2020) inventory at $0.1^\circ \times 0.1^\circ$ horizontal resolution. For D02, EDGAR
 138 emissions for the transport and industrial sectors were downscaled using the Open-source Data Inventory for Anthropogenic
 139 Carbon Dioxide emission inventory (ODIAC) at $1 \text{ km} \times 1 \text{ km}^2$ resolution (Oda et al., 2018). This is done by distributing EDGAR
 140 emissions into the 1 km^2 grid using ODIAC CO_2 as a spatial proxy in a mass conserving way. Biogenic, dust, sea salt, and fire
 141 emissions were computed within WRF-Chem using the model's full-chemistry emission modules (Table 1). In this
 142 configuration, dust and sea-salt emissions are calculated every chemistry timestep, while biogenic emissions (MEGAN) are
 143 updated every 30 minutes. For fire emissions, plume rise is enabled, in which the injection heights are diagnosed using the
 144 plume-rise parameterization and emissions are vertically distributed (typically $\sim 80\%$ at the surface with the remainder aloft).
 145 The model was configured using the RACM-MADE-VBS (Ahmadov et al., 2012; Tuccella et al., 2015) chemical mechanism
 146 and physics parameterizations selected based on prior campaign experience (e.g., KORUS-AQ), with updates to better
 147 represent secondary organic aerosol formation, heterogenous chemistry, and aerosol properties. The modal aerosol scheme in
 148 MADE-VBS tracks both particle mass and number, allowing mode diameters to evolve dynamically with aerosol aging and
 149 growth processes. Hereafter, we will refer to this model configuration as WRF_{Base} . Model cases with updated anthropogenic
 150 NO_x emissions will be referred to as $\text{WRF}_{\text{Updated}}$ and $\text{WRF}_{\text{Updated+BC}}$ (later introduced). ~~The model with updated anthropogenic~~
 151 NO_x emissions (later introduced) will be referred to as ~~$\text{WRF}_{\text{Updated}}$~~

152
 153 **Table 1** WRF-Chem base (WRF_{Base}) model configuration and input datasets.

Component	Configuration/Source
Model Version	WRF-Chem v4.2.2
Domain	D01: 20 km (regional); D02: 4 km (nested)
Meteorological IC/BC	NCEP FNL reanalysis ($0.254^\circ \times 0.254^\circ$; 6-hourly)
Chemical IC/BC	CAMS global model output
Chemistry Mechanism	RACM-MADE-VBS (with aqueous reactions)
Anthropogenic Emissions	EDGAR v5; downscaled with ODIAC CO_2
Biogenic Emissions	MEGAN v2.1 (Guenther et al., 2006)
Biomass Burning Emissions	QFED v2.6 (Grell et al., 2011; Koster et al., 2015)
Dust Emissions	GOCART scheme (Zhao et al., 2010)
Sea Salt Emissions	Gong et al. (1997) parameterization (Gong et al., 1997)

Radiation Scheme	RRTMG (longwave); Goddard (shortwave)
Cumulus Parameterization	Grell-Freitas (D01 only)
Microphysics	Morrison (double-moment) (Ye et al., 2021)
PBL Scheme	Mellor-Yamada-Janjic TKE scheme
Simulation Period	14 – 27 March 2024

155



156

157 **Figure 1.** Spatial illustration of the WRF-Chem model domain configuration, including D01 (20 km) and D02 (4 km), and
158 average base-model NO_{x2} input emissions from EDGAR v5. D02 is centered over Thailand, and the urban signal associated
159 with the Bangkok Metropolitan Region (BMR) is highlighted by the star.

160

161

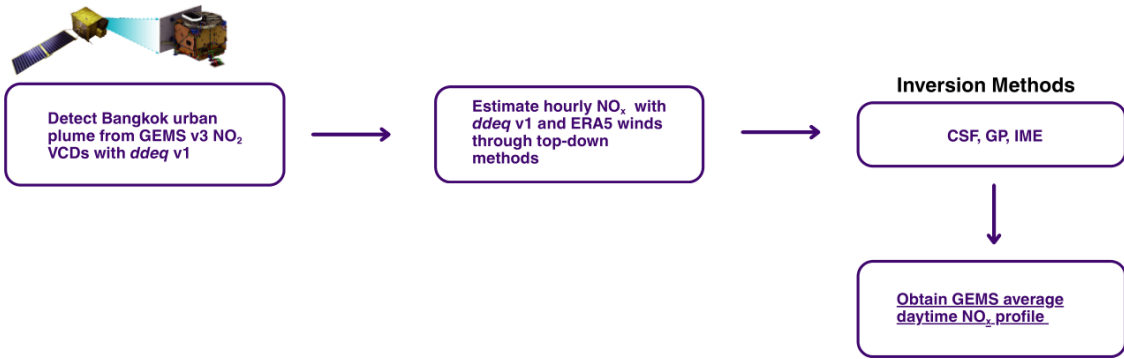
162

163

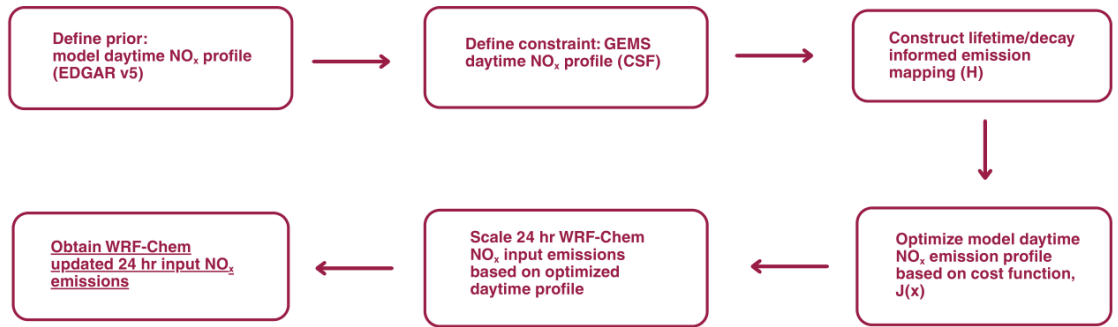
164

165
166
167
168
169
170
171
172
173
174
175
176
177
178
179
180
181
182
183
184
185
186
187
188
189
190
191
192
193
194
195
196
197
198

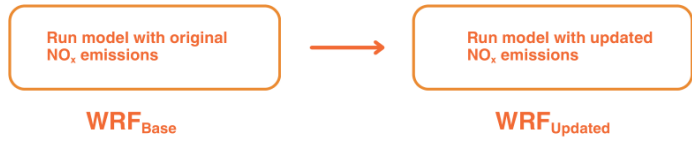
1 Estimate Daytime NO_x Emissions from GEMS



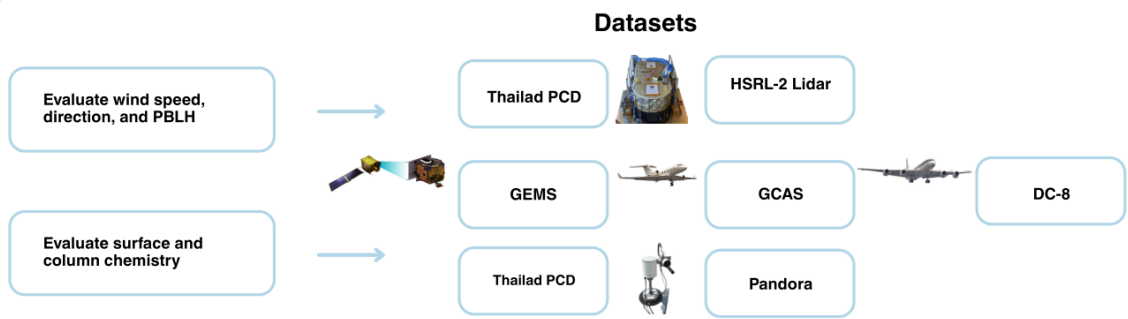
2 Correct WRF-Chem's NO_x Profile Based on GEMS



3 Test WRF-Chem NO_x Sensitivity



4 Evaluate WRF_{Base} and WRF_{Updated}



199
200
201
202
203
204
205

206 **Figure 2.** Schematic overview of the workflow used to derive satellite-constrained daytime NO_x emission profiles and assess
207 their impact in WRF-Chem over the BMR. (1) Urban NO₂ plumes are detected using GEMS tropospheric NO₂ columns, and
208 hourly NO_x emissions are estimated using top-down methods implemented in the *ddeg* v1 Python library. (2) a GEMS-derived
209 daytime NO_x profile is used to constrain the prior emission profile through an optimization framework, yielding updated input
210 24 h NO_x emissions for WRF-Chem. (3) Model simulations are performed using both the original and updated emissions. (4)
211 Model performance is evaluated against surface, column, airborne, and observations.

212 3 Satellite-derived ~~top-down~~ NO_x emission estimates

213 3.1 Correcting for GEMS bias prior to inversion

214 Recent independent validation studies of the operational GEMS v3 product over Bangkok and South Korea report low biases
215 in NO₂ columns relative to ground-based sun-photometer and DOAS measurements (Bae et al., 2025; Jung et al., 2025). Bae
216 et al. (2025) shows that GEMS v3 increasingly underestimates NO₂ relative to Pandora under high-NO₂ conditions ($>1 \times 10^{16}$
217 molecules cm⁻²) as is the case for Bangkok pollution levels. In Jung et al. (2025), validation results over Bangkok indicate a
218 pronounced low bias in GEMS tropospheric NO₂ columns relative to Pandora, with regression slopes of ~ 0.35 for v2.0 and
219 ~ 0.28 for v3.0, indicating increasing underestimation at higher NO₂ levels. While moderate correlations ($r \approx 0.6$ – 0.7) suggest
220 that GEMS captures temporal variability, column magnitudes are substantially underestimated, particularly under polluted
221 conditions. The persistence of this behavior in the v3.0 product indicates that the low bias is not fully corrected by recent
222 algorithm updates and is consistent with retrieval sensitivity limitations in highly polluted urban environments (Jung et al.,
223 2025).

224 To address the low bias in GEMS prior to the NO_x satellite emission inversion, we first quantify the GEMS bias relative to
225 Pandora measurements over our period of interest (14 – 27 March 2024). We compare total column GEMS NO₂ to Pandora
226 Level 2 direct-sun total column retrieval, filtering for high quality measurements (quality flag = 10) and averaging to hourly
227 means. GEMS columns are sampled at the nearest grid cell to each Pandora site and temporally collocated. Results are shown
228 in Fig. S1. GEMS NO₂ columns are generally about a factor of two lower than Pandora measurements (mean bias $\approx -9.2 \times$
229 10^{15} molecules cm⁻²). This factor-of-two difference persists throughout March 2024 (Fig. S1).

230 To assess the sensitivity of the top-down NO_x inversion framework to this bias, we apply a simple correction factor to GEMS
231 prior to inversion. Specifically, GEMS NO₂ columns over the BMR are scaled by a factor of 1.67 derived from the Pandora
232 comparison. The inversion is then performed with and without the bias-corrected columns.

234 3.2 GEMS inversion framework

235 Previous studies have used satellite data (OMI, TROPOMI, SCIAMACHY, GOME (-2), OMPS) to estimate top-down NO_x
236 emissions over urban areas, but were limited to once-a-day, mid-afternoon measurements, leaving temporal variability in
237 emissions largely unaddressed (Beirle et al., 2011; Goldberg et al., 2017, 2019). Ground-based and aircraft measurements of
238 emissions can be challenging to constrain given boundary layer dynamics, such as changes in boundary layer height, stability,
239 and vertical mixing, which can strongly influence observed concentrations of trace gases (Goldberg et al., 2017, 2019).
240 Additionally, temporal allocation in bottom-up emission inventories remain a significant uncertainty, particularly at hourly
241 and daily timescales because default temporal profiles (diurnal, weekly, seasonal) often fail to capture real activity patterns,
242 meteorological influences, and sector-specific variability (Goldberg et al., 2017, 2019; Mues et al., 2014). GEMS observations,
243 however, offer a unique opportunity to provide hourly emissions rates over Bangkok, complementing existing inventories that
244 are usually provided at monthly scales. To estimate NO_x emissions over Bangkok in March 2024, we apply the methodology
245 of Kuhlmann et al. (2024), implemented through the openly available data-driven emission quantification (*ddeq v1*) Python
246 library (see step 1 Fig. 2). The standard *ddeq* library implements computationally inexpensive methods (e.g., Gaussian Plume
247 Inversion (GP), Cross-Sectional Flux (CSF) method, Integrated Mass Enhancement (IME) method) to estimate emissions from
248 Sentinel5P-TROPOMI images (Graziosi and Manca, 2025; Meier et al., 2024). One study found limited temporal sampling
249 from polar-orbiting satellites (i.e., TROPOMI) can lead to systematic underestimation of NO_x emissions, particularly because
250 wintertime conditions with higher emissions are often poorly observed due to cloud cover (Meier et al., 2024). Geostationary
251 observations, including GEMS, address this limitation by providing hourly measurements that increase the likelihood of usable
252 data on partially cloudy days and enable direct resolution of daytime emission variability, which is not accessible from once-
253 daily LEO observations. For our application, we estimate emissions for daylight hours from GEMS tropospheric column NO₂
254 data over Bangkok during the ASIA-AQ campaign. A brief description of inversion methods and specifics is provided here. A
255 complete description of the inversion methods and algorithm can be found in Kuhlmann et al. (2024).

256
257 First, within the *ddeq* framework, the source location (Bangkok; 13.7563°N, 100.5018°E), GEMS v3 NO₂ column data, and
258 ERA5 wind fields are read. We chose to incorporate ERA5 wind fields as opposed to those provided by our high resolution
259 WRF-Chem simulation in this analysis given they presented significantly lower bias when compared to surface observations
260 (Fig. S2; Sect. 6.1). The ERA5 wind fields were downloaded and prepared by the *ddeq* library. Cloudy pixels (CF > 0.3) were
261 removed. Next, a plume detection algorithm is implemented to identify the Bangkok urban plume within the GEMS image.

262 The Bangkok plume subregion is estimated based on the source location and ERA5 wind field. Generally, a wind vector is
263 taken at the source location, and the plume is assumed to be located downwind, and a rectangular polygon can be drawn with
264 the along- and across- wind direction (Kuhlmann et al., 2024) . An example of these plume detections and associated
265 rectangular polygons is shown in Fig. S34. To aid the algorithm’s plume detection process, we identify two additional sources
266 north of Bangkok in the Saraburi province to avoid overlapping plumes from other NO_x sources. These correspond to the Khao
267 Wong (14.692856°N, 100.817204°E), and Thap Kwang (14.645313°N, 101.077650°E) regions, which we identified through
268 NO₂ patterns visible in the GEMS data in Fig. S34. These areas are not representative of Bangkok urban emissions as they are
269 a source of industrial activity related to limestone quarries and mining operations outside the inversion domain (Makkwao and
270 Prueksasit, 2021). Next, a center curve is fitted to the ~~data~~ data, and natural coordinates are calculated for the detected plume
271 associated to Bangkok to prep for the inversion algorithm. The coordinates are computed as the distance along and
272 perpendicular to the wind vector and for curved plumes this distance is computed as the arc length. Lastly, the data is prepared
273 for the satellite-derived emissions estimation by calculating and removing the background field and converting the NO₂
274 columns to kg m⁻². We estimate satellite-derived NO_x emissions using three inversion techniques included in *ddeg*: CSF, GP,
275 and IME methods. Below is a summary of the CSF method defined in Kuhlmann et al. (2024). GP and IME method descriptions
276 are available in the Supplement (e.g., S1) and Kuhlmann et al. (2024). In the following subsections and in Section 4, we refer
277 to the WRF-Chem input inventory based on EDGAR as the prior emissions, the CSF-based estimates from GEMS as the
278 satellite-derived emissions, the CSF-based estimates from the model-simulated columns as the model-derived emissions, and
279 the final emissions after applying the optimization framework, as the posterior emissions.

280

281 3.33.1 Cross-Sectional Flux (CSF) framework

282 The CSF approach applies mass conservation to quantify the NO_x flux transported downwind of Bangkok using (i) the wind
283 speed perpendicular to the plume and (ii) the NO₂ enhancement integrated along the plume (line density). The NO_x flux, F (kg
284 s⁻¹), is defined as:

$$285 \quad F = u \cdot q \quad (1)$$

286 where u (m s⁻¹) is the effective transport wind speed and q (kg m⁻¹) is the NO₂ line density. The emission rate, Q (kg s⁻¹), is
287 then inferred by correcting for chemical decay along the plume using:

$$288 \quad Q = \frac{F(x)}{D(x,\tau)} \quad (2)$$

289 Here, $D(x, \tau)$ represents the along-plume decay for lifetime τ . Here, τ represents an effective plume lifetime that accounts for
290 both chemical decay and plume dispersion (Kuhlmann et al., 2024).

291

3.34.1. Effective wind speed estimation

The *ddeg* algorithm computes an effective wind speed, i.e., the plume-transport wind, that supports an unbiased emission estimate. Ideally, this is a NO₂-enhancement-weighted average of the along-plume wind:

$$u(x, y) = \frac{\int_0^{z_T} \rho_e(x, y, z) u(x, y, z) dz}{\int_0^{z_T} \rho_e(x, y, z) dz} \quad (3)$$

Here, $\rho_e(x, y, z)$ is the NO₂ enhancement, $u(x, y, z)$ is the along-plume wind speed and z_T is the plume-top height. Because ρ_e is not directly observed, *ddeg* follows the approximation of Fioletov et al. (2015), in which the effective wind speed is estimated using the mean of the lowest three ERA5 layers, representing the typical transport level for near-surface urban plumes.

3.34.2. NO₂ line density calculation

The line density $q(x)$, is the integral of the NO₂ enhancement across the plume cross-section:

$$q(x) = \int_{y_1}^{y_2} (V(x, y) - V_{bg}(x, y)) dy \quad (4)$$

where $(V(x, y) - V_{bg}(x, y))$ represents the NO₂ enhancement above the background in kg m⁻². The integration bounds y_1 and y_2 are defined by the plume subregion (polygon) identified using the *ddeg* framework, which delineates the area of enhanced NO₂ associated with the source based on plume detection and wind direction (Kuhlmann et al., 2024). As such, the effective integration length across the plume is determined by the spatial extend of this polygon and the fitted Gaussian representation. To further compute this and account for missing satellite pixels, *ddeg* fits a Gaussian function to all GEMS pixels within a plume polygon:

$$g(y) = \frac{q}{2\sqrt{\pi}\sigma} \exp \exp \left(-\frac{(y - \mu)^2}{2\sigma^2} \right) + my + b \quad (5)$$

Here, μ and $\sigma(x)$ are the plume center and width in meters, and $my + b$ approximates a linear background. The plume width is further defined as:

$$\sigma(x) = \sqrt{\frac{2Kx^\kappa}{u}} \quad (6)$$

Where K is the eddy diffusivity coefficient (m² s⁻¹), κ accounts for nonlinear plume spreading under varying meteorology, and u is the effective transport wind speed defined above. The plume width, $\sigma(x)$ is derived from the Gaussian fit, and the parameters, K and κ are then determined by fitting, $\sigma(x)$ within the CSF framework. After fitting the Gaussian function, line densities are converted to fluxes using wind speeds at each corresponding downwind cross-section. Fluxes can be estimated for several cross-sections or polygons located downwind of the urban source (see Fig. S34, S42) (Kuhlmann et al., 2024). Using multiple points along the plume ensures different portions of the plume are sampled robustly.

3.3.4.3. Emission rate and lifetime estimation

Because NO₂ decays as the plume travels, the flux decreases with distance. To estimate the true emission rate, Q , at the source, *ddeq* fits a lifetime τ by matching modeled and observed flux decay:

$$F_a(x, \tau, \mu_a, \sigma_a) = Q \int_{-\infty}^{\infty} D(x', \tau) g(x - x', \mu_a, \sigma_a) dx' \quad (7)$$

Where μ_a and σ_a describe the city-scale plume location and extent, $D(x', \tau)$ describes the exponential decay along the plume, and g is the Gaussian parameter described above. Fitting Eq. (7) to the derived fluxes yields both the emission rate Q and plume lifetime τ (Kuhlmann et al., 2024).

3.3.4.4. Conversion from NO₂ to NO_x emissions

GEMS provides NO₂ column densities; therefore, a NO₂-to-NO_x conversion factor is needed to obtain NO_x emissions. Following the *ddeq* implementation, we use:

$$Q_{NO_x} = f_q \cdot Q_{NO_2} \quad (8)$$

to obtain NO_x estimates, where $f_q = 1.32$, as implemented in the *ddeq* algorithm: a localized factor was not derived from WRF-Chem due to known NO₂ biases in the prior simulation that would propagate into the conversion.

3.3.5 Structural uncertainties in the CSF framework

While the CSF framework provides a computationally efficient approach for deriving satellite-derived emissions, we acknowledge the method contains some structural uncertainties. First, the integration bounds used to compute the line densities (Eq. 4) are defined by the plume polygon identified from the satellite observations and wind field, such that the inferred top-down emissions depend on how the plume extent is delineated. As a result, inferred satellite-derived emissions can be sensitive to the selected plume extent, particularly under conditions of weak enhancements or overlapping sources. Second, the satellite-derived emission estimate scales directly with the effective wind speed (Eq. 1), such that errors in wind magnitude or direction propagate into the derived fluxes and satellite-derived emissions (see Fig. S5). Although ERA5 winds averaged over the lowest model layers are used to approximate plume transport, they may not fully represent local meteorological variability. Third, the inferred satellite-derived emission rate depends on the assumptions within the fitting framework, including the Gaussian representation of plume structure (Eq. 5), the parametrization of plume spreading (Eq. 6), and the effective lifetime τ (Eq. 7), which represent a simplified treatment of chemical decay and dispersion. Together, these factors represent inherent uncertainties in the CSF approach that should be considered when interpreting the satellite-derived emissions.

3.42 Results for satellite GEMS-derived NO_x emission estimates

GEMS NO_x emissions for Bangkok were estimated for daytime hours (00:45:00 – 06:45:00 UTC) during the ASIA-AQ deployment, 14 – 27 March 2024. The bias-corrected satellite inversion results are denoted with the subscript “BC”. Days with significant cloud contamination were removed from the analyses on a case-by-case basis, leaving satellite-derived emissions estimates for 14,15,17,18,22,24,25 March 2024. Satellite-derived eEmissions were computed for both weekends and weekdays, however, due to fewer weekends in the study period, weekday estimates are estimated to be more robust. We aggregate satellite-derived emissions hourly across weekdays to produce a summary daytime profile as illustrated in Fig. 3a and Fig. 3b. Satellite-derived eEmissions generally range between 0.5 – 4 kg s⁻¹ dependent on the inversion method. Bias-corrected results (Fig. 3b) illustrate a larger NO_x range, between 0.4 – 5 kg s⁻¹. Differences between CSF, GP, and IME satellite-derived emission estimates are expected, as each method relies on distinct assumptions regarding transport, plume geometry, and chemical loss. Similar spreads between methods have been reported in previous satellite-based emission studies (Hakkarainen et al., 2023, 2024; Santaren et al., 2025), particularly in urban environments, and can be interpreted as a measure of structural uncertainty rather than inconsistency between methodologies. Nevertheless, in this application, the CSF method illustrates a distinct daytime pattern with satellite-derived emissions peaking between 08:00:00 – 09:00:00 LT (bias-corrected) at 01:00:00 UTC (or 08:00:00 LT) coinciding with morning rush hour traffic, decreasing by approximately 65% by 14:00:00 LT. The GP and IME results illustrate a relatively stable daytime pattern and overall lower (< 50%) morning satellite-derived emission compared to the CSF method.

These results reflect both methodological differences and uncertainties in the underlying NO₂ observations. While the satellite-derived emissions might provide strong constraints on daytime variability, uncertainties in the GEMS NO₂ retrieval, particularly under high NO₂ conditions may influence the magnitude and timing of the inferred emissions as depicted in Fig. 3a,3b. The bias-corrected emissions are approximately 70% higher on average, indicating a substantial sensitivity of the inversion to the assumed retrieval bias.

3.53 Selection of the inversion method

To identify the optimal inversion method to be used for model correction, we test which method can successfully recover WRF-Chem’s prior daytime NO_x emission profile. To do so, we apply the *ddeq* inversion algorithms to WRF_{Base}, to produce “top-down” estimates from the model, which we will refer to as model-derived emissions. To replicate the satellite output, we re-gridded the model output from its native resolution to the satellite swath grid using the Universal Regridder for Geospatial Data (xESMF) Python package (Jiawei Zhuang et al., 2025). A nearest-neighbor interpolation scheme was used to preserve spatial gradients and align the model resolution to that of the satellite observations. This spatial re-gridding was performed on an hourly basis, corresponding to the nearest observation time (00:45:00 – 06:45:00 UTC). Following re-gridding, model NO₂

382 mixing ratios were vertically interpolated to the satellite pressure levels using a one-dimensional linear interpolation to ensure
383 consistency between the model and observed data for averaging kernel application. After interpolating model output to
384 GEMS's spatial and pressure grid, we computed the model's tropospheric column NO₂ (molecules cm⁻²). This is done by
385 converting the model's standard output of NO₂ volume mixing ratio (ppmV) to a number density with the ideal gas law:

$$386 \quad NO_{2\text{Number Density}} = \frac{P \cdot \chi_{NO_2} \cdot N_A}{R \cdot T} \quad (9)$$

387 Where χ_{NO_2} is the NO₂ mixing ratio in ppmV, P is pressure in Pa, T is temperature in K, R is the gas constant (8.314 J/mol/K),
388 and N_A is Avogadro's number ($6.022 \times 10^{23} \text{ mol}^{-1}$). The number density is then multiplied by the thickness of each vertical
389 model layer Δz to obtain the NO₂ amount per unit area. Summing across all layers yields the total column NO₂:

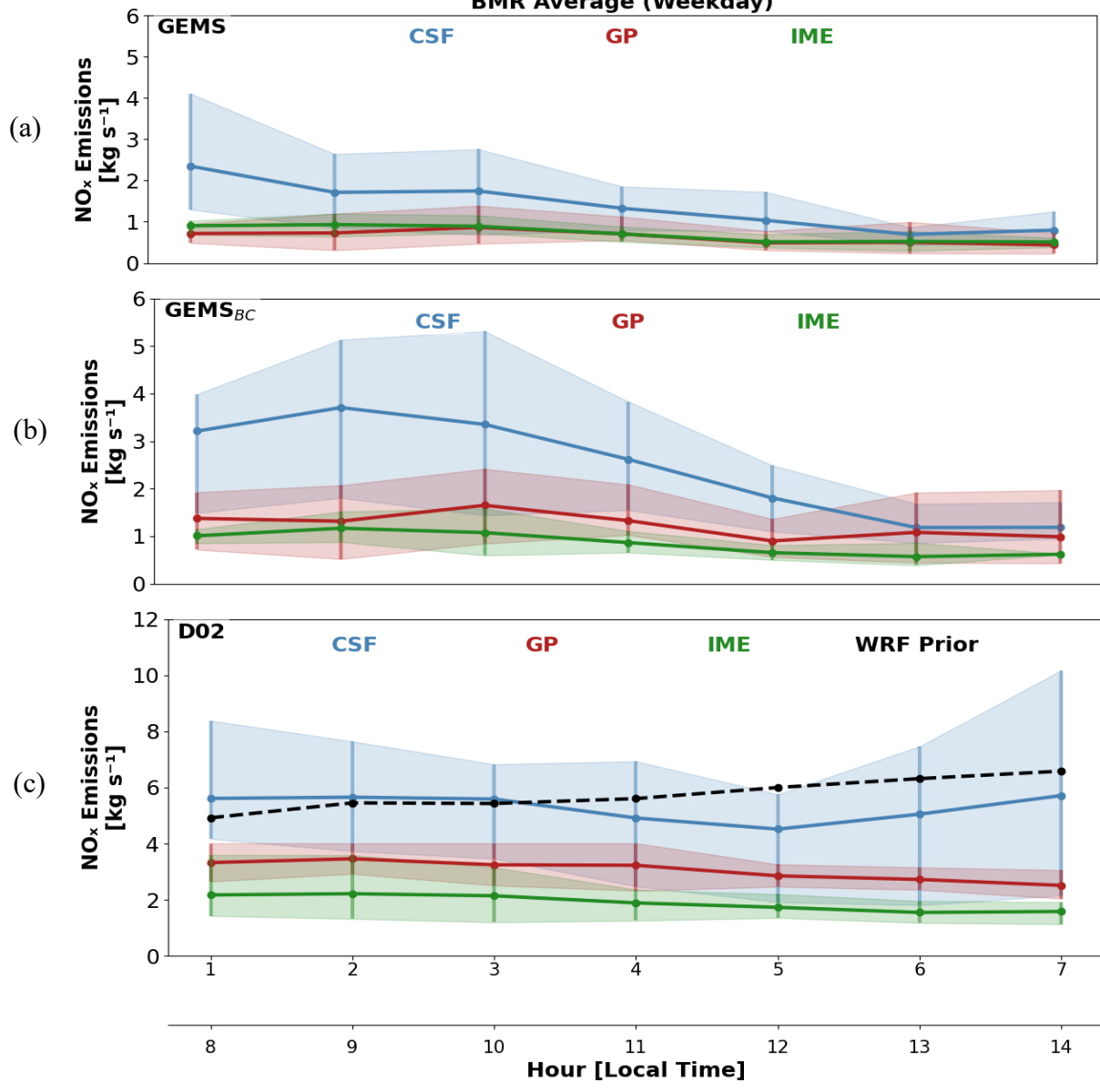
$$390 \quad NO_{2\text{WRF-GEMS}} = \frac{1}{10^4} \times \sum_k (A_k \cdot NO_{2\text{Number Density},k} \cdot \Delta z_k) \quad (10)$$

391 Where A_k is the averaging kernel value at layer k , Δz_k is the thickness of the model layer k , in meters, and $\frac{1}{10^4}$ converts the
392 units to molecules cm⁻². As WRF-Chem has no stratosphere, we regard this as the tropospheric column NO₂. The satellite
393 averaging kernel weights each model layer based on how sensitive GEMS is to that part of the atmosphere. This allows for a
394 direct comparison with GEMS retrievals.

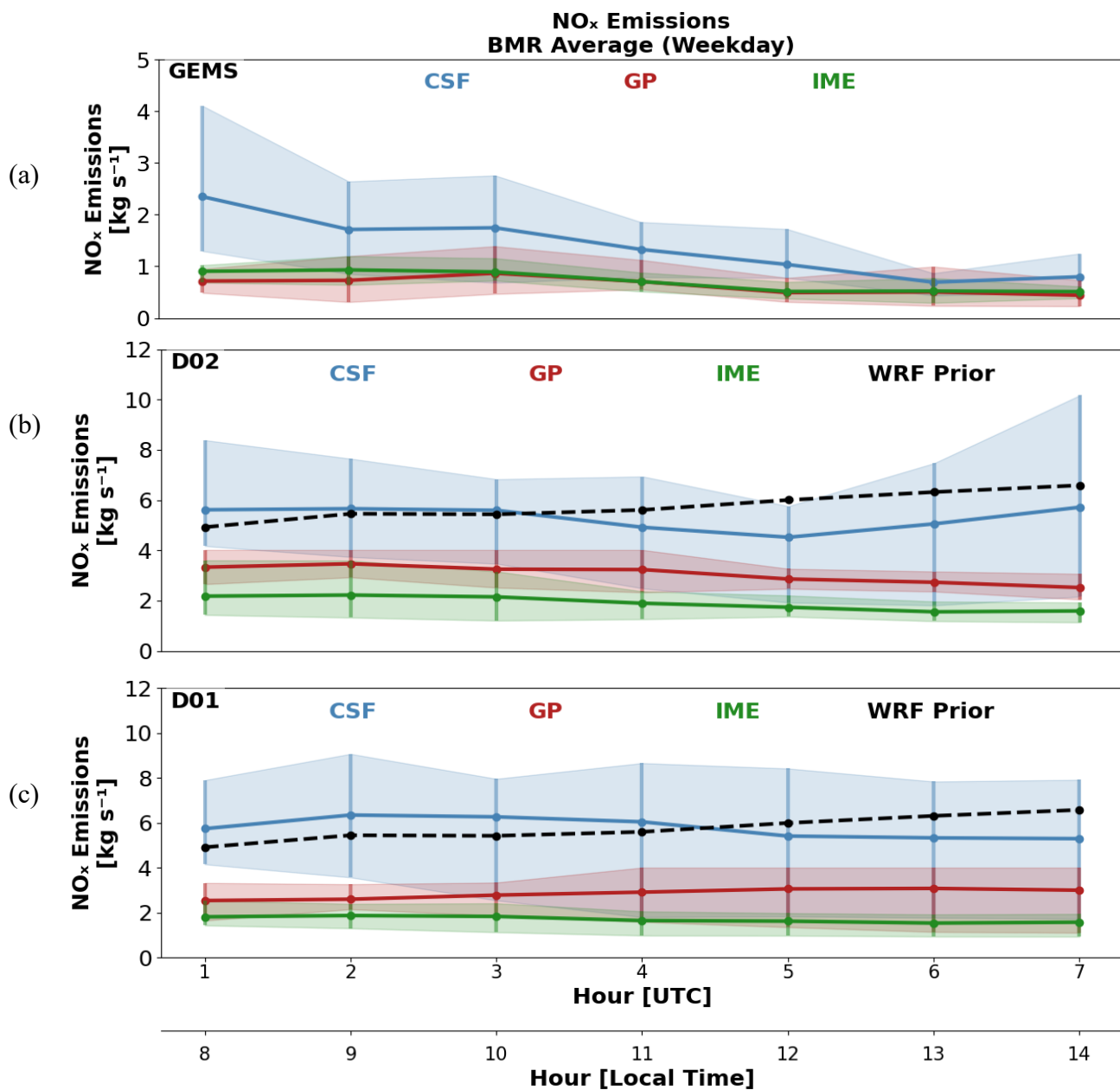
395

396 We compute model-derived NO_x emissions from re-gridded WRF_{Base} (which we denote as WRF-GEMS) with *ddeg* and the
397 resulting average daytime profile for Bangkok is illustrated in Fig. 3b, 3c. The model's shape and magnitude of model-derived
398 NO_x emissions differ substantially from the satellite-derivedGEMS emission data. Model-derived emissions are initially >
399 50% larger than GEMS-derived emissions. Additionally, there are minimal changes in the daytime pattern present in any of
400 the inversion methods. In fact, WRF-GEMS D02 sees an increase in emission between 08:00:00-10:00:00 LT, a pattern that
401 disagrees with the observed satellite-derived emissions. The results here further illustrate the need for an hourly correction to
402 the model's emission profile, rather than applying a single scaling factor across all hours. The WRF_{Base} prior emission profile
403 is shown by the black dashed line. For this comparison, we smoothed the prior emission profile using a 3 h backward-looking
404 average to account for the accumulation and chemical evolution represented implicitly in the inversion results. Overlaying the
405 prior emissions shows that the model-derived CSF method most accurately recovers them, likely due to its use of downwind
406 fluxes and multiple cross-sections across the plume, which provide additional constraints on plume evolution and reduce
407 sensitivity to local errors in wind fields, plume definition, and missing data compared to the IME and GP methods. As a result,
408 we select the CSF inversion method moving forward to correct and scale WRF-Chem's daytime NO_x emission profile.

**NO_x Emissions
BMR Average (Weekday)**



409
410



411
 412 **Figure 3.** Comparison of daytime NO_x emission estimates derived from (a) GEMS, (b) GEMS with bias correction applied
 413 (GEMS_{BC}) WRF-GEMS-D02, and (c) WRF-GEMS D02₁ using the Cross-Sectional Flux (blue), Gaussian Plume inversion
 414 (red), and Integrated Mass Enhancement (green) methods. Emissions (kg s⁻¹) represent averages across daytime hours and
 415 weekdays during the ASIA-AQ deployment period (14 – 27 March 2024). Model-derived-inversion emissions in (b) and (c)
 416 were obtained by re-gridding WRF_{Base} output to the GEMS spatial resolution and applying the same inversion methods. The

417 WRF_{Base} prior emission profile is shown as a black dashed line and represents a backward-looking three-hour average to
418 account for emission accumulation embedded in the inversion estimates.

419

420 **4 Model emission adjustment framework**

421 To better represent NO_x emissions over Bangkok, we developed an optimization framework to re-scale and shape WRF-
422 Chem's priorinput daytime emissions across the BMR (see step 2 Fig. 2). The prior emissions come from monthly EDGAR
423 v5 values. The optimization uses a cost function $J(x)$ to adjust daytime priormodel emissions based on GEMS NO_x retrievals,
424 incorporating the lifetime and uncertainties from both the model and observations.

425 **4.1 Optimization of daytime anthropogenic NO_x emissions**

426 **4.1.1. Observational constraint**

427 The GEMS average daytime NO_x profile (blue lines in Fig. 3a,3b) from the CSF method provides the observational constraint.
428 Two versions of the optimization are performed: one using the constraint derived from the bias-corrected retrievals, and one
429 without it. To improve consistency between the observed and modeled columns, we applied a correction factor to the constraint
430 to account for the portion of the NO₂ column that GEMS does not capture because of reduced sensitivity near the surface.
431 Although the air mass factor (AMF) calculation includes vertical weighting, the retrieved GEMS column can still
432 underestimate tropospheric NO₂ in conditions where a substantial fraction resides in the lowest few hundred meters and is
433 weakly sensed by the instrument. To address this sensitivity, satelliteGEMS-derived NO_x emission estimates were scaled using
434 the ratio of model-derivedWRF-Chem emissions obtained from the full column (i.e., Eq. (10) excluding the A_k) and from the
435 same column after application of the GEMS averaging kernel:

$$436 \quad y = e_{GEMS} \times \left(\frac{e_{WRF}^{TC}}{e_{WRF}^{AK}} \right) \quad (11)$$

437 Where e_{GEMS} , e_{WRF}^{TC} , and e_{WRF}^{AK} denote the satellite-derived CSF-derived daytime NO_x emission profiles derived from
438 GEMS, model-derived emissions from WRF-Chem (D02) total columns, and model-derived emissions from the same columns
439 after applying the GEMS averaging kernel, respectively. Hourly correction factors ranged between 1.05 – 1.33, where larger
440 corrections (e.g., 1.33) werewhere present in the morning hours, 01:00:00 – 02:00:00 UTC. This vertically adjusted satellite-
441 derived emission vector was used as the observational constraint, y , in the optimization.

442

443 **4.1.2. Prior assumptions, lifetimes, and temporal weighting**

444 The prior for the optimization, x_b , refers to the bottom-up daytime NO_x emission profile shown in the black dashed line in Fig.
445 3cb. For the optimization, it is necessary to map the priormodel emissions to the satellite-derived emissions through the

446 observational operator H . Satellite emissions of NO_x represent not only emissions from the current hour, but also contributions
 447 from preceding hours. To address this, we introduce an operator H that links the ~~prior model~~ daytime hourly emissions to the
 448 ~~satellite-derived observed GEMS~~ NO_x amounts. Each row of H defines how emissions from a set of prior model hours
 449 contribute to an observation at time, t_i .

450
 451 For each GEMS observation hour t_i , we assume that the column enhancement is influenced by emissions from a backward-
 452 looking window of three model hours:

$$t_i - 2, t_i - 1, t_i$$

453
 454 The window choice was determined by comparing inversion results to model priors using averaging windows from 1 – 6 hours.
 455 The three-hour window provided the best agreement with the ~~model-derived CSF emissions~~ ~~CSF inversion~~ as shown in Fig 3b,
 456 3c. Within this window, the contribution from each prior hour depends on the atmospheric lifetime of NO_2 for that hour. We
 457 use hourly lifetimes, τ , ~~derived from the GEMS-based which were fitted within the~~ CSF inversion in Eq. (7), ~~where τ is fitted~~
 458 ~~from observed along-plume decay using ERA5 winds, and is therefore independent of WRF-Chem meteorology. This ensures~~
 459 ~~the satellite-derived emission estimates are completely independent of the WRF-Chem simulations. For reference,~~ WRF-
 460 Chem-derived decay times are generally longer than those inferred from ~~GEMS, GEMS, reflecting differences in modeled vs.~~
 461 ~~observed loss and dilution processes with partial overlap at earlier hours but increasing divergence later in the day, indicating~~
 462 ~~differences in the effective loss and dilution processes represented by the model.~~ Hours with no satellite information, are
 463 assigned a default lifetime of 3 hours. We then apply a simple exponential decay law:

$$w(\Delta t) = \exp\left(-\frac{\Delta t}{\tau}\right) \quad (12)$$

464 where:

$$\Delta t \in \{0,1,2\}$$

465
 466 is the time lag between when NO_x was emitted and when its NO_2 enhancement is observed. These raw weights are normalized
 467 within each row of H to ensure mass conservation:

$$H_{i,j} = \frac{w(\Delta t_j)}{\sum_j w(\Delta t_j)} \quad (13)$$

468
 469 Thus, $H_{i,j}$, represents the fraction of the observed column at hour i , that is attributable to emissions from model hour j . This
 470 framework of H ensures that shorter lifetimes contribute to a stronger emphasis on the most recent emissions, appropriately
 471 reflecting rapid chemical loss, and longer lifetimes spread the influence of emissions over multiple hours, consistent with
 472 slower decay. By embedding this chemical persistence into the operator, H , we obtain a physically representative mapping
 473 between model emissions and the satellite observations that are used to constrain them.
 474
 475

4.1.3. Solution for posterioroptimized daytime emissions

A model corrected daytime NO_x emission profile (posterior), \hat{x} was obtained by minimizing the following cost function:

$$J(x) = \frac{1}{2}(y - Hx)^T R^{-1}(y - Hx) + \frac{1}{2}(x - x_b)^T B^{-1}(x - x_b) \quad (14)$$

Where y is the satellite-derivedGEMS, column-corrected NO_x emission vector, x is the unknown corrected model daytime emission profile, x_b is the model prior profile, $R = \sigma_r^2 I$, $B = \sigma_B^2 I$ are the observation and background error covariance matrices, and H is the observational operator matrix described above. In this study, we use $R = 1$ and $B = 10$. These values were based on sensitivity tests in which we vary R and B over several orders of magnitude. The chosen values represent a compromise that allowed the posterioroptimized emission profile to closely follow the satellite constrains while preventing excessive deviations from the prior emission profile. To account for temporal correlation in prior emission errors, the elements of B are defined as:

$$B_{i,j} = \sigma_B^2 \exp\left(-\frac{|t_i - t_j|}{L}\right) \quad (15)$$

Where $|t_i - t_j|$ is the temporal separation between emission hours i and j , and L is the temporal correlation length, set to $L = 2 \text{ hr}$ in this study. This setup ensures that prior errors vary smoothly in time rather than independently hour-to-hour. Finally, the cost function was minimized using a Sequential Least Squares Quadratic Programming (SLSQP) algorithm (minimize(method='SLSQP') — SciPy v1.16.2 Manual, 2025; Nocedal and Wright, 2006). The result is a corrected model hourly emission vector, \hat{x} , that balances the satellite-derived emissions observations with the model's prior estimate while accounting for chemistry and transport behavior (Fig. 4).

Figure 4a and 4c illustrates the raw hourly daytime NO_x for both the prior model (dashed purple) and the optimized version (solid purple), based on constraints applied without and with the GEMS bias correction, respectively. In both bases, tThe posterioroptimized profile departs notably from the prior in both magnitude and shape, shape. In the case without the bias-corrected constraint (Fig. 4a), with a pronounced a morning peak is visible at 07:00:00 LT, followed by a steady decline until 13:00:00 LT. This pattern is consistent with temporal patterns in weekday traffic intensity in Bangkok found in Ly et al. (2015), which found the morning traffic to peak at 07:30:00 LT ending at 09:30:00 LT, and the evening peak from 17:00:00 to 20:00:00 LT (outside of GEMS observing window). Activity begins to increase at 13:00:00 LT which corresponds to the NO_x increase we begin to see in the posterioroptimized result after 06:00:00 UTC. The case with the bias-corrected constraint (Fig. 4c) places peak morning emission closer to the model prior at 07:00:00 – 08:00:00 LT, with NO_x declining slightly later, at 09:00:00 LT. NO_x emission begins to increase after 13:00:00 LT similar to what is depicted in Fig. 4a. When the prior and posterioroptimized hourly emissions are passed through H , we obtain a temporally smoothed emission profile consistent with what GEMS would observe (Fig. 4b,4d). Figures 4b and 4d shows the posterioroptimized profile closely reproduces the GEMS-derived daytime pattern, indicating the optimization effectively aligns model emissions with satellite-derived emissions observations while preserving components of the prior model behavior.

508 4.2 Adjustment of WRF-Chem diurnal emission profiles

509 Using satelliteGEMS-derived NO_x emissions and the posterioroptimization results above, we correct the WRF-Chem 24 h
510 input emissions over the BMR. Since GEMS provides estimates over 01:00:00-07:00:00 UTC, we only have
511 posterioroptimized model emissions over this window. To apply these updates to the full gridded 24 h WRF-Chem
512 anthropogenic emission input (00:00:00-23:00:00 UTC), while preserving the model's spatial distribution, we compute hourly
513 scaling factors which we use to adjust the gridded priorinput NO_x emissions. Because GEMS provides constraints only during
514 the daytime overpass window, the derived scaling below primarily reflects daytime emission adjustments. We therefore apply
515 the mean scaling factor uniformly during the nighttime hours to preserve the prior temporal structure and avoid introducing
516 artificial discontinuities between the constrained and unconstrained hours, particularly given the large daytime emission
517 reductions. This approach is consistent with previous satellite-constrained emission studies (e.g., Goldberg et al., 2019) which
518 constrain emission magnitude based on a single daytime value derived from OMI. Where available, locally derived temporal
519 profiles should be used to better represent regional emission patterns; in this study, our prior profile reflects the best available
520 regional representation for Asia at the time of study.

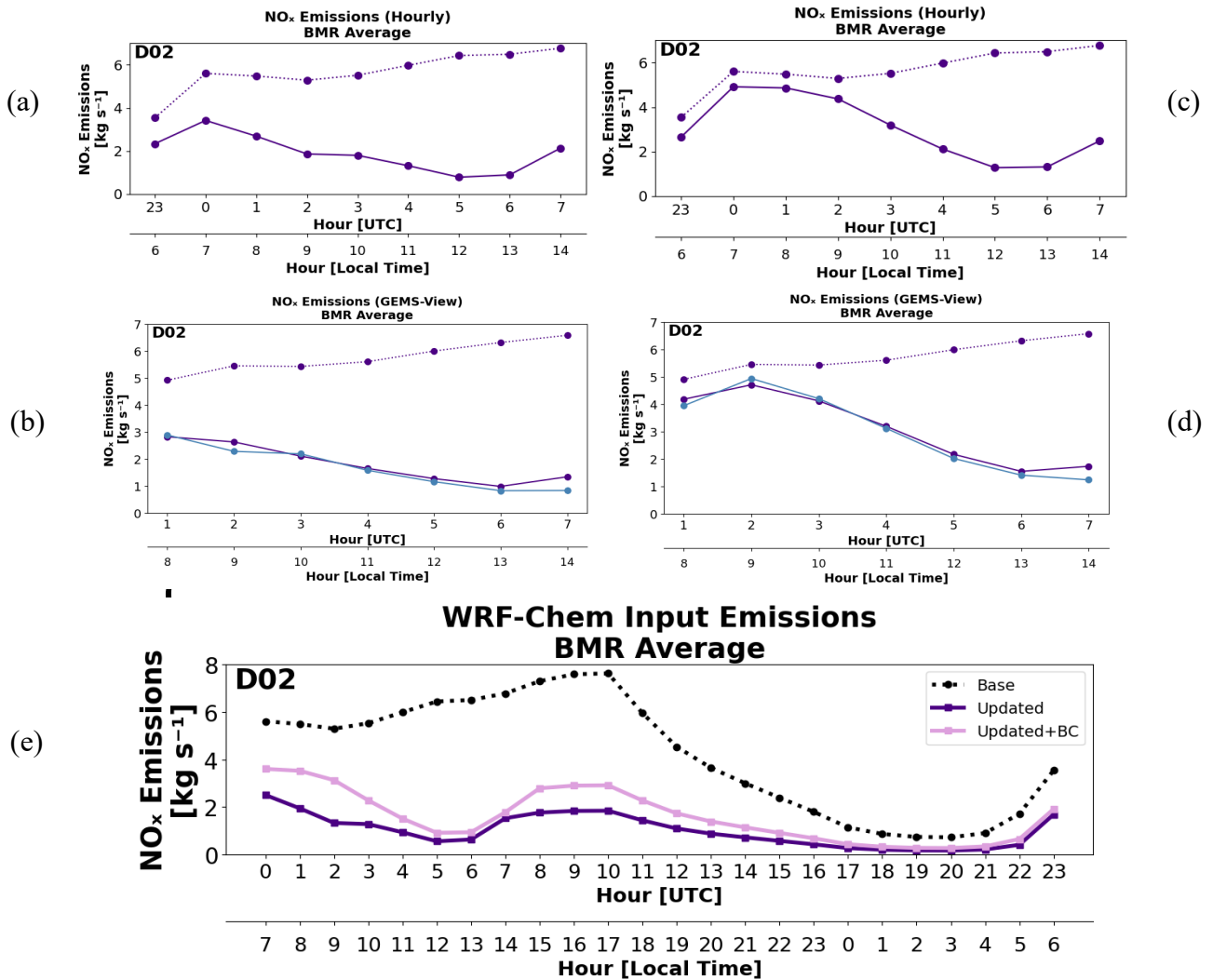
521
522 To compute the factors, hourly WRF-Chem NO and NO₂ prior emission fields were summed across the vertical levels and
523 masked to the Bangkok region bounded by N-S:13.5°-15.0°, W-E:100.2°-100.9°, using the WRF-Chem grid. In WRF-Chem,
524 NO_x emissions are stored as NO₂-equivalent mass ('NO_x-as-NO₂'), so all conversions use the molecular weight of NO₂. The
525 total emissions were converted to mol hr⁻¹ using a molecular weight of 46.01 g mol⁻¹ and an area of 16 km² per grid cell
526 (following the resolution of D02). Each posterioroptimized emission, \hat{x}_h was converted from kg s⁻¹ to mol hr⁻¹ and divided by
527 the corresponding original WRF-Chem total to compute a scale factor, f for each hour h :

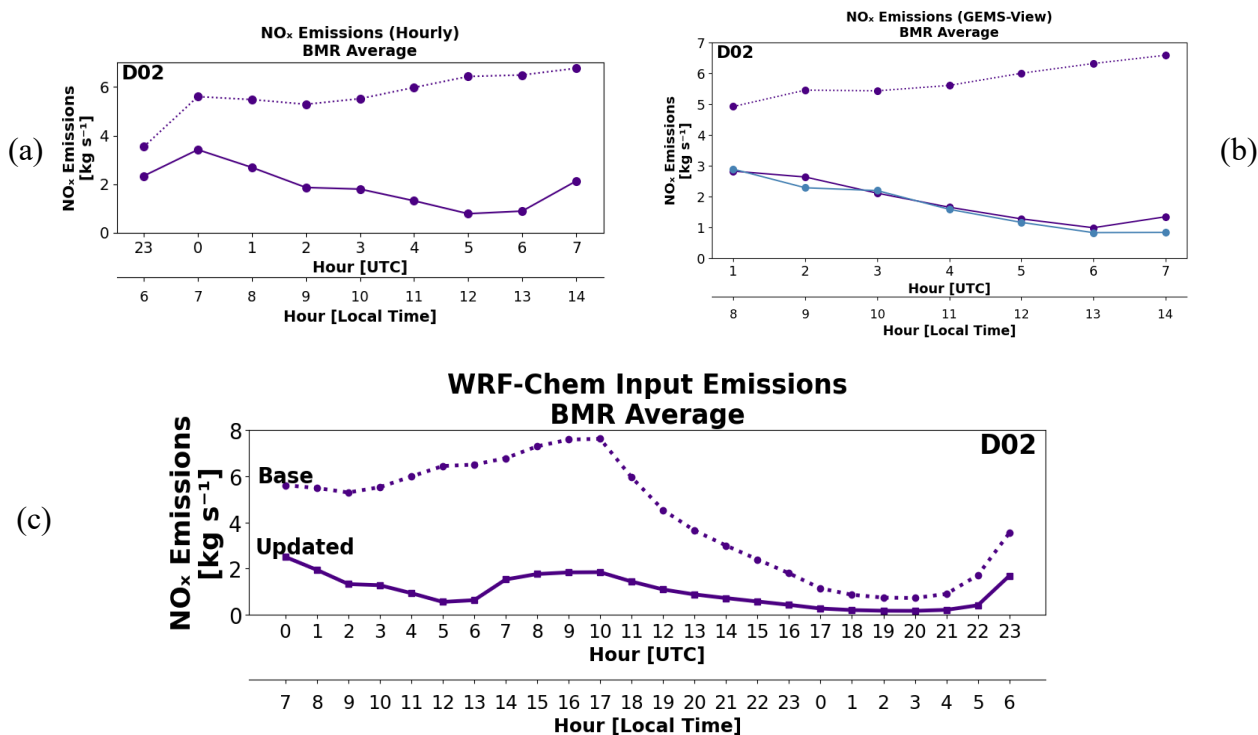
$$528 \quad f = \frac{\hat{x}_h \times \frac{1000}{46.01} \times 3600}{E_H^{WRF}} \quad (16)$$

529 Where E_H^{WRF} is the original domain-integrated prior NO_x emissions for hour h . Since the optimization covered hours with
530 GEMS measurements, the scaling factors for the remaining model hours were computed using the ratio of average daytime
531 posterior emissions where averages are taken over the constrained hours. Finally, we apply the scaling factors spatially over
532 the BMR. The scaling factor was applied to the hourly WRF-Chem anthropogenic emissions priorinput files and only to NO
533 and NO₂ grid cells within the BMR mask. This preserves the original spatial distribution but adjusts the total prior emissions
534 to match the posterioroptimized values. The updated emission files were then used to initialize an updated model simulation,
535 ran for the ASIA-AQ deployment period, which we will refer to as WRF_{Updated} (see step 3 Fig. 2).

536
537 Figure 4ee compares the average diurnal prior profile over BMR with the updated profile derived from the optimization and
538 scaling procedure. The optimized diurnal profile based on the bias-corrected GEMS constraint is illustrated by the light pink
539 line. The updated profiles shows a notable increase in NO_x between 07:00:00-10:00:00 UTC (14:00:00 to 17:00:00 LT), which
540 may reflect the beginning of a rush-hour signal over the city. Nighttime emissions retain the overall shape of the prior profile

541 but are scaled downward based on the daytime average. Figure [S6S4](#) maps the spatial distribution of these updates across
 542 BMR, showing the largest differences in the late afternoon and early evening, with localized reductions of up to $400 \text{ mol km}^{-2} \text{ hr}^{-1}$
 543 in the updated input emissions.





549
 550 **Figure 4.** Results of the emissions optimization, shown as averages over the BMR. (a) Posterior optimized (solid) and prior
 551 (dashed) daytime NO_x emissions in model space, where the prior represents the three-hour backward average of EDGAR v5
 552 emissions used as input to the optimization. (b) Same emissions as in (a) but transformed into observational space using the
 553 observational operator. The GEMS profile is shown in blue. (c) and (d) are representative of optimization results using the
 554 GEMS bias-corrected CSF results as the constraint. (e) Full diurnal cycle of updated (solid purple), updated+BC (solid pink),
 555 and prior (dashed) NO_x emissions. Note that, unlike (a), the prior in (e) does not include the 23 UTC hour from the previous
 556 day in the backward averaging. Results of the emissions optimization, shown as averages over the BMR. (a) Comparison of
 557 optimized (solid) and prior (dashed) daytime NO_x emissions. (b) Same as (a) but viewed through the GEMS observational
 558 operator. The GEMS profile is shown in blue. (c) Comparison of full optimized (solid) and prior (dashed) diurnal NO_x emission
 559 profiles.

561 **4.3 Comparison with bottom-up emission inventories**

562 To place the updated NO_x emissions in context of existing emission inventories, we compared total monthly emissions over
 563 the BMR against several widely used bottom-up inventories, our top-down emissions (including bias-corrected results – This
 564 Study_{BC}), and emissions from a chemical reanalysis product (Fig. 5). These include HTAP v3.2 (base 2019), a local Thailand
 565 Inventory (THAI-KMUTT) (base 2019), MIX v2.3 (base 2017), EDGAR v5 (base 2015), CEDS (base 2024), our study (2024),

566 and the Tropospheric Chemistry Reanalysis (TCR-3) top-down emissions TCR-3 (2024) (Miyazaki et al., 2020). Across
567 inventories, monthly totals for March can vary nearly by an order of magnitude, highlighting large uncertainty in regional NO_x
568 sources and emissions processing methodology. For example, although both HTAP v3.2 and MIX v2.3 rely on the REAS
569 framework (Kurokawa and Ohara, 2020) for Asian anthropogenic emissions, they are derived from different REAS versions,
570 temporal coverage, and processing assumptions, which can lead to substantial differences in absolute emission magnitudes
571 over Bangkok. HTAP v3.2 is based on REAS v3.2.1, which provides monthly emissions for 2000–2015 at a spatial resolution
572 of 0.25°. In the HTAP product, these emissions are re-gridded to 0.1° by assuming a uniform spatial distribution within each
573 grid cell (Guizzardi et al., 2025). In contrast, the MIX inventory is based on REAS v2, which covers 2000–2008 and reflects
574 earlier emission estimates and activity data (Li et al., 2024). REAS v2 was subsequently extended to 2010 following the scaling
575 approach described by Kurokawa & Ohara (2020).

576
577 Overall, HTAP v3.2 depicts the highest NO_x totals at 31kTons month⁻¹. THAI-KMUTT follows with emissions at ~20 kTons
578 month⁻¹, reflecting its incorporation of detailed regional activity from local emissions data. The coarser-resolution MIX v2.3,
579 and EDGAR v5, and CEDS inventories reflect lower totals, at ~13,11,10 kTons month⁻¹ respectively, consistent with the use
580 of different emission estimation methodology and older base years for MIX and EDGAR which correspond to lower macro-
581 economic (e.g., GDP) indicators in Thailand compared to 2019. Lastly, GEMS top-down NO_x estimates (including bias-
582 corrected results) and TCR-3 estimates based on the chemical reanalysis using TROPOMI NO₂ indicate substantially lower
583 emissions (2-43 kTons month⁻¹). These reduced magnitudes may result from both recent emission declines and structural
584 differences in how emissions are computed (i.e., top-down perspective).

585
586 It is important to note uncertainties are present and differ amongst emission methods. For example, bottom-up inventories
587 depend on activity data, emission factors, spatial approximations, and assumptions that may not capture rapid socio-economic
588 changes or region-specific behavior. Top-down estimates incorporate uncertainties from their respective satellite retrievals,
589 reanalysis data (e.g., ERA5), averaging kernels, chemical lifetime assumptions, and forecast-model transport and chemistry
590 (e.g., TCR-3). Together, these differences highlight the value of combining observational constraints with updated bottom-up
591 information to define NO_x emission estimates.

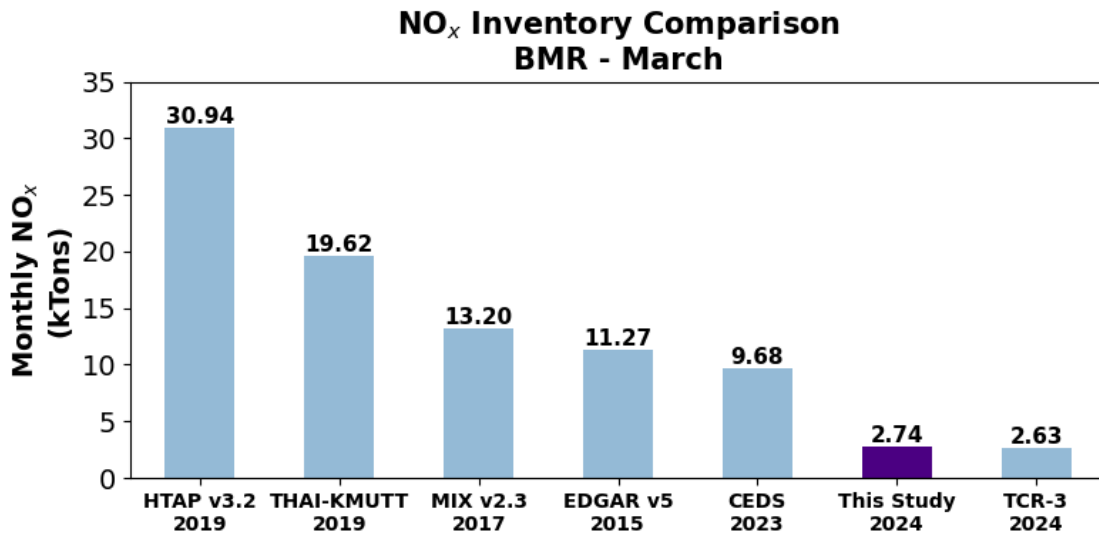
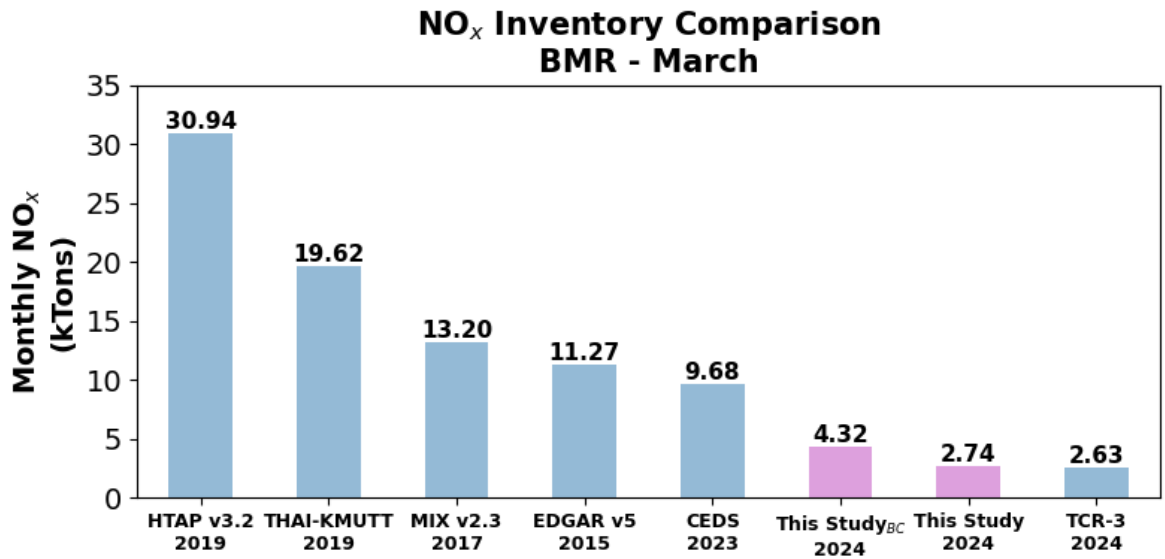


Figure 5. Comparison of March NO_x emissions over the BMR derived from bottom-up, top-down, and assimilated approaches. Bottom-up inventories (HTAP v3.2 (Guizzardi et al., 2025), THAI-KMUTT, MIX v2.3 (Li et al., 2024), EDGAR v5 (Crippa et al., 2020), and CEDS (Hoesly et al., 2018)) exhibit substantial variability. In contrast, top-down estimates from GEMS and TROPOMI (TCR-3) for 2024 indicate considerably lower emissions (2.6–~~4.32~~–7 kt month⁻¹), highlighting uncertainties in bottom-up inventory methodologies, satellite sensitivity, and potential changes in anthropogenic NO_x activity.

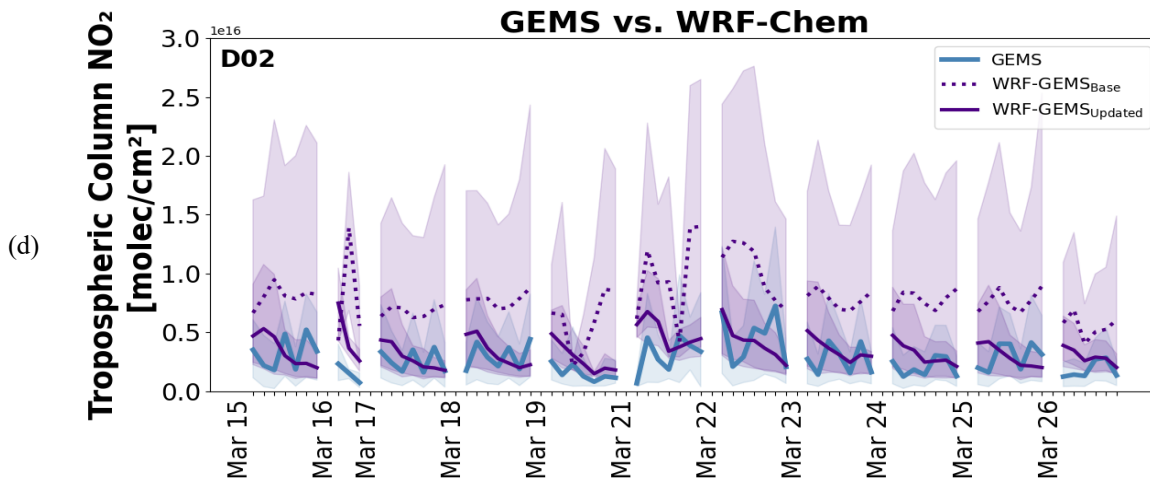
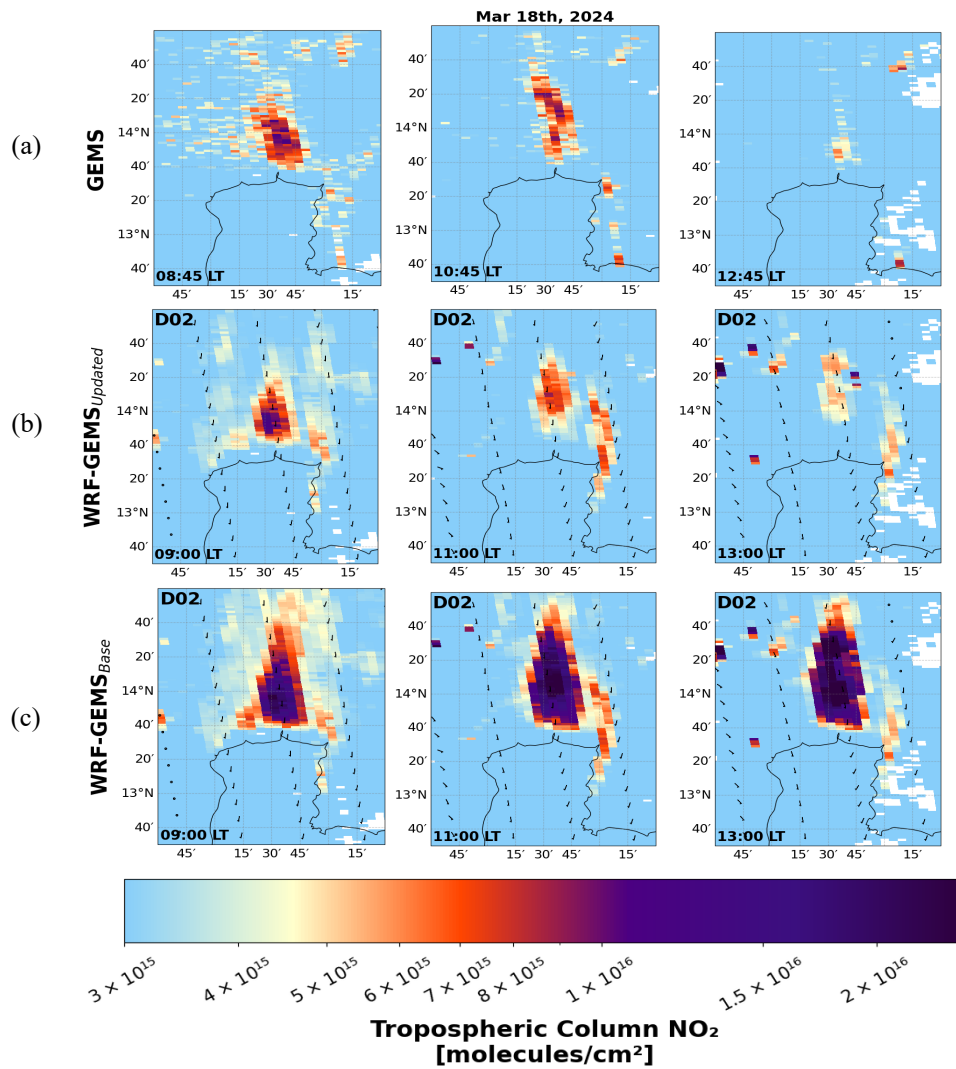
601 5 Evaluation against satellite observations

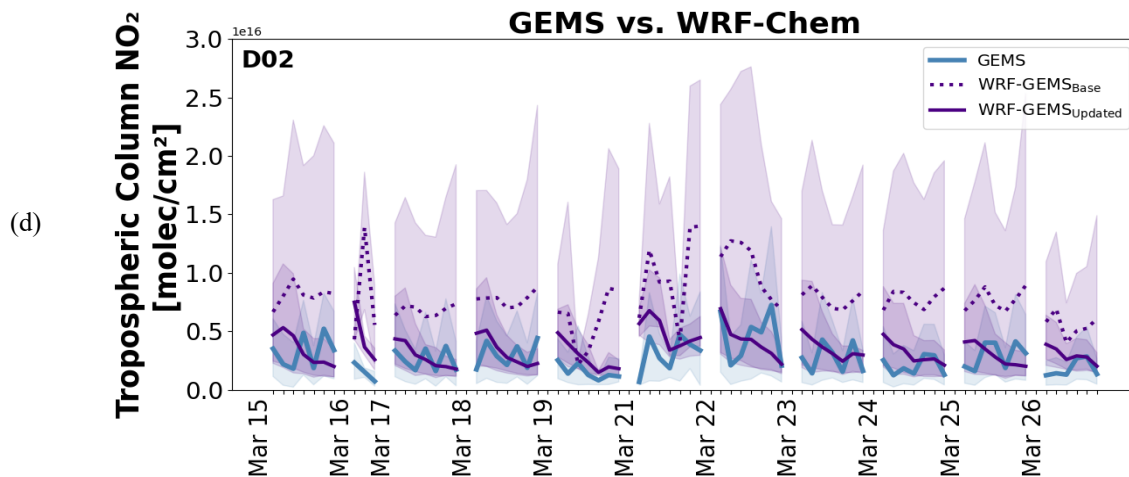
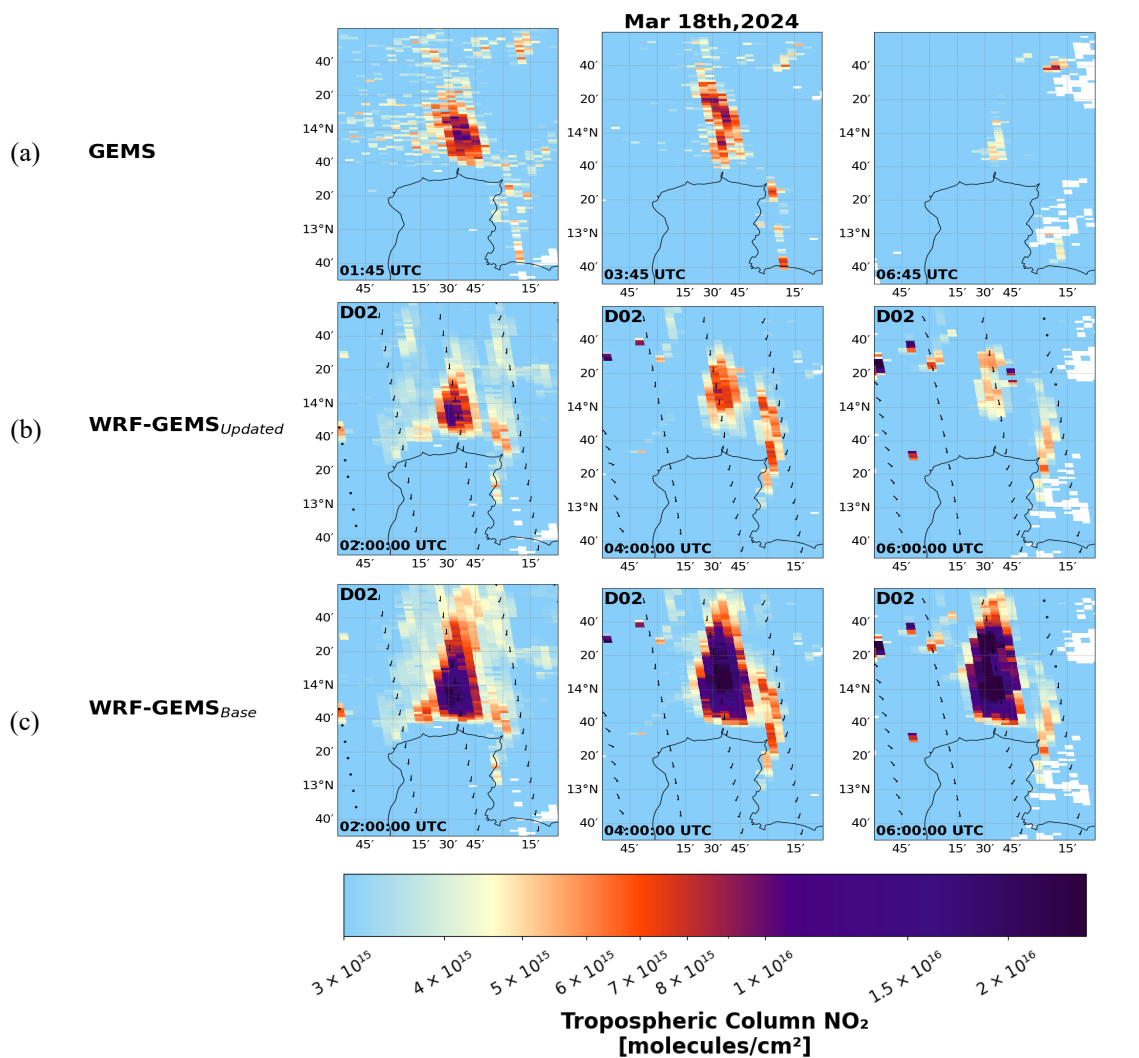
602 To evaluate the performance of WRF-Chem (Base + Updated) NO₂ simulations during the ASIA-AQ period (14 – 27 March
603 2024) in Bangkok, we first compared model output with satellite tropospheric column NO₂ retrievals from GEMS v3 data.
604 For GEMS observations, pixels were filtered based on cloud fraction (CF < 0.3). The GEMS averaging kernel and air mass
605 factor data were used to isolate tropospheric contributions and account for satellite instrument sensitivity. To enable a direct
606 comparison with our model output, we re-gridded model output from its native resolution to the satellite swath grid as explained
607 in Sect. 3.3. As before, refer to the re-gridded model simulations with the GEMS averaging kernel applied as WRF-GEMS.
608 To evaluate regional NO₂ variability, we aggregated satellite and model-derived tropospheric column NO₂ values over the
609 BMR, by defining a N-S (13.5-14°N), W-E (100.3-100.9°E) bounding box for the area. For pixels within this boxed region,
610 we calculate the mean NO₂ concentration, minimum NO₂, maximum NO₂, standard deviation, and the 10th and 90th percentiles
611 to characterize regional variability. This analysis was repeated on an hourly basis for each co-located WRF-Chem and GEMS
612 dataset, providing a regionally aggregated view of column NO₂ for intercomparison.

613
614 The results shown here are based on satellite comparisons using the non-bias corrected model results and are intended to
615 illustrate that the optimization brings the model closer to GEMS observations. The maps shown in Fig. 6 illustrate a spatial
616 comparison of (a) GEMS, (b) updated model results, WRF-GEMS_{Updated} D02, and (c) base model, WRF-GEMS_{Base} D02
617 tropospheric columns NO₂ over the BMR for several snapshots on 18 March 2024. Results for D01 can be found in Fig. S65,
618 S76. GEMS generally places BMR city enhancements between $5 \times 10^{15} - 2 \times 10^{16}$ molecules cm⁻² in a N-S direction. Both
619 WRF_{Updated} D01, D02 generally reflect the spatial distribution and magnitude of tropospheric column NO₂ observed during
620 daylight hours. WRF_{Updated} D02 (Fig. 6b) tends to place the city plume more northward at 04:00:00 and 07:00:00 UTC
621 compared to what is observed in GEMS data (Fig 6a). This spatial discrepancy is likely related to overpredicted model winds
622 (further discussed in Sect. 6.1) which displaces the plume in a northward direction. Additionally, while the inversion
623 framework adjusts emission magnitudes temporally, it does not correct spatial errors in plume transport or source distribution
624 (See Sect. 7.2 for further discussion). Nevertheless, the daytime pattern seen in GEMS is accurately reflected in WRF_{Updated}
625 with column NO₂ values at their peak in the morning hours (08:00:00 LT), decreasing substantially throughout the afternoon
626 (14:00:00 LT) due to photochemical interactions. This is a substantial improvement from WRF_{Base}, which sees a large
627 overestimation of NO₂ in the morning hours followed by persistent and growing NO₂ columns throughout the afternoon as
628 seen in Fig. 6c.

629
630 The time series in Fig. 6d illustrates a full comparison of daytime tropospheric column NO₂ values across model types in D02
631 (see Fig. S78 for D01) for the duration of ASIA-AQ. WRF-GEMS_{Updated} indicates a clear reduction in error and bias from
632 WRF_{Base} as illustrated by the reduced NO₂ columns and model spread. WRF_{Updated} also indicates corrected daytime patterns

633 compared to WRF_{Base}, indicating better consistency with GEMS observations for the deployment period with few exceptions
634 such as 22 March where GEMS has peaks in the afternoon (further discussed in Sect. 6.1).





638 **Figure 6.** Spatial comparison over the BMR on 18 March 2024 of tropospheric NO₂ columns from (a) GEMS, (b) WRF-
639 GEMSupdated D02, and (c) WRF-GEMSB_{Base} D02 for snapshots at 02:00:00, 04:00:00, and 07:00:00 UTC, corresponding to
640 approximately 09:00, 11:00:00, and 14:00:00 LT. (d) Tropospheric NO₂ column for daytime hours between GEMS (blue),
641 WRF-GEMSB_{Base} D02 (dotted purple), and WRF-GEMSupdated D02 (solid purple) during the ASIA-AQ deployment period.
642 Shaded regions indicate variability, represented by the 10th and 90th percentiles.

643 **6 Evaluation using independent observations**

644 To independently assess the performance of the optimized WRF-Chem simulations, we compared three model configurations:
645 WRF_{Base}, WRF_{Updated}, and WRF_{Updated+BC} results for D01 and D02 against a suite of independent airborne and ground-based
646 observations distinct from the satellite measurements used in the emission optimization process (see step 4 Fig. 2).
647 Comparisons between WRF_{Updated} and WRF_{Updated+BC} reflect the sensitivity of the model results to biases in the GEMS retrieval
648 used to constrain emissions in the optimization process. This evaluation primarily emphasizes the results of D02 (4 km), which
649 more directly represents urban-scale processes and exhibits improved performance compared to D01 across multiple
650 observational datasets. These datasets provide an unbiased test of how well the model reproduces meteorological conditions
651 and trace gas amounts beyond those directly constrained from GEMS observations. By evaluating WRF-Chem against surface
652 monitoring networks (Thailand PCD), Pandora spectrometer measurements, and airborne ASIA-AQ data (e.g., GCAS NO₂
653 columns, DC-8 vertical profiles), we examine the model's ability to capture daytime variability, vertical structure, and surface
654 concentrations of NO₂ across different spatial and temporal scales. Evaluation amongst these diverse datasets, therefore, helps
655 to support the robustness of the emission correction framework described in this paper.

656
657 **Table 2.** Summary of WRF-Chem D02 validation statistics for WRF_{Base} (B) ~~and~~ WRF_{Updated} (U), and WRF_{Updated+BC} (U+BC)
658 simulations evaluated against independent observational datasets. Metrics include mean bias (MB), mean error (ME),
659 normalized mean bias (NMB), normalized mean error (NME), root-mean-square error (RMSE), and Pearson correlation
660 coefficient (CORR).

661
662
663
664
665
666
667
668
669

Dataset	Species	Model Run	MB	ME	NMB	NME	RMSE	CORR
GCAS	Tropospheric NO ₂ column (molecules cm ⁻²)	B	4.0E+15	5.1E+15	93	1.2E+2	9.3E+15	0.64
		U	-2.4E+14	1.9E+15	-5.6	45	3.4E+15	0.54
		<u>U+BC</u>	<u>6.8E+14</u>	<u>2.3E+15</u>	<u>16</u>	<u>53</u>	<u>4.1E+15</u>	<u>0.4</u>
DC-8	NO _x O ₃ NO ₂ (ppbV)	B	1.3	1.4	82	87	2.8	0.97
		U	-0.81	0.8	-49	49	1.4	0.93
		<u>U+BC</u>	<u>-0.38</u>	<u>0.49</u>	<u>-23</u>	<u>30.3</u>	<u>0.89</u>	<u>0.94</u>
	CANOE NO ₂ (ppbV)	B	1.4	1.5	87	94	2.9	0.97
		U	-0.76	0.76	-48	48	1.3	0.93
		<u>U+BC</u>	<u>-0.34</u>	<u>0.50</u>	<u>-21</u>	<u>31</u>	<u>0.88</u>	<u>0.94</u>
Ground Monitors	NO ₂ (ppbV)	B	12	12	1.3E+2	1.3E+2	15	0.61
		U	-3.0	4.5	-32	47	5.6	0.53
		<u>U+BC</u>	<u>0.1</u>	<u>4.0</u>	<u>0.6</u>	<u>43</u>	<u>5.5</u>	<u>0.55</u>
	NO _x (ppbV)	B	14	15	1.4E+2	1.4E+2	18	0.59
		U	-3.6	4.9	-34	47	6.7	0.61
		<u>U+BC</u>	<u>0.02</u>	<u>4.8</u>	<u>0.2</u>	<u>46</u>	<u>7.1</u>	<u>0.57</u>
		B	-5.6	8.2	-18	27	10	0.87

	O ₃ (ppbV)	U	4.9	8.5	16	27	11	0.81
		<u>U+BC</u>	<u>3.1</u>	<u>6.6</u>	<u>10</u>	<u>22</u>	<u>9.2</u>	<u>0.86</u>
Pandora	Tropospheric NO ₂ column (molecules cm ⁻²)	B	7.9E+15	8.6E+15	55	59	9.6E+15	0.71
		U	-6.6E+15	6.8E+15	-46	47	8.2E+15	0.67
		<u>U+BC</u>	<u>-3.8E+15</u>	<u>4.9 E+15</u>	<u>-26</u>	<u>33</u>	<u>6.4 E+15</u>	<u>0.70</u>

672

673 **6.1 Meteorological evaluation: winds and PBL height**674 **6.1.1. Evaluation methodology**

675 To assess the performance of WRF-Chem meteorological fields, modeled wind speed and direction were evaluated against
676 surface observations across the BMR during the ASIA-AQ campaign, 14 – 27 March 2024. Biomass burning was active in the
677 region during the study period, particularly over northern Thailand and Myanmar, with peak activity occurring in mid-March.
678 However, transport to Bangkok was likely limited due to weak synoptic flow and short chemical lifetime of NO_x, reducing its
679 impact on urban concentrations of NO_x in the BMR. Following March 20, precipitation suppressed fire activity, further
680 minimizing its impact. While biomass burning may contribute to broader regional enhancements, its impact on the inversion
681 results and coincident model evaluation over Bangkok is expected to be minor.

682

683

684 Surface observations of wind speed (m s⁻¹) and direction are obtained from Thailand Pollution Control Department (PCD)
685 ground monitor network data. Hourly surface wind observations from PCD network data were co-located with corresponding
686 model outputs for D01 and D02. For each site, model data were extracted from the nearest grid cell and interpolated to
687 observation timestamps. Daily wind roses were constructed to visualize and compare the frequency distribution of wind speed
688 and direction between the model and observations. For each station, wind speeds were binned into intervals of 0-1, 1-3, 3-5,
689 and 5-8 m s⁻¹ and wind directions were grouped into 16 compass sectors. Normalized frequency counts were computed to
690 highlight dominant flow patterns. Data was averaged across stations within a larger bounding box around BMR, N-S (12.5-
691 15°N), W-E (99.5-101.5°E). For meteorology, we use a large box that spans the regional flow influencing Bangkok so that we
692 capture plume transport into and out of the city. Figure S87a illustrates the station locations and averaging domains in Bangkok.

693

694 Additionally, we performed an evaluation of planetary boundary layer height (PBLH) to gauge the model’s ability to capture
695 daily PBLH magnitude and development during the deployment period. Observed PBLHs were derived from [the NASA](#)
696 [Langley](#) airborne [High Spectral Resolution Lidar Generation -2- \(HSRL-2\)](#) data following a machine learning approach
697 described in Christopoulos et al., (2025) for ASIA-AQ flight days, 18 March, 19 March, 23 March, and 25 March 2024. We
698 evaluate PBLHs for aircraft raster periods (i.e., Raster 1: morning, Raster 2: afternoon, Raster 3: late afternoon/evening hours)
699 and co-locate the observed PBLHs to modeled PBLHs based on a nearest grid-cell approximation.
700

701 **6.1.2. Model-observation wind discrepancies**

702 Within the observational data, a pronounced synoptic transition occurred over Thailand on 20 – 21 March 2024, during which
703 winds reversed from the typical southwesterlies that were present during the deployment period to northeasterlies, weakened
704 substantially, coinciding with a drop in PBLH, and increased atmospheric stability (see [PCD](#) observations; Fig. [S98-10](#)). This
705 transition played a major role in PM_{2.5} and ozone exceedances by promoting stagnation over the BMR. The WRF-Chem
706 simulation failed to capture the timing or strength of this abrupt wind shift and associated stagnation (Fig. [S2a, S2b, S9b,](#)
707 [S9c](#)~~[S8a, S8b](#)~~). The model instead maintained stronger southwesterly flow and higher PBLH, which led to unrealistic vertical
708 mixing patterns compared to the observations (Fig. [S98-S104](#)). Since this mismatch drives discrepancies between model and
709 observations that are unrelated to emissions adjustments/inversions, we exclude 20 – 21 March from the inversion/air quality
710 evaluation. Although the simulation is driven by FNL, it is possible for WRF-Chem to mis-time a rapid synoptic transition.
711 This event evolved on a relatively short spatial and temporal scale, and the coarse FNL boundary conditions may not have
712 fully resolved the sharp changes in low-level flow. In addition, local processes (i.e., convection, PBL mixing, land-sea
713 interactions) around Bangkok can cause the model to drift from the observed timing once it is integrated forward. We suspect
714 these factors likely contributed to the later wind shift in WRF-Chem. We additionally found WRF-Chem (D01, D02)
715 systematically overpredicts wind speed throughout the deployment (Fig. [S2a, S2b](#)~~[S8a, S8b](#)~~; Table S2) with better agreement
716 from the high-resolution 4 km domain. This bias likely arises from ~~the~~ fact that many PCD monitors are embedded within
717 the complex urban environment of Bangkok, which are not fully resolved at WRF-Chem’s spatial scale.
718

719 The consequences of this mis-timed synoptic transition are most pronounced on 21 March as demonstrated in the next section,
720 when weak large-scale flow made the simulation highly sensitive to local processes. Under these conditions, WRF-Chem
721 misses the stagnation and dilutes pollutants too quickly. This helps explain why the model performs worst during the highest
722 observed PM_{2.5} and O₃ episode. These results indicate that forecast performance during similar weak-flow pollution events
723 would benefit from improved representation of urban boundary-layer processes (e.g., surface roughness, urban canopy effects,
724 and land–sea breeze structure).

725

726 6.1.3. Model-observation PBLH discrepancies

727 As shown in Fig. S10 and summarized in Table S3, WRF-Chem generally captures the temporal evolution of the PBLH
728 observed by the aircraft. During the daytime (afternoon hours represented by Raster 2-3), the simulated PBL is broadly
729 comparable to the observations, with median values that are often similar. However, the magnitude and sign of the model bias
730 vary by day, with WRF-Chem demonstrating both over- and under- estimation likely related to the meteorological conditions.
731 This day-to-day variability suggests PBLH biases are not systematic during the afternoon and may influence surface pollution
732 dilution differently across individual cases, potentially contributing to variability in simulated daytime NO₂ concentrations
733 rather than a consistent model bias.

734

735 6.2 Surface air quality evaluation

736 To evaluate model performance of surface trace gases, modeled surface mixing ratios of NO₂, NO_x, and O₃ were evaluated
737 against observations across BMR during 14 – 27 March 2024. Surface observations of these constituents (in ppbV) were
738 obtained from Thailand PCD ground monitor network data. Like the evaluation of wind speeds and direction, data was co-
739 located by extracting model information from the nearest grid cell and matched to the observation timesteps. Station data and
740 model data were averaged across stations located within the Bangkok urban plume, bounded by N-S (13.5-14.6°N), W-E
741 (100.2-101°E). Figure S87b illustrates the station locations and averaging domain in Bangkok. For the air quality evaluation,
742 we restrict the station averaging domain to a smaller area over the Bangkok urban plume. This smaller domain allows us to
743 assess how the inversion and optimization specifically correct the local plume structure as opposed to a broader regional
744 background.

745

746 6.2.1. NO₂ and NO_x

747 Figure 7a,7b,7c shows a comparison of average surface NO₂, NO_x, and O₃ (ppbV) for stations located within the Bangkok
748 urban plume during the ASIA-AQ deployment for D02. D01 results are available in Fig. S114. The 20 – 21 March is shaded
749 in grey to indicate the period where the model mis-represented synoptic conditions resulting in enhancements in the observed
750 concentrations due to stagnation. During this time, NO₂, and NO_x, and O₃ reached as high as 49, and 59 ppbV, and 103 ppbV,
751 respectively. O₃ peaked at 103 ppbV the following day, on 22 March. Excluding this event, observed NO₂ and NO_x for this
752 period generally ranged between 3 – 17 ppbV, and 3.5 – 22 ppbV respectively. Overall, there is a clear improvement in the
753 representation of NO₂ and NO_x during this period in WRF_{Updated} and WRF_{Updated+BC} as shown in Fig 7a, 7b. Table 2 depicts
754 summary statistics for this analysis. The baseline simulation, WRF_{Base} overestimates both NO₂ and NO_x with mean biases of
755 +12 ppbV and +14 ppbV, respectively. With updated emissions, these large positive biases in WRF_{Updated} were eliminated and

756 reversed, yielding mean biases of -3.0 ppbV for NO₂ and -3.6 ppbV for NO_x. The remaining negative bias is likely linked to
757 the overprediction of winds, associated advection, and inversion related biases, which leads to locally diluted concentrations
758 near urban sites as shown in the previous analyses. WRF_{Updated+BC} further reduces the residual bias related to WRF_{Updated},
759 bringing mean biases closer to zero (e.g., +0.1 ppbV for NO₂ and +0.02 ppbV for NO_x), while maintaining comparable error
760 and correlation, indicating accounting for the GEMS retrieval bias prior to inversion provides a modest additional improvement
761 in model performance. Correlations with observed NO₂ and NO_x remain moderate ($r = 0.5\text{--}0.6$) reflecting potential spatial
762 discrepancies in WRF_{Updated} as seen in the previous analyses. Average diurnal cycles of NO_x for D02, D01 are further illustrated
763 in Fig. S12a, c. Observed NO_x shows a clear morning peak and lower midday concentrations driven by boundary layer
764 evolution. WRF_{Base} overestimates NO_x and exaggerates the morning peak while WRF_{Updated} (dark purple) substantially
765 improves both magnitude and timing but underestimates the evening peak values. WRF_{Updated+BC} shows mixed performance
766 with an overprediction of the morning peak while the evening peak aligns more closely with observations compared to
767 WRF_{Updated}, indicating a trade-off in how the bias correction might redistribute NO_x across the diurnal cycle in the updated
768 models.

770 6.2.2. O₃

771 Observed O₃ generally ranged between 14–57 ppbV, excluding the stagnation event on 20 – 21 March, and the baseline model
772 captures this range reasonably well (Fig. 7c). After updating the emissions, O₃ increases in WRF_{Updated} and WRF_{Updated+BC}
773 primarily at night, consistent with reduced NO titration following the decrease in NO_x emissions. Average diurnal cycles in
774 D02 (Fig. S12ab,d) show that daytime O₃ production changes only modestly between base and updated simulations, indicating
775 the emission update mainly affects nighttime chemistry, as opposed to shifting photochemical O₃ formation in the daytime.
776 This pattern is reflected in the change in overall mean bias in Table 2, which shifts from an underprediction (-5.6 ppbV) to an
777 overprediction (+4.9 ppbV) in WRF_{Updated}. The overprediction is not as substantial in WRF_{Updated+BC} (+3.1 ppbV). While
778 WRF_{Updated} exhibits an earlier O₃ peak in D02 compared to observations, this shift is not present in D01 despite the same
779 emission inversion being applied. This likely suggests the discrepancy is driven by domain-dependent differences in
780 meteorological or chemical processes, rather than an error in the inferred NO_x emission timing. The O₃ peak is better
781 represented in WRF_{Updated+BC}.

782
783 The relatively weak daytime O₃ response to decreased NO_x emissions is consistent with recent analyses of O₃ formation
784 sensitivity during ASIA-AQ with in situ measurements, which indicate that the BMR exhibits mixed sensitivity to NO_x and
785 VOCs, in contrast to the predominantly NO_x-limited regimes observed at other ASIA-AQ locations (e.g., Manila) (Cho et al.,
786 2026). In this mixed-sensitivity regime, changes in NO_x emissions alone are not expected to strongly perturb daytime O₃
787 production, further providing validation for the minimal daytime O₃ response observed here. The magnitude of the daytime O₃

788 response varies by domain/model as shown by the D01 results (Fig. S12d+2b). Although WRF_{Updated} D01 better matches
789 observed daytime O₃, this apparent improvement likely reflects NO_x titration associated with spatial dilution.

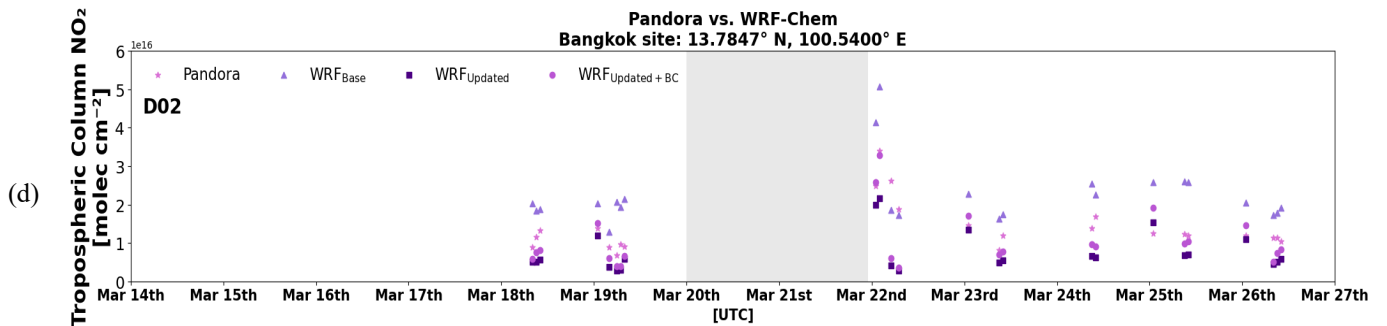
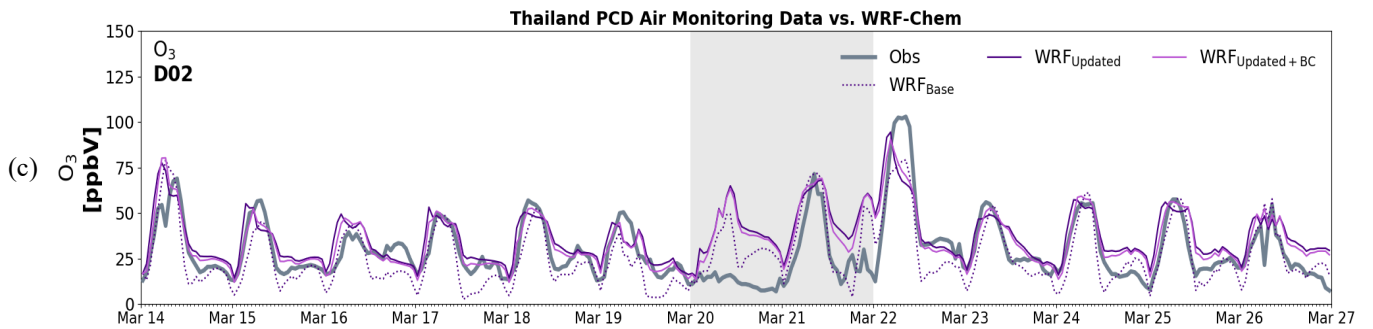
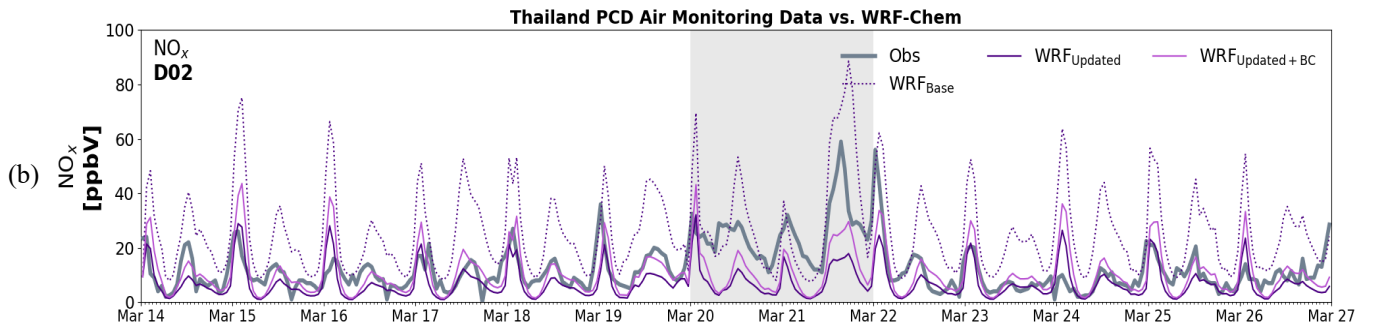
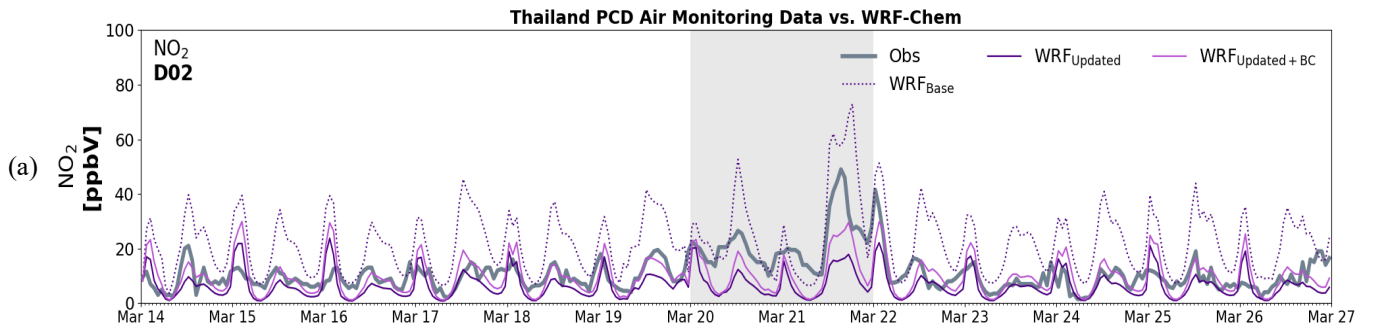
791 Overall, these results suggest that while the updated emissions improve the model's NO_x representation, further improvements
792 in VOC representation and local mixing processes may be needed to fully capture daytime O₃ levels in the BMR. Nevertheless,
793 the updated emissions substantially improve the model's simulation of surface NO₂ and NO_x, resulting in a more realistic
794 overall representation of air quality in Bangkok.

796 6.3 Evaluation with Pandora column observations

797 We additionally evaluate modeled NO₂ columns against Pandora measurements for the Bangkok site. Pandora NO₂ evaluation
798 used Level 2 direct-sun total column retrievals, filtered for high-quality measurements (quality flag = 10), and averaged to
799 hourly means. Tropospheric columns from Pandora were estimated by subtracting coincident or closest GEMS stratospheric
800 NO₂ at the nearest satellite pixel. Model columns were sampled at the nearest grid cell to the Pandora site and temporally
801 matched to observations.

803 Figure 7d depicts a comparison of WRF_{Base} (light purple triangles), WRF_{Updated} (dark purple squares), WRF_{Updated+BC} (magenta
804 dots) and Pandora (pink stars), tropospheric NO₂ column measurements for days with high quality data. Throughout this period,
805 Pandora measurements generally ranged between approximately $7 \times 10^{15} - 3.5 \times 10^{16}$ molecules cm⁻² and fit between WRF_{Base}
806 which places columns higher (e.g., up to 5×10^{16} molecules cm⁻²), WRF_{Updated+BC}, and ~~and~~ WRF_{Updated} which places columns
807 lower (e.g. 2×10^{15} molecules cm⁻²). Average statistics between model cases for this analysis are shown in Table 2. Biases are
808 generally similar between model cases. WRF_{Base} overestimates column NO₂ as illustrated by the mean bias ($+7.9 \times 10^{15}$
809 molecules cm⁻²) whereas emissions updates contribute to an underestimation (-6.6×10^{15} molecules cm⁻²). However, there are
810 some improvements in absolute error metrics with ME and RMSE decreasing by roughly 20% and 12% respectively, and NME
811 dropping from 61% to 48%. The greatest bias improvements overall are seen in WRF_{Updated+BC} (-3.8×10^{15} molecules cm⁻²).
812 Figure S13+4 illustrates the spatial distribution of mean tropospheric model NO₂ bias for GEMS and Pandora during the time
813 reflected in Fig. 7d. In the WRF_{Base} simulation, a strong positive bias is seen within and north of the Pandora site, indicating
814 the overestimation of NO₂ columns (up to 2×10^{16} molecules cm⁻²) in the urban plume relative to GEMS. This pattern reiterates
815 the point that the prior anthropogenic emissions (based on EDGAR v5) were too large with pollutant accumulation occurring
816 downwind of Bangkok as a result. After applying the emission updates, the WRF_{Updated}, simulation essentially eliminates this
817 bias. The overall bias near the Pandora site becomes close to neutral or slightly negative, demonstrating the optimization
818 effectively corrected the spatial overprediction. WRF_{Updated+BC} further reduces the residual negative bias relative to WRF_{Updated}
819 with NMB improving from -46% to -26% and RMSE decreasing from 8.2×10^{15} to 6.4×10^{15} molecules cm⁻². This indicates
820 that accounting for the GEMS retrieval bias in the initial optimization process partially corrects the remaining underestimation.

821 ~~although some spatial discrepancies persist due to transport and plume placement error. The remaining negative bias close~~
822 ~~to the city center/Pandora site is likely related to discrepancies in the WRF_{Updated} urban plume placement, overpredicted wind~~
823 ~~speeds, and inversion biases related to the GEMS retrievals. Examples of ~~D~~daily biases for WRF_{Base} D01, D02, and WRF_{Updated}~~
824 D01, D02 can be found in Fig. S1415 and Fig. S1516.



825
826
827
828

829

830

831

832

833

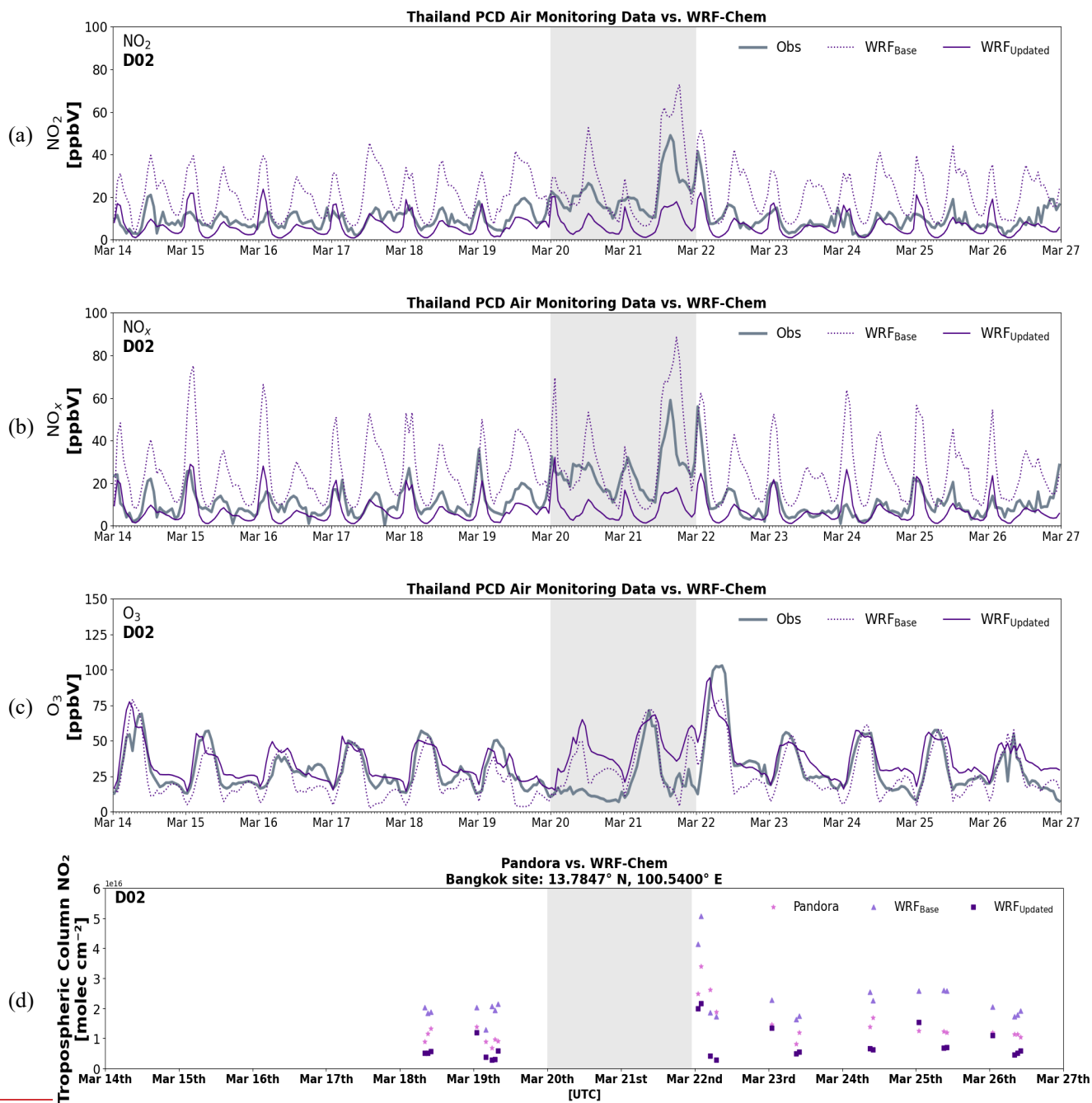


Figure 7. Comparison of WRF_{Base} D02 (dotted purple), ~~and~~ WRF_{Updated} D02 (solid purple), and WRF_{Updated}+BC D02 (solid magenta) simulations against Thailand Pollution Control Department (PCD) ground-monitor network observations for (a) NO₂ mixing ratio (ppbV), (b) NO_x mixing ratio (ppbV), and (c) O₃ mixing ratio (ppbV) during the ASIA-AQ deployment period

839 (14 – 27 March 2024). represent averages across stations within the Bangkok urban plume. (d) Comparison of tropospheric
840 NO₂ columns from WRF_{Base} D02 (light purple [triangles](#)), WRF_{Updated} D02 (dark purple [squares](#)), [WRF_{Updated+BC} D01 \(magenta](#)
841 [dots](#)) and Pandora (pink [stars](#)) for high-quality observations during the ASIA-AQ deployment period (18 – 27 March 2024).
842 The shaded region represents the stagnation period, 20 – 21 March excluded from the evaluation.

843

844 **6.4 Evaluation with ASIA-AQ aircraft measurements**

845 The Airborne and Satellite Investigation of Asian Air Quality (ASIA-AQ) was a NASA field campaign conducted in February
846 – March 2024 to advance the understanding of urban and regional air quality across East and Southeast Asia. Targeting several
847 megacities (e.g., Manila, Seoul, Bangkok, Chiang Mai), the campaign combined satellite observations, aircraft measurements,
848 ground-based monitoring, and modeling approaches to characterize pollution sources and validate satellite retrievals. A main
849 objective of ASIA-AQ was to evaluate the data from GEMS. Airborne observations were collected using the NASA DC-8 in
850 situ and LaRC G-III remote sensing aircraft, with coordinated support from ground-based networks such as Pandora and
851 AERONET. Additionally, chemical transport models (e.g., GEOS-Chem, GEOS-FP, MUSICA, WRF-Chem, WRF-CMAQ)
852 played a key role in real-time flight planning and post-campaign interpretation.

853

854 **6.4.1. GCAS**

855 The GEOstationary Coastal and Air Pollution Events (GEO-CAPE) Airborne Simulator (GCAS) is an airborne UV-Vis
856 spectrometer that was flown on the G-III aircraft during the ASIA-AQ campaign. GCAS was designed to simulate the
857 spectral capabilities of TEMPO and GEMS, but with a much finer pixel resolution of approximately 250 x 560 m at flight
858 altitude (Janz et al., 2019; Lee et al., 2024). GCAS uses a push-broom remote sensing technique and consists of two
859 spectrometer channels: a UV-Vis channel (300-490 nm) optimized for air quality measurements, and a Vis-NIR channel (480-
860 900 nm) for ocean color observations (Kowalewski and Janz, 2014; Lee et al., 2024). This work focuses on the NO₂ retrieval
861 from spectra in the UV-Vis channel. Retrieval details and validation results can be found in Judd et al., (2020) but were
862 previously found to be unbiased with uncertainties within +/-25%. As in previous field campaigns, the aircraft executed a
863 “lawnmower” flight pattern with parallel flight lines spaced 6.3 km apart, providing about 10% overlap between flight lines
864 assuming a flight altitude of 28,000 feet. This flight strategy, combined with the instrument’s 45° field of view, allowed for
865 the generation of gap-free NO₂ column maps up to three times per day, period referred to as a “raster”. Due to the short duration
866 of each raster period (~3 hours), local meteorological conditions often influence the fine-scale structures observed in the GCAS
867 NO₂ data (Goldberg et al., 2024). Here, we evaluate the WRF-Chem runs against GCAS for several flight days: 18 March, 19
868 March, 23 March, and 25 March 2024.

869

870 We perform the evaluation for each raster separately to isolate specific flight patterns and accurately evaluate spatial gradients
 871 in NO₂ between the model and observations. For each analysis, GCAS pixels corresponding to the flagged raster were retained
 872 for comparison. Additional filters were applied to remove poor-quality retrievals. We masked pixels with cloud or sun glint
 873 contamination based on a provided flag variable (`cloud_glint_flag = 1`) and discarded retrievals with missing data or undefined
 874 AMFs. GCAS provides separate NO₂ vertical columns above and below the aircraft, as well as model-derived scattering
 875 weights, and AMFs for both portions. The above and below aircraft contributions can be approximated as the stratospheric
 876 and tropospheric contributions, respectively. For this evaluation, we focus exclusively on the NO₂ column below the aircraft
 877 or the tropospheric column NO₂, which is the portion most relevant to surface-level air quality and most comparable to our
 878 WRF-Chem results. We compute the below-aircraft averaging kernel, A_i^{below} , as:

$$A_i^{below} = \frac{SW_i}{AMF_{below}} \quad (17)$$

879
 880 Here, SW_i represents the scattering weight for layer i , representing the sensitivity of the measured radiance to NO₂ in that
 881 layer. This averaging kernel represents the satellite-equivalent vertical sensitivity to NO₂ below the aircraft and was used to
 882 weigh the WRF-Chem vertical profile.

883
 884 WRF-Chem output including, NO₂ mixing ratio, pressure, temperature, and height were used to compute air density and
 885 convert volume mixing ratios to number densities as previously done in the GEMS evaluation. Each GCAS pixel was
 886 temporally matched to the nearest model output time (rounded to nearest hour) and spatially co-located by finding the nearest
 887 WRF-Chem grid cell. To isolate the portion of the model column below the aircraft, we filtered the model levels based on the
 888 aircraft altitude reported at each pixel. We compute the tropospheric column as shown in Eq. (10). To generate a model column
 889 that reflects the vertical sensitivity of the GCAS retrieval, we interpolate the WRF-Chem profile to the number of GCAS
 890 vertical layers (49), converted the mixing ratios to number density, and applied the GCAS averaging kernel to yield WRF-
 891 GCAS.

892
 893 The maps in Fig. 8 illustrate a spatial comparison between (a) GCAS, (b) WRF-GCAS_{Updated+BC D02}, (c) WRF-GCAS_{Updated}
 894 D02, and (d) WRF-GCAS_{Base D02} over BMR for a flight day on 18 March 2024. D01 spatial comparisons are available in
 895 Fig. S16. 18 March represents a typical example of local pollution dominating BMR with minimal influences from long-range
 896 pollution transport and biomass burning. The GCAS instrument generally places tropospheric column NO₂ values in BMR
 897 between $5 \times 10^{15} - 2 \times 10^{16}$ molecules cm⁻², with the largest enhancements observed in the city center, as also seen in the
 898 GEMS data (Fig. 7). A clear N-S plume is visible in the data, reflecting persistent southerly onshore flow from the Gulf of
 899 Thailand. This pattern coincides with the seasonal shift from the northeast to southwest monsoon. Overall, WRF-GCAS_{Updated}
 900 and WRF-GCAS_{Updated+BC} can generally better capture the spatial differences and magnitudes of tropospheric column NO₂ in
 901 BMR for different raster periods compared to WRF-GCAS_{Base}. WRF_{Updated+BC} outperforms WRF_{Updated} in capturing NO₂ column
 902 enhancements, particularly during raster 2 (late morning – afternoon LT). GCAS also illustrates enhanced NO₂ columns

903 southeast of Bangkok in a region known as the Eastern Economic Corridor (EEC), a major hub for industrial activity (e.g.,
904 automotive manufacturing, petrochemicals, electronics). WRF_{Updated}, WRF_{Updated+BC}, and WRF_{Base} tend to underestimate
905 pollution levels in the EEC. This is likely related to wind speed overprediction and a lack of updated regional source data in
906 the EDGAR v5 inventory (since this is a region outside of the performed inversion). Information from a local emissions
907 inventory, or additional inversions performed on this region could aid the model in better representing the air quality in this
908 region, which has similar magnitudes of column NO₂ (2×10^{16} molecules cm⁻²) to the Bangkok city center.

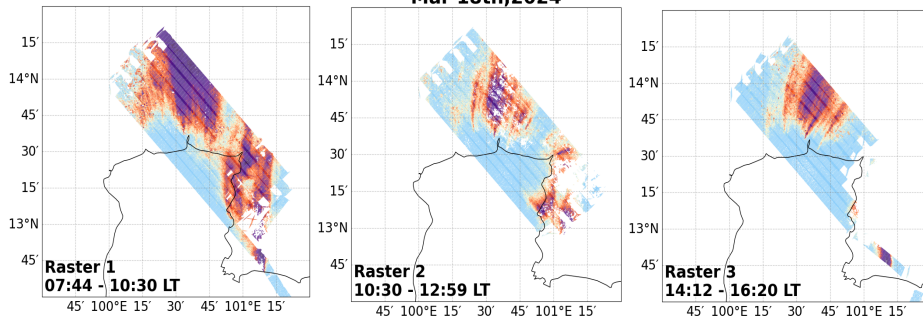
909
910 Statistics for this analysis are shown in Table 2. Overall, statistics are representative of substantial bias and error improvements
911 in the updated runs from WRF_{Base}, which significantly overpredicts column NO₂ amounts in the region for all raster periods.
912 For example, ME and RMSE are improved by ~62% from WRF_{Base} and WRF_{Updated}. Mean biases are negative which indicate
913 WRF_{Updated} is underpredicting NO₂ columns. This is likely the result of the low inversion biases and windspeed overprediction.
914 However, this underprediction is improved throughout the day as seen in Fig. S1720a, S1720b. This is in opposition to
915 WRF_{Base}, which increases in biases and error for each raster as also shown in Fig. S1720a, S1720b. These daytime patterns
916 also highlight an important distinction between the benefits of geostationary (GEMS) versus LEO observations. Morning
917 improvements are particularly strong because the inversion directly constrains the rapid rise in emissions during the morning,
918 something that LEO sensors generally under sample due to their limited overpass frequency. Midday and afternoon
919 performance remains improved as well, but the morning hours show the clearest advantage of daytime GEO sampling for
920 capturing short-timescale emission variability. Similar results are demonstrated in WRF_{Updated} D01 (Fig. S18). WRF_{Updated+BC}
921 is indicative of a partial correction to the negative bias in WRF_{Updated}, shifting the NMB from -5.6% to +16%. While this brings
922 the simulated NO₂ columns closer to observations in a mean sense, is it followed by increases in error, suggesting a trade-off
923 between bias reduction and overall model performance.

924
925 Correlations remain moderate high (0.40-6 – 0.60-8) for ~~both~~ model cases, however, WRF_{Updated} and WRF_{Updated+BC} illustrate
926 has weaker correlations likely due to (i) subtle shifts in the urban plume placement (i.e., shift in a more northerly direction),
927 and (ii) a reduction in dynamic range after emissions corrections. For example, when plume magnitudes are lowered, the
928 variability shrinks allowing the correlations to become less sensitive to spatial-temporal agreement and more sensitive to small
929 plume-placement differences as is the case here.

Mar 18th, 2024

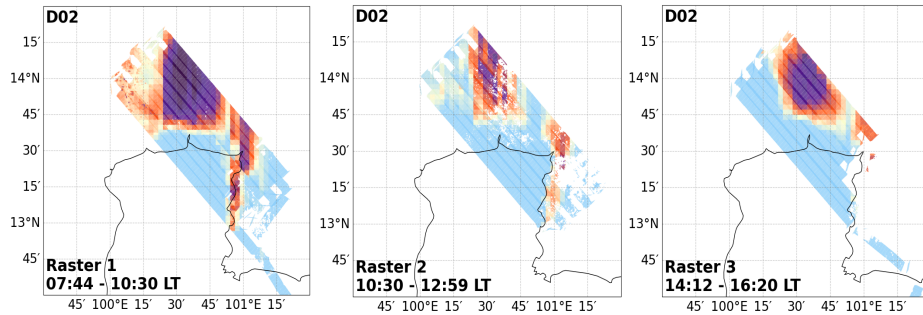
(a)

GCAS



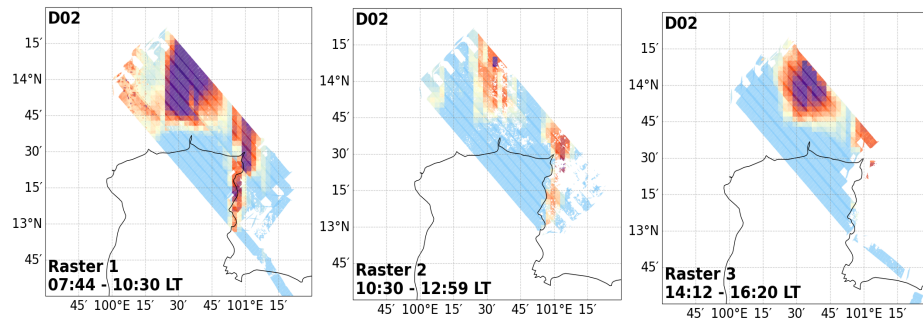
(b)

WRF-GCAS_{Updated + BC}



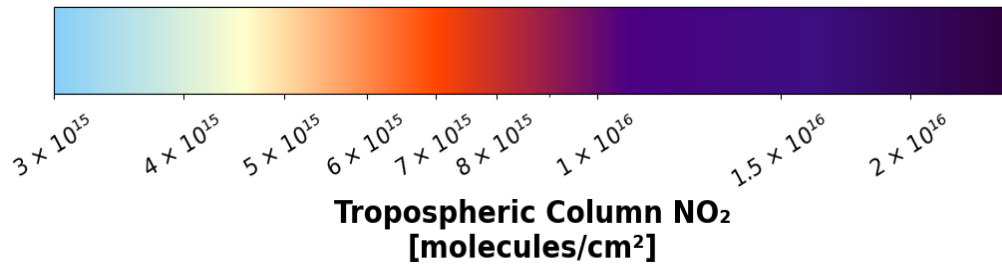
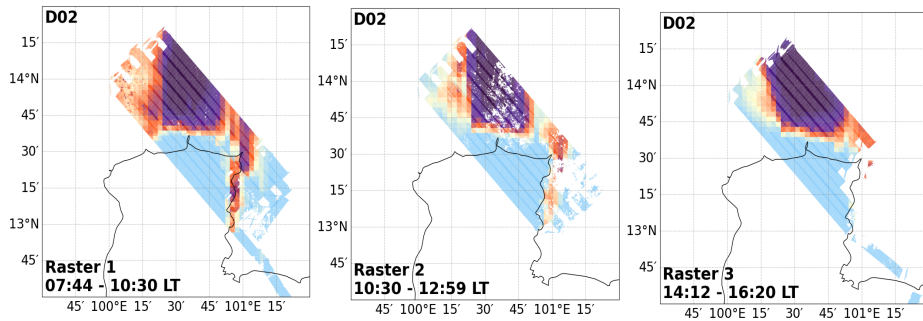
(c)

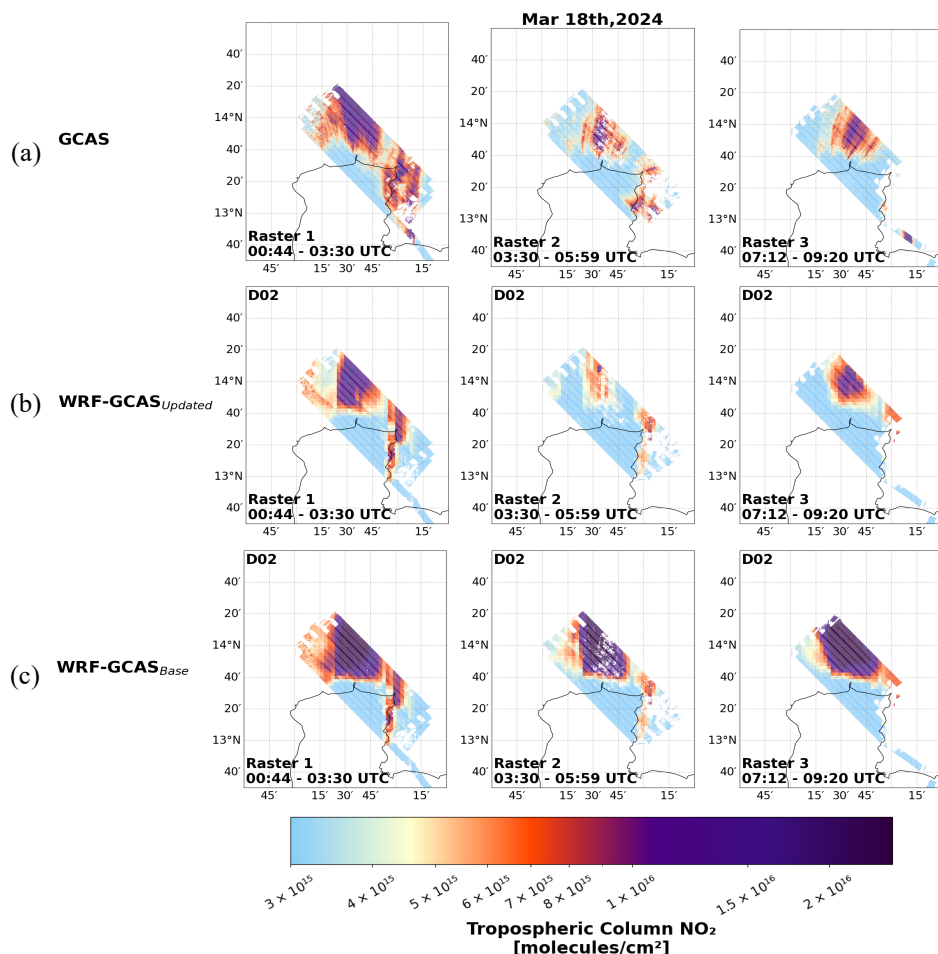
WRF-GCAS_{Updated}



(d)

WRF-GCAS_{Base}





932
 933 **Figure 8.** Spatial comparison over the BMR on 18 March 2024 of tropospheric NO₂ columns from (a) GCAS, (b) WRF-
 934 GCAS_{Updated+BC} D02, (c) WRF-GCAS_{Updated} D02 and (d) WRF-GCAS_{Base} D02 for raster periods corresponding to morning,
 935 afternoon, and early evening local time.

936 6.4.2. NO_xO₃ and CANOE (DC-8)

937 We additionally compare the model simulations to in situ NO₂ data gathered by the National Center for Atmospheric
 938 Research's (NCAR) NO_xO₃ and NASA's GSFC's Compact Airborne NO₂ Instrument (CANOE) aboard the DC-8 aircraft. The
 939 NO_xO₃ instrument is a 3-channel chemiluminescence instrument designed for the measurement of NO, NO₂, and O₃ (Ridley
 940 et al., 1992; Ridley and Grahek, 1990). CANOE measures NO₂ using non-resonant laser induced fluorescence (LIF) (St. Clair
 941 et al., 2019). We use the 1-sec DC-8 data for the flights conducted in Thailand during March 2024 (18 March, 25 March). A
 942 visual depiction of the DC-8 flight path is shown in Fig. S19-17a, 17b. The typical flight path included several low-altitude
 943 descents/ascent over several airports (see Fig. S19-17b) along with long-distance transects across Central Thailand.

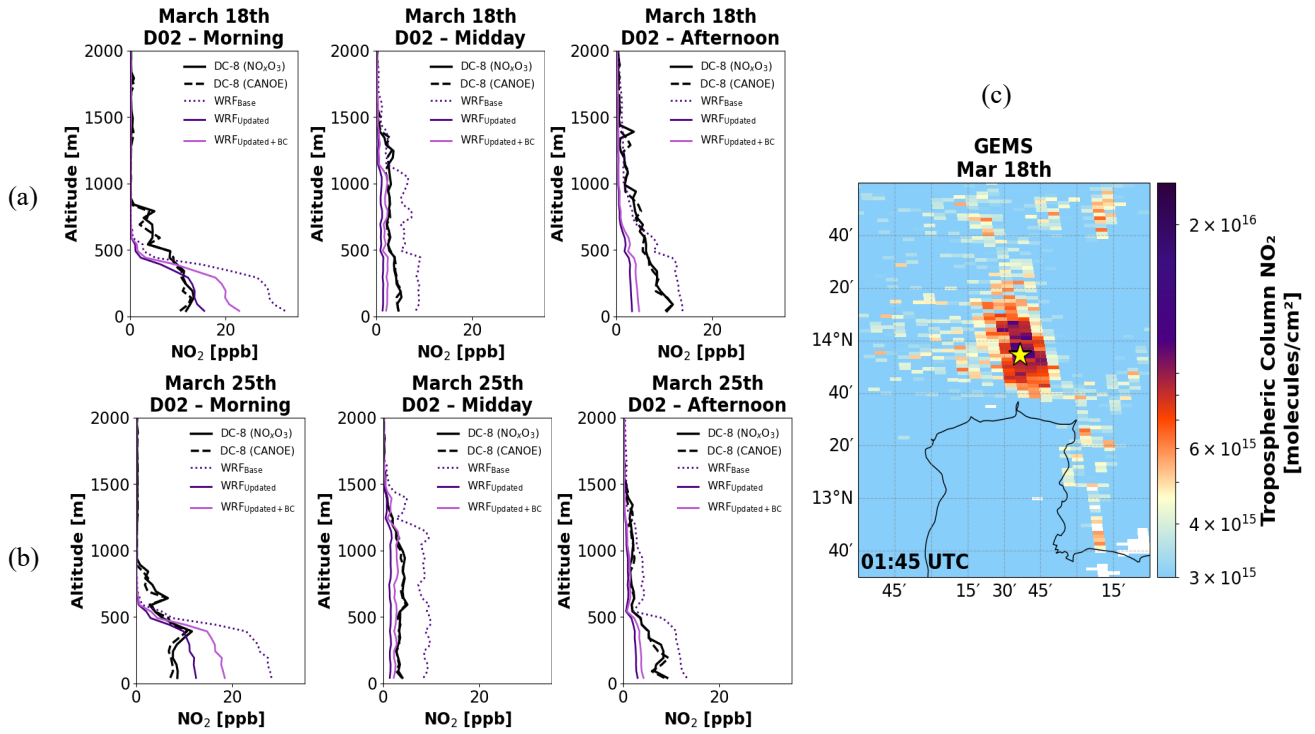
945 To evaluate model performance, we match hourly WRF-Chem outputs from both the 20 km (D01) and 4 km (D02) domains
946 to the aircraft location and time. For each observation, we extract co-located model NO₂ values along the aircraft track. Profiles
947 are filtered by location (e.g., Don Mueang International Airport in Bangkok) and direction (e.g., ascent or descent) using flags
948 in the provided observational datasets. Individual profiles are grouped by their unique number, and we bin the observations
949 and model output by altitude (50 m vertical bins). For each bin, we compute mean NO₂ from the aircraft and model datasets.
950 These vertically resolved comparisons allow us to assess model skill in capturing the observed structure and magnitude of NO₂
951 within the boundary layer and lower troposphere.

952
953 Figure 9 depicts a comparison of aggregated in situ NO₂ vertical profiles over the Don Mueang International airport for (a) 18
954 March and (b) 25 March. Model scenarios are shown in shades of purple (WRF_{Base}: dotted dark purple; WRF_{Updated}: solid dark
955 purple; WRF_{Updated+BC} solid magenta), and in situ information from two instruments aboard the DC-8, NO_xO₃ (solid) and
956 CANOE (dashed) are displayed in black. The location of the Don Mueang International Airport with respect to the Bangkok
957 urban plume is depicted in (c). We separate and group the data by time of day to gauge how the model runs perform with
958 respect to time of day. Corresponding plots for D01 are available in Fig. S20. As shown in Fig. 9, the NO_xO₃ and CANOE
959 NO₂ measurements exhibit excellent agreement throughout the analysis period. This consistency between two independent in
960 situ instruments strengthens confidence in the observational data used for model evaluation. Comparison with DC-8 in situ
961 NO₂ profiles show that WRF_{Base} consistently overestimated observed concentrations, with a mean bias of +1.3 ppb and
962 normalized mean bias near 80%. Figure 9a and Figure 9b indicate the overestimation is most pronounced near the surface
963 during the morning, where WRF_{Base} exceeds observations by nearly 25 ppb. WRF_{Updated+BC} also suggests an overestimation
964 compared to aircraft observations in the morning. In contrast, WRF_{Updated} captures the observed morning surface enhancements
965 accurately. As time progresses, however, WRF_{Updated} and WRF_{Updated+BC} begins to underestimate the column (average bias ~ -
966 0.3 to -0.8 ppb), though both mean error and RMSE remain improved in the updated cases relative to WRF_{Base} (Table 2). This
967 daytime behavior likely reflects the nature of the GEMS-based emission constraints, which are directly applied only until
968 14:00:00 LT, after which a single daily scaling factor is applied on the input emissions. As afternoon PBL growth and
969 photochemistry evolve, the fixed scaling likely results in an underestimation in the afternoon profiles. Additionally,
970 overestimated model winds speeds may further dilute surface concentrations, likely contributing to the midday and afternoon
971 biases shown in WRF_{Updated}, and WRF_{Updated+BC}. The afternoon underestimation is slightly reduced in WRF_{Updated+BC}, likely
972 reflecting the impact of the bias correction applied prior to inversion/NO_x emission optimization.

973
974 Correlations for WRF_{Updated} (r = 0.93 – 0.97) and WRF_{Updated+BC} (r = 0.94) remain high (~~r = 0.93 – 0.97~~) indicating the simulation
975 preserved the observed structure while improving the overprediction. Overall, these results highlight the effectiveness of the
976 emission updates in accurately capturing morning surface air quality. This suggests that while the updated emissions
977 substantially improve the magnitude of modeled NO₂, remaining discrepancies are driven primarily by meteorological
978 transport rather than emission magnitude.

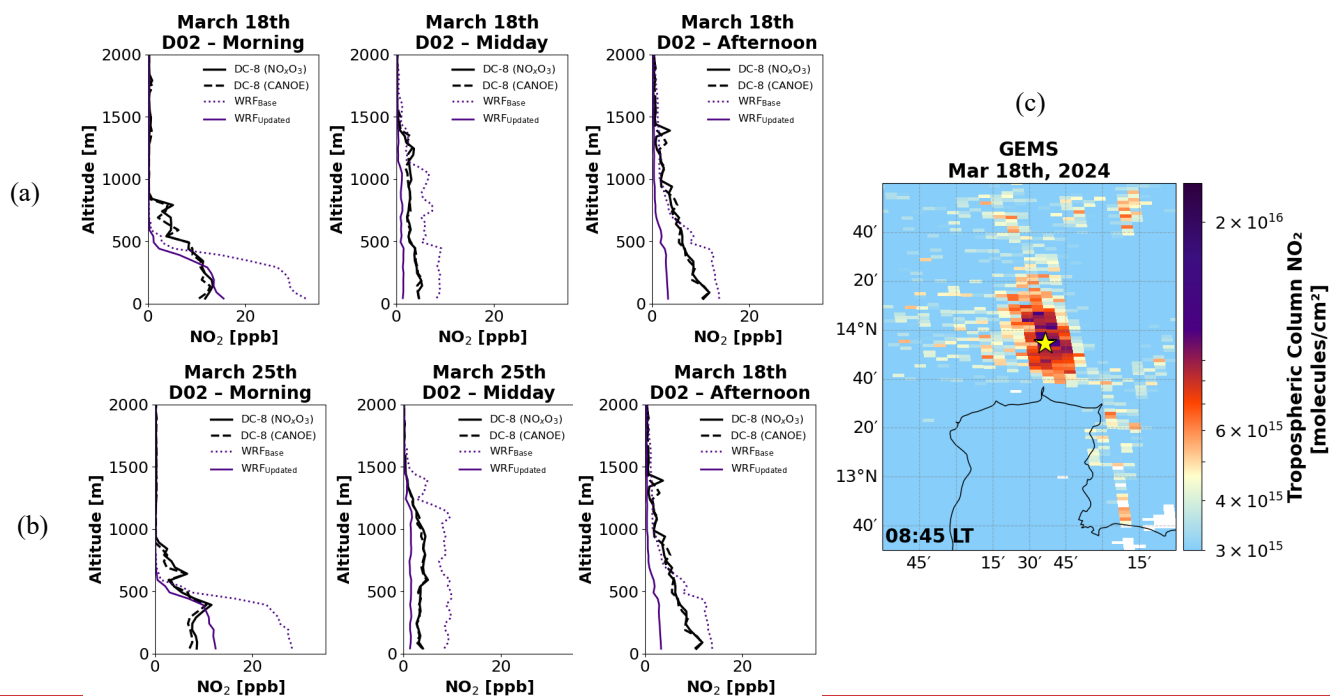
979

980



981

982



984

985 **Figure 9.** Comparison of WRF-Chem D02 simulations (WRF_{Base}: dotted dark purple; WRF_{Updated}: solid dark purple;
 986 WRF_{Updated+BC}: solid }magenta) with airborne in situ measurements from the CANOE (dashed black) and NO_xO₃ (solid black)
 987 instruments aboard the DC-8 for (a) 18 March and (b) 25 March 2024. Profiles are grouped by morning (06:00:00–11:00:00
 988 LT), midday (11:00:00–13:00:00 LT), and afternoon (13:00:00–17:00:00 LT) approaches at Don Mueang International Airport
 989 in northern Bangkok, whose location relative to the Bangkok urban plume is shown within a GEMS snapshot in (c).

990

991 7 Discussion

992 7.1 Implications of GEMS NO₂ retrieval biases

993 Comparisons between GEMS tropospheric NO₂ columns and independent column references indicate a systematic low bias in
 994 the GEMS product, particularly over the Bangkok region. In our analysis during ASIA AQ, GEMS total NO₂ columns are
 995 generally lower than coincident Pandora total column NO₂ observations (Fig. S13) (mean bias $\approx -9.2 \times 10^{15}$ molecules cm⁻²),
 996 consistent with recent independent validation studies of the operational GEMS v3 product over Bangkok and South Korea that
 997 report low biases relative to ground-based sun-photometer and DOAS measurements (Bae et al., 2025; Jung et al., 2025). Bae
 998 et al. (2025) shows that GEMS v3 increasingly underestimates NO₂ relative to Pandora under high NO₂ conditions ($>1 \times 10^{16}$
 999 molecules cm⁻²) as is the case for Bangkok pollution levels. In Jung et al. (2025), validation results over Bangkok indicate a

1000 pronounced low bias in GEMS tropospheric NO₂ columns relative to Pandora, with regression slopes of -0.35 for v2.0 and
1001 -0.28 for v3.0, indicating increasing underestimation at higher NO₂ levels. While moderate correlations ($r \approx 0.6-0.7$) suggest
1002 that GEMS captures temporal variability, column magnitudes are substantially underestimated, particularly under polluted
1003 conditions. The persistence of this behavior in the v3.0 product indicates that the low bias is not fully corrected by recent
1004 algorithm updates and is consistent with retrieval sensitivity limitations in highly polluted urban environments (Jung et al.,
1005 2025).

1006 ~~To further evaluate the relative behavior of GEMS and airborne GCAS NO₂ columns, we compare their tropospheric columns~~
1007 ~~using WRF_{Updated} as a common transfer framework (Fig. 10). Figure 10 compares the observed GCAS/GEMS NO₂ column~~
1008 ~~ratios with ratios calculated after both datasets are mapped through WRF_{Updated}. In the observations, GCAS columns are~~
1009 ~~consistently higher than GEMS, with GCAS/GEMS ratios of ~2-3 on most days and values reaching ~6-7 on 21 March. In~~
1010 ~~contrast, the corresponding WRF-GCAS_{Updated}/WRF-GEMS_{Updated} ratios are substantially smaller (~1.1-1.7), even on 21~~
1011 ~~March. This is consistent with a low bias in GEMS NO₂ columns as found in previous comparisons.~~

1012 In our study, the comparisons with independent aircraft and ground-based observations indicate the satellite-constrained
1013 emissions without bias-corrections presented here may represent a low estimate. In particular, the systematic low bias in GEMS
1014 NO₂ is consistent with the negative biases often seen in the WRF_{Updated}, updated simulations. Importantly, this bias could not
1015 be diagnosed using the satellite data alone.

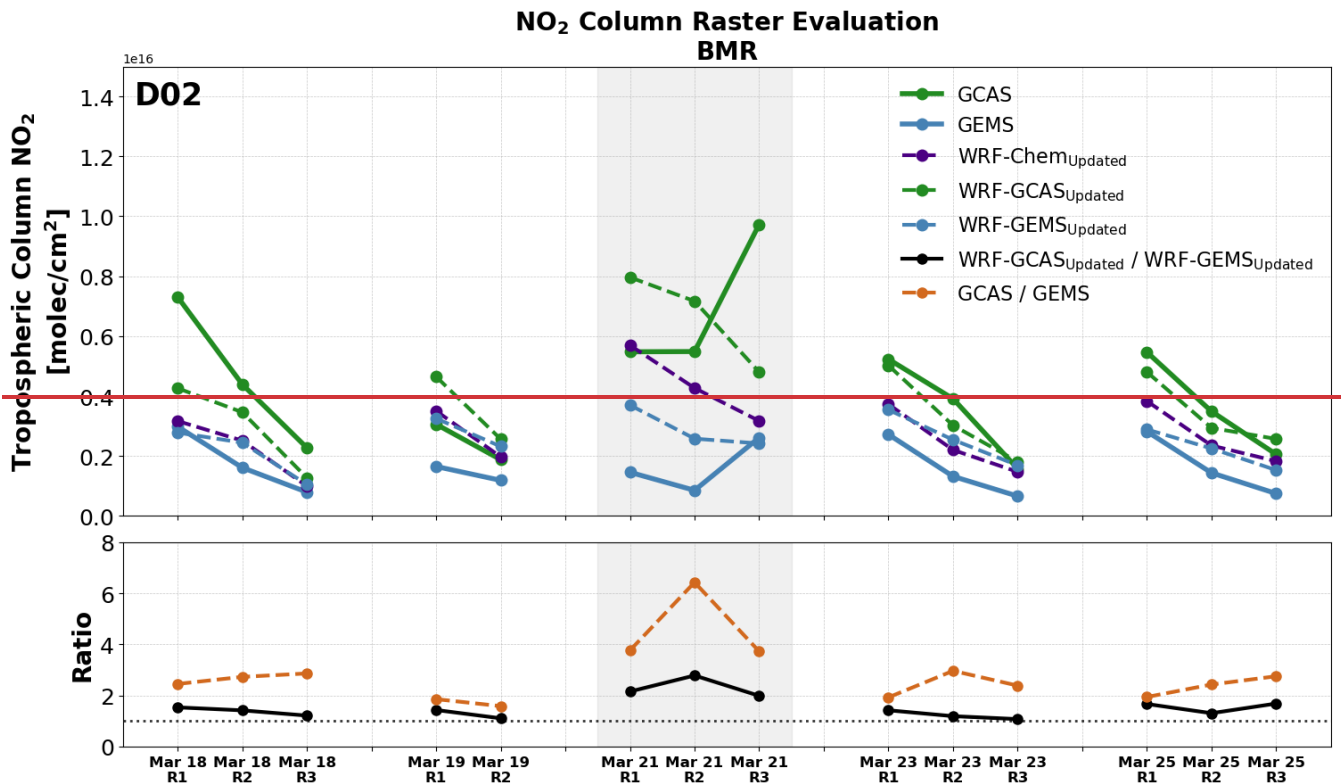
1016 To further evaluate the relative behavior of GEMS and airborne GCAS NO₂ columns, we compare their tropospheric columns
1017 using WRF_{Updated+BC} as a common transfer framework (Fig. S21+0). Figure S21+0 compares the observed GCAS/GEMS NO₂
1018 column ratios with ratios calculated after both datasets are mapped through WRF_{Updated+BC}. In the observations, GCAS columns
1019 are consistently higher than the raw GEMS columns as illustrated by the orange line, with GCAS/GEMS ratios of ~2-3 on
1020 most days and values reaching ~6-7 on 21 March. In contrast, the corresponding WRF-GCAS_{Updated+BC}/WRF-GEMS_{Updated+BC} ratios
1021 are closer to 1:1 substantially smaller (~1.1-1.7), even on 21 March. This is consistent with a low bias in GEMS NO₂
1022 columns as found in previous comparisons. This behavior is consistent with a low bias in GEMS NO₂ columns relative to
1023 GCAS. After applying the bias correction, the GCAS/GEMS_{BC} ratios approach 1:1 on most days, indicating improved
1024 consistency between the datasets, and supporting the effectiveness of the applied GEMS bias correction.

1025 When incorporating bias-corrected retrievals into the top-down inversions and NO_x emission optimization process, the
1026 resulting WRF_{Updated+BC} run reduces the negative biases in the independent validation, in some cases bringing the model results
1027 even closer to observations as seen in the surface air quality analysis. However, this improvement is not uniform. In certain
1028 comparisons (e.g., GCAS and DC-8), WRF_{Updated+BC} introduces a tendency toward overprediction in morning hours,
1029 highlighting tradeoffs associated with the bias correction. These results suggest that while accounting for the retrieval bias can

1030 improve mean model performance, additional uncertainties such as overestimated wind speeds and associated transport errors
1031 continue to influence the representation of modeled NO₂.

1032 Here, the integration of ground-based, airborne, satellite, and model data provides a powerful framework not only for
1033 improving emissions but also for identifying limitations within individual observing systems. While WRF_{Updated} clearly
1034 outperforms the baseline model, and WRF_{Updated+BC} offers targeted improvements in reducing systematic bias, the combined
1035 observational evidence highlights the necessity of a multi-platform validation to fully interpret the satellite-based emission
1036 estimates.

1037 Despite this low bias in the GEMS retrieval, the high-frequency daytime sampling provided by geostationary observations
1038 offers critical constraints on daytime variability and plume evolution that are particularly valuable for emission inversion and
1039 air quality modelling. For example, the GEMS-constrained emission adjustments presented here were critical for improving
1040 the temporal evolution of NO_x in WRF-Chem, resulting in substantial and robust improvements in model performance across
1041 independent evaluations. Future work may further benefit from continued refinement of bias-corrected GEMS products and
1042 upcoming algorithm improvements (e.g., v4), alongside improved representation of spatial representation of emissions within
1043 the model. ~~the application of bias corrected GEMS products or future GEMS algorithm updates and corrections (e.g., v4~~
1044 ~~products).~~



1045
1046
1047 **Figure 10.** Daily raster (e.g., R1, R2, R3) comparison of tropospheric NO₂ columns from WRF_{Updated}-D02 (dashed purple),
1048 WRF-GCAS_{Updated}-D02 (dashed green), WRF-GEMS_{Updated}-D02 (dashed blue), GCAS (green), and GEMS (blue) for ASIA-
1049 AQ flight days. Dashed model lines indicate simulations with instrument specific averaging kernels applied. The bottom panel
1050 illustrates the ratio GCAS/GEMS (orange) and WRF-GCAS/WRF-GEMS (black).
1051

1052 7.2 Limitations and potential extensions of the inversion framework

1053 The current model emission update framework optimizes the temporal evolution of emissions but does not explicitly resolve
1054 regional variability, as a single set of hourly scaling factors is applied uniformly across all grid cells within the BMR. As a
1055 result, the inversion preserves the spatial structure of the prior inventory, and any inaccuracies in the spatial distribution of
1056 emissions are not corrected.

1057
1058 Extending this approach to resolve emissions at finer scales would require allowing emissions to vary across grid cells or
1059 subregions, supported by additional constraints. These constraints could include regional higher-resolution regional prior

inventories when available, as well as higher-resolution observations (e.g., GCAS) that can better resolve the urban variability in NO₂ as shown in this analysis.

8 Conclusion and Discussion

8.1 A GEO-constrained framework for anthropogenic NO_x emissions

Accurate urban NO_x emissions remain a major challenge for air quality modeling efforts, but geostationary satellites now offer a path forward. This work takes a novel approach in improving urban NO_x emissions using daytime GEO satellite observations. We quantify and reduce biases in modeled NO₂ over the Bangkok Metropolitan Region (BMR), by integrating GEMS constraints into a high-resolution model's daytime prior emission profile. We first used top-down inversions of hourly GEMS NO₂ columns with the Cross-Sectional Flux (CSF) method to develop an average daytime NO_x profile for the BMR in March 2024. Using this information, we developed and applied an optimization framework that incorporates physical constraints (i.e., with regards to emissions accumulation and lifetime) to reshape the WRF-Chem's daytime emission pattern and magnitude to better reflect observed emissions variability in the BMR.

This represents one of the first applications of the *ddeg* framework to estimate hourly urban NO_x emissions with geostationary observations in Southeast Asia. In contrast to a full chemical reanalysis, the *ddeg*-based framework provides an efficient and scalable alternative that does not require repeated model reinitialization of extensive chemical state optimization. This makes the approach particularly suitable for regional applications and for broader application across different modeling systems and urban environments within the domain of GEO sensors.

8.2 Model improvements across independent observational platforms

Re-running WRF-Chem (D01 – 20 km; D02 – 4 km) with an updated NO_x emission profile (WRF_{Updated}; WRF_{Updated+BC}) led to substantial improvements across multiple independent datasets. Model evaluation with ground monitors, Pandora, GCAS, and DC-8 observations consistently showed reduced biases and errors relative to the baseline simulation based on EDHAR v5 emissions. For example, surface-level comparisons with Thailand PCD ground network data confirmed some of these trends in WRF_{Updated}, with mean biases in NO₂ and NO_x decreasing from +12 - +14 ppbV in WRF_{Base} to roughly -3 ppbV in WRF_{Updated}, and 0.02 to 0.1 ppbV in WRF_{Updated+BC}. At the Bangkok Pandora site, mean bias shifted from strongly positive (+7.9 x 10¹⁵ molecules cm⁻²) to negative, and normalized mean errors decreased by ~20-~~42~~5% in WRF_{Updated} and WRF_{Updated+BC}. Evaluation against GCAS airborne column retrievals further showed that the emissions updates improved spatial variability and magnitude of NO₂ across the Bangkok urban plume, reducing mean and root mean square errors by ~~~55-63~~40% in WRF_{Updated} and WRF_{Updated+BC} compared to WRF_{Base}. The DC-8 in situ vertical profiles further illustrated that WRF_{Updated} could substantially reduce near-surface overestimation in morning hours and preserve the observed vertical structure of NO₂ mixing ratios.

1091

1092 **8.3 Assessing GEMS bias through multi-platform integration**

1093 Overall, these results demonstrate that incorporating geostationary satellite constraints into regional, high-resolution (4 km)
1094 chemical transport models can substantially improve the representation of urban air quality over Bangkok. Large biases in the
1095 baseline simulation are likely driven by reliance on outdated global emissions inventories (e.g., EDGAR v5), which do not
1096 reflect recent changes in regional anthropogenic activity, as well as uncertainties in bottom-up methodologies where updated
1097 local estimates appear systematically high. The satellite-constrained emission estimates derived here are consistent with
1098 independent top-down approaches (e.g., TCR-3) based on different satellite platforms and methodologies, increasing
1099 confidence in the inferred reductions.

1100 Comparisons with independent aircraft and ground-based observations further indicate that the GEMS-constrained emissions
1101 presented here may represent an underestimate. In particular, the systematic low bias reported for the GEMS v3 NO₂ product
1102 is consistent with the remaining negative biases observed in WRF_{Updated}. By accounting for this bias through the application of
1103 bias-corrected retrievals, WRF_{Updated+BC} reduces these negative biases, although in some cases introduces a tendency toward
1104 overprediction, highlighting tradeoffs associated with the correction. While model output (e.g., WRF_{Base}) can serve as a transfer
1105 standard for comparing different observing systems, these results highlight the importance of integrating ground-based,
1106 airborne, satellite, and model information to robustly identify biases and improve emission estimates. This bias could not be
1107 diagnosed using the satellite data alone. Instead, the integration of ground-based, airborne, satellite and model information
1108 together provides a powerful framework not only for improving emission estimations, but also for identifying limitations
1109 within individual observing systems.

1110 **8.4 Value of hourly GEO constraints, high-resolution modelling and future directions**

1111 A key strength of this framework is the use of hourly daytime constraints uniquely provided by geostationary observations,
1112 which enable direct characterization of daytime emission variability and plume evolution that cannot be captured by once-
1113 daily low-Earth-orbit measurements. These daytime constraints are particularly important for urban environments, where
1114 emissions, chemistry, and boundary-layer dynamics vary rapidly and strongly influence air quality impacts.

1115 Coarse (~12 km) simulations have been shown to inadequately represent circulations in coastal environments, and nonlinear
1116 NO_x chemistry, leading to systematic biases in simulations of NO₂ (Hsu et al., 2026; Valin et al., 2011; Verreyken et al., 2025;
1117 Yu et al., 2023). These limitations in model resolution are expected in coastal megacities such as Bangkok with complex local
1118 topography and land-sea contrasts. Consistent with recent TEMPO-based emission studies indicating that model resolution
1119 can limit the robustness of GEO-based top-down NO_x constraints (Hsu et al., 2026), these considerations motivate the use of

1120 4 km WRF-Chem simulations in this work as a necessary framework for accurately interpreting geostationary satellite
1121 observations and constraining urban NO_x emissions.

1122 While remaining discrepancies, including the negative model biases, are likely influenced in part by overpredicted model wind
1123 speeds and associated transport errors, future work could benefit from finer-resolution simulations (< 4 km) and more
1124 advanced urban parameterizations (e.g., multi-layer urban canopy models; Liu et al., (2025)) to better represent urban flow,
1125 drag, and mixing. Continued validation and further development of bias-corrected for updated GEMS retrievals will also
1126 strengthen the use of geostationary NO₂ products. Nevertheless, the high-frequency daytime sampling provided by GEMS
1127 already offers critical information for emission inversion, and the integration of GEMS-derived constraints into WRF-Chem
1128 represents a scalable pathway toward near-real-time, satellite-informed emissions estimation and improved air quality
1129 forecasting for rapidly developing megacities.

1130 **Code Availability.**

1131 The code repository for *ddeq v1* is available on GitLab: <https://gitlab.com/empa503/remote-sensing/ddeq>, [Kuhlmann, 2024a](#).
1132 The implementation of *ddeq v1* for top-down NO_x estimates and model optimization scripts are publicly available via Zenodo
1133 (<https://doi.org/10.5281/zenodo.18381169>).

1134 **Data Availability.**

1135 All ASIA-AQ field campaign data used in this study (i.e., GEMS NO₂ v3, NO_xO₃, CANOE, GCAS, Thailand PCD air quality
1136 monitoring data) are openly available and were acquired from their NASA Langley Research Center maintained archive:
1137 <https://www-air.larc.nasa.gov/cgi-bin/ArcView/asiaaq>. Pandora total column NO₂ observations are available through the
1138 Pandonia Global Network website: <https://www.pandonia-global-network.org/home/documents/pgn-data/>. ERA5
1139 meteorological reanalysis data were obtained from the Copernicus Climate Data Store: <https://cds.climate.copernicus.eu/>.
1140 Global emissions used in this study are openly available as well, HTAP v3.2 (https://edgar.jrc.ec.europa.eu/dataset_htap_v32),
1141 MIXv3.1(<https://csl.noaa.gov/groups/csl4/modeldata/data/Li2023/>), EDGARv5(https://edgar.jrc.ec.europa.eu/dataset_ghg50),
1142 ODIAC (<https://db.cger.nies.go.jp/dataset/ODIAC/>). THAI-KMUTT, and TCR-3 emissions can be made available upon
1143 request.

1144 **Supplement.**

1145 The supplement related to this article is available online.

1146 **Author Contributions**

1147 JAC designed the study, performed the model simulations, conducted the data analysis, prepared all figures, and wrote the
1148 initial draft of the manuscript. PS supervised the project, contributed ideas, guidance, and discussions regarding the model
1149 framework and interpretation of results. MM provided additional guidance on the modeling framework and interpretation of
1150 results. All authors discussed the results and contributed to the final version of the manuscript.

1151 **Competing Interests**

1152 At least one of the (co-)authors is a member of the editorial board of Atmospheric Chemistry and Physics.

1153 **Acknowledgements**

1154 We thank the entire ASIA-AQ team for their contributions to the field experiment. We extend our gratitude to the instrument
1155 teams for their efforts in conducting in situ measurements, to the airborne remote sensing teams (HSRL-2 and GCAS) for their
1156 data collection and support, and the GEMS team for providing the data utilized in this work. [We also thank Dr. Daniel Goldberg
1157 for helpful discussions related to top-down emissions estimation methodologies, including recommendations on the ddeg
1158 library and guidance on inversion methodology development.](#) The TCR-3 product was generated by calculations using the
1159 Earth Simulator with the support of the Japan Agency for Marine-Earth Science and Technology.

1160 **Financial Support**

1161 The funding for this research came from the National Aeronautics and Space Administration under awards 80NSSC22M0266
1162 and 80NSSC23K0786. [Additionally, part of this work was carried out at the Jet Propulsion Laboratory, California Institute of
1163 Technology, under contract to NASA \(80NM0018D0004The\).](#) The views expressed in this manuscript are those of the authors
1164 and do not reflect the views of NASA.

1165 **References**

1166

1167 Agarwal, P., Stevenson, D. S., and Heal, M. R.: Evaluation of WRF-Chem-simulated meteorology and aerosols over northern
1168 India during the severe pollution episode of 2016, *Atmospheric Chemistry and Physics*, 24, 2239–2266,
1169 <https://doi.org/10.5194/acp-24-2239-2024>, 2024.

1170 Ahmadov, R., McKeen, S. A., Robinson, A. L., Bahreini, R., Middlebrook, A. M., Gouw, J. A. de, Meagher, J., Hsie, E.-Y.,
1171 Edgerton, E., Shaw, S., and Trainer, M.: A volatility basis set model for summertime secondary organic aerosols over the
1172 eastern United States in 2006, <https://doi.org/10.1029/2011JD016831>, 2012.

1173 Anav, A., Sorrentino, B., Collalti, A., Paoletti, E., Sicard, P., Coulibaly, F., Manzini, J., Hoshika, Y., and De Marco, A.:
1174 Meteorological, chemical and biological evaluation of the coupled chemistry-climate WRF-Chem model from regional to
1175 urban scale. An impact-oriented application for human health, *Environmental Research*, 257, 119401,
1176 <https://doi.org/10.1016/j.envres.2024.119401>, 2024.

1177 Anenberg, S. C., Moheggh, A., Goldberg, D. L., Kerr, G. H., Brauer, M., Burkart, K., Hystad, P., Larkin, A., Wozniak, S., and
1178 Lamsal, L.: Long-term trends in urban NO₂ concentrations and associated paediatric asthma incidence: estimates from global
1179 datasets, *The Lancet Planetary Health*, 6, e49–e58, [https://doi.org/10.1016/S2542-5196\(21\)00255-2](https://doi.org/10.1016/S2542-5196(21)00255-2), 2022.

1180 ASIA-AQ White Paper | ASIA-AQ: https://espo.nasa.gov/asia-aq/document/ASIA-AQ_White_Paper, last access: 6 January
1181 2025.

1182 `minimize(method='SLSQP')` — SciPy v1.16.2 Manual: [https://docs.scipy.org/doc/scipy/reference/optimize.minimize-](https://docs.scipy.org/doc/scipy/reference/optimize.minimize-slsqp.html)
1183 `slsqp.html`, last access: 4 November 2025.

1184 Aung, S. H., Gheewala, S. H., Winijkul, E., Panyametheekul, S., and Prapasongsa, T.: Environmental impacts and costs of
1185 ozone formation in Bangkok Metropolitan Region, *Atmospheric Pollution Research*, 16, 102450,
1186 <https://doi.org/10.1016/j.apr.2025.102450>, 2025.

1187 Bae, K., Richter, A., Lange, K., Friedrich, M. M., Pinaridi, G., Roozendael, M. V., Merlaud, A., Fayt, C., Bösch, T., Zilker, B.,
1188 Latsch, M., Behrens, L. K., Lee, H., Jung, Y., Hong, H., Chang, L.-S., and Song, C.-K.: Comparison of GEMS v3.0
1189 tropospheric NO₂ columns with ground-based DOAS instruments in Ulsan, *GIScience & Remote Sensing*, 2025.

1190 Beirle, S., Boersma, K. F., Platt, U., Lawrence, M. G., and Wagner, T.: Megacity Emissions and Lifetimes of Nitrogen Oxides
1191 Probed from Space, *Science*, 333, 1737–1739, <https://doi.org/10.1126/science.1207824>, 2011.

1192 Bond, T. C., Streets, D. G., Yarber, K. F., Nelson, S. M., Woo, J.-H., and Klimont, Z.: A technology-based global inventory
1193 of black and organic carbon emissions from combustion, <https://doi.org/10.1029/2003JD003697>, 2004.

- 1194 Bond, T. C., Bhardwaj, E., Dong, R., Jogani, R., Jung, S., Roden, C., Streets, D. G., and Trautmann, N. M.: Historical emissions
1195 of black and organic carbon aerosol from energy-related combustion, 1850–2000, *Global Biogeochemical Cycles*, 21,
1196 <https://doi.org/10.1029/2006GB002840>, 2007.
- 1197 Chen, F. and Chen, Z.: Cost of economic growth: Air pollution and health expenditure, *Science of The Total Environment*,
1198 755, 142543, <https://doi.org/10.1016/j.scitotenv.2020.142543>, 2021.
- 1199 Cho, C., Franchin, A., Flocke, F., Lesko, K., Owen, C., Hall, S. R., Ullmann, K., Apel, E. C., Hills, A. J., Hornbrook, R. S.,
1200 Roozitalab, B., Jeong, D., Diskin, G. S., Choi, Y., DiGangi, J. P., Miech, J., Wolfe, G. M., Hanisco, T. F., St. Clair, J. M.,
1201 Liao, J., Delaria, E. R., Sebol, A., Hannun, R. A., Wennberg, P. O., Ball, K., Lee, Y. R., Huey, L. G., Tanner, D. J., Arterburn,
1202 L., Blake, D. R., Blake, N. J., Barletta, B., Meinardi, S., Min, K.-E., Kang, H., Nam, W., Wisthaler, A., Piel, F., Wojnowski,
1203 W., Dibb, J., and Crawford, J.: Insights on Ozone Formation Sensitivity in Southeast and East Asian Megacities during ASIA-
1204 AQ, *EGUosphere*, 1–29, <https://doi.org/10.5194/egusphere-2025-6434>, 2026.
- 1205 Choi, S., Lamsal, L. N., Follette-Cook, M., Joiner, J., Krotkov, N. A., Swartz, W. H., Pickering, K. E., Loughner, C. P., Appel,
1206 W., Pfister, G., Saide, P. E., Cohen, R. C., Weinheimer, A. J., and Herman, J. R.: Assessment of NO₂ observations during
1207 DISCOVER-AQ and KORUS-AQ field campaigns, *Atmospheric Measurement Techniques*, 13, 2523–2546,
1208 <https://doi.org/10.5194/amt-13-2523-2020>, 2020.
- 1209 Christopoulos, J. A., Saide, P. E., Ferrare, R., Collister, B., Barton-Grimley, R. A., Scarino, A. J., Collins, J., Hair, J. W., and
1210 Nehrir, A.: Improving Planetary Boundary Layer Height Estimation From Airborne Lidar Instruments, *Journal of Geophysical*
1211 *Research: Atmospheres*, 130, e2024JD042538, <https://doi.org/10.1029/2024JD042538>, 2025.
- 1212 Christopoulos, J.: GEMS Top-Down NO_x Emissions and Model Optimization, Zenodo,
1213 <https://doi.org/10.5281/zenodo.18381169>, 2026.
- 1214
- 1215 Commerce, N. C. for E. P. W. S. S. D. of: NCEP FNL Operational Model Global Tropospheric Analyses, continuing from
1216 July 1999, <https://doi.org/10.5065/D6M043C6>, 2000.
- 1217 Crippa, M., Solazzo, E., Huang, G., Guizzardi, D., Koffi, E., Muntean, M., Schieberle, C., Friedrich, R., and Janssens-
1218 Maenhout, G.: High resolution temporal profiles in the Emissions Database for Global Atmospheric Research, *Sci Data*, 7,
1219 121, <https://doi.org/10.1038/s41597-020-0462-2>, 2020.
- 1220 Elguindi, N., Granier, C., Stavrakou, T., Darras, S., Bauwens, M., Cao, H., Chen, C., Denier van der Gon, H. a. C., Dubovik,
1221 O., Fu, T. M., Henze, D. K., Jiang, Z., Keita, S., Kuenen, J. J. P., Kurokawa, J., Lioussse, C., Miyazaki, K., Müller, J.-F., Qu,
1222 Z., Solmon, F., and Zheng, B.: Intercomparison of Magnitudes and Trends in Anthropogenic Surface Emissions From Bottom-

- 1223 Up Inventories, Top-Down Estimates, and Emission Scenarios, *Earth's Future*, 8, e2020EF001520,
1224 <https://doi.org/10.1029/2020EF001520>, 2020.
- 1225 de Foy, B. and Schauer, J. J.: An improved understanding of NO_x emissions in South Asian megacities using TROPOMI NO₂
1226 retrievals, *Environ. Res. Lett.*, 17, 024006, <https://doi.org/10.1088/1748-9326/ac48b4>, 2022.
- 1227 Fuller, R., Landrigan, P. J., Balakrishnan, K., Bathan, G., Bose-O'Reilly, S., Brauer, M., Caravanos, J., Chiles, T., Cohen, A.,
1228 Corra, L., Cropper, M., Ferraro, G., Hanna, J., Hanrahan, D., Hu, H., Hunter, D., Janata, G., Kupka, R., Lanphear, B., Lichtveld,
1229 M., Martin, K., Mustapha, A., Sanchez-Triana, E., Sandilya, K., Schaeffli, L., Shaw, J., Seddon, J., Suk, W., Téllez-Rojo, M.
1230 M., and Yan, C.: Pollution and health: a progress update, *The Lancet Planetary Health*, 6, e535–e547,
1231 [https://doi.org/10.1016/S2542-5196\(22\)00090-0](https://doi.org/10.1016/S2542-5196(22)00090-0), 2022.
- 1232 Gao, Z. and Zhou, X.: A review of the CAMx, CMAQ, WRF-Chem and NAQPMS models: Application, evaluation and
1233 uncertainty factors, *Environmental Pollution*, 343, 123183, <https://doi.org/10.1016/j.envpol.2023.123183>, 2024.
- 1234 Georgoulias, A. K., van der A, R. J., Stammes, P., Boersma, K. F., and Eskes, H. J.: Trends and trend reversal detection in 2
1235 decades of tropospheric NO₂ satellite observations, *Atmospheric Chemistry and Physics*, 19, 6269–6294,
1236 <https://doi.org/10.5194/acp-19-6269-2019>, 2019.
- 1237 Goldberg, D. L., Lamsal, L. N., Loughner, C. P., Swartz, W. H., Lu, Z., and Streets, D. G.: A high-resolution and
1238 observationally constrained OMI NO₂ satellite retrieval, *Atmospheric Chemistry and Physics*, 17, 11403–11421,
1239 <https://doi.org/10.5194/acp-17-11403-2017>, 2017.
- 1240 Goldberg, D. L., Saide, P. E., Lamsal, L. N., de Foy, B., Lu, Z., Woo, J.-H., Kim, Y., Kim, J., Gao, M., Carmichael, G., and
1241 Streets, D. G.: A top-down assessment using OMI NO₂ suggests an underestimate in the NO_x emissions inventory in Seoul,
1242 South Korea, during KORUS-AQ, *Atmospheric Chemistry and Physics*, 19, 1801–1818, [https://doi.org/10.5194/acp-19-1801-](https://doi.org/10.5194/acp-19-1801-2019)
1243 2019, 2019.
- 1244 Goldberg, D. L., Tao, M., Kerr, G. H., Ma, S., Tong, D. Q., Fiore, A. M., Dickens, A. F., Adelman, Z. E., and Anenberg, S.
1245 C.: Evaluating the spatial patterns of U.S. urban NO_x emissions using TROPOMI NO₂, *Remote Sensing of Environment*, 300,
1246 113917, <https://doi.org/10.1016/j.rse.2023.113917>, 2024.
- 1247 Gong, S. L., Barrie, L. A., and Blanchet, J.-P.: Modeling sea-salt aerosols in the atmosphere: 1. Model development, *Journal*
1248 *of Geophysical Research: Atmospheres*, 102, 3805–3818, <https://doi.org/10.1029/96JD02953>, 1997.

- 1249 Graziosi, F. and Manca, G.: Quantification of Hotspot Methane Emissions Using Sentinel-5P TROPOMI Observations, JRC
1250 Publications Repository, <https://doi.org/10.2760/4473858>, 2025.
- 1251 Grell, G., Freitas, S. R., Stuefer, M., and Fast, J.: Inclusion of biomass burning in WRF-Chem: impact of wildfires on weather
1252 forecasts, *Atmospheric Chemistry and Physics*, 11, 5289–5303, <https://doi.org/10.5194/acp-11-5289-2011>, 2011.
- 1253 Guenther, A., Karl, T., Harley, P., Wiedinmyer, C., Palmer, P. I., and Geron, C.: Estimates of global terrestrial isoprene
1254 emissions using MEGAN (Model of Emissions of Gases and Aerosols from Nature), *Atmospheric Chemistry and Physics*, 6,
1255 3181–3210, <https://doi.org/10.5194/acp-6-3181-2006>, 2006.
- 1256 Guizzardi, D., Crippa, M., Butler, T., Keating, T., Wu, R., Kaminski, J., Kuenen, J., Kurokawa, J., Chatani, S., Morikawa, T.,
1257 Pouliot, G., Racine, J., Moran, M. D., Klimont, Z., Manseau, P. M., Mashayekhi, R., Henderson, B. H., Smith, S. J., Hoesly,
1258 R., Muntean, M., Banja, M., Schaaf, E., Pagani, F., Woo, J.-H., Kim, J., Pisoni, E., Zhang, J., Niemi, D., Sassi, M., Duhamel,
1259 A., Ansari, T., Foley, K., Geng, G., Chen, Y., and Zhang, Q.: The HTAP_v3.2 emission mosaic: merging regional and global
1260 monthly emissions (2000–2020) to support air quality modelling and policies, *Earth System Science Data*, 17, 5915–5950,
1261 <https://doi.org/10.5194/essd-17-5915-2025>, 2025.
- 1262 Gulde, S. T., Kolm, M. G., Smith, D. J., Maurer, R., Courrèges-Lacoste, G. B., Sallusti, M., and Bagnasco, G.: Sentinel 4: a
1263 geostationary imaging UVN spectrometer for air quality monitoring: status of design, performance and development, in:
1264 *International Conference on Space Optics — ICSO 2014*, *International Conference on Space Optics — ICSO 2014*, 1158–
1265 1166, <https://doi.org/10.1117/12.2304099>, 2017.
- 1266 Hakkarainen, J., Nurmela, J., and Lindqvist, H.: D4.4 Benchmarking of plume detection and quantification methods, 2023.
- 1267 Hakkarainen, J., Kuhlmann, G., Koene, E., Santaren, D., Meier, S., Krol, M. C., van Stratum, B. J. H., Ialongo, I., Chevallier,
1268 F., Tamminen, J., Brunner, D., and Broquet, G.: Analyzing nitrogen dioxide to nitrogen oxide scaling factors for data-driven
1269 satellite-based emission estimation methods: A case study of Matimba/Medupi power stations in South Africa, *Atmospheric
1270 Pollution Research*, 15, 102171, <https://doi.org/10.1016/j.apr.2024.102171>, 2024.
- 1271 Hoesly, R. M., Smith, S. J., Feng, L., Klimont, Z., Janssens-Maenhout, G., Pitkanen, T., Seibert, J. J., Vu, L., Andres, R. J.,
1272 Bolt, R. M., Bond, T. C., Dawidowski, L., Kholod, N., Kurokawa, J., Li, M., Liu, L., Lu, Z., Moura, M. C. P., O’Rourke, P.
1273 R., and Zhang, Q.: Historical (1750–2014) anthropogenic emissions of reactive gases and aerosols from the Community
1274 Emissions Data System (CEDS), *Geoscientific Model Development*, 11, 369–408, <https://doi.org/10.5194/gmd-11-369-2018>,
1275 2018.

1276 Hsu, C.-H., Henze, D. K., Mizzi, A. P., Harkins, C., Lyu, C., Cooper, O. R., Schwantes, R. H., He, J., Li, M., Wang, S.,
1277 Stockwell, C. E., Warneke, C., Rollins, A. W., Waxman, E. M., Zuraski, K., Peischl, J., Kondragunta, S., Li, F., Xu, C., Pierce,
1278 R. B., Abad, G. G., Nowlan, C. R., Liu, X., and McDonald, B. C.: Top-Down Estimates of U.S. NO_x Emissions Using TEMPO
1279 and TROPOMI NO₂ Remote Sensing Observations With WRF-Chem/Chem-DART, *Journal of Geophysical Research:*
1280 *Atmospheres*, 131, e2025JD044223, <https://doi.org/10.1029/2025JD044223>, 2026.

1281 Inness, A., Ades, M., Agustí-Panareda, A., Barré, J., Benedictow, A., Blechschmidt, A.-M., Dominguez, J. J., Engelen, R.,
1282 Eskes, H., Flemming, J., Huijnen, V., Jones, L., Kipling, Z., Massart, S., Parrington, M., Peuch, V.-H., Razinger, M., Remy,
1283 S., Schulz, M., and Suttie, M.: The CAMS reanalysis of atmospheric composition, *Atmospheric Chemistry and Physics*, 19,
1284 3515–3556, <https://doi.org/10.5194/acp-19-3515-2019>, 2019.

1285 Janz, S. J., Kowalewski, M., Lamsal, L., Nowlan, C., and Judd, L.: Airborne hyperspectral trace gas sensors as testbeds for
1286 geostationary air quality missions, in: *Sensors, Systems, and Next-Generation Satellites XXIII*, *Sensors, Systems, and Next-*
1287 *Generation Satellites XXIII*, 509–518, <https://doi.org/10.1117/12.2533765>, 2019.

1288 Jiawei Zhuang, raphael dussin, David Huard, Pascal Bourgault, Anderson Banihirwe, Stephane Raynaud, Brewster Malevich,
1289 Martin Schupfner, Filipe, Charles Gauthier, Sam Levang, André Jüling, Mattia Almansì, RichardScottOZ, RondeauG, Stephan
1290 Rasp, Trevor James Smith, Ben Mares, Jemma Stachelek, Matthew Plough, Pierre, Ray Bell, Romain Caneill, and Xianxiang
1291 Li: pangeo-data/xESMF: v0.8.10, , <https://doi.org/10.5281/ZENODO.4294774>, 2025.

1292 Judd, L. M., Al-Saadi, J. A., Szykman, J. J., Valin, L. C., Janz, S. J., Kowalewski, M. G., Eskes, H. J., Veefkind, J. P., Cede,
1293 A., Mueller, M., Gebetsberger, M., Swap, R., Pierce, R. B., Nowlan, C. R., Abad, G. G., Nehrir, A., and Williams, D.:
1294 Evaluating Sentinel-5P TROPOMI tropospheric NO₂ column densities with airborne and Pandora spectrometers near New
1295 York City and Long Island Sound, *Atmospheric Measurement Techniques*, 13, 6113–6140, [https://doi.org/10.5194/amt-13-](https://doi.org/10.5194/amt-13-6113-2020)
1296 [6113-2020](https://doi.org/10.5194/amt-13-6113-2020), 2020.

1297 Jung, Y., Park, J., Hong, H., Lee, H., and Jeong, U.: Evaluation of GEMS NO Retrieval Algorithm Version 2.0 and 3.0 Using
1298 TROPOMI and Pandora Observations, *Korean Journal of Remote Sensing*, 41, 803–811,
1299 <https://doi.org/10.7780/kjrs.2025.41.5.8>, 2025.

1300 Kim, J., Jeong, U., Ahn, M.-H., Kim, J. H., Park, R. J., Lee, H., Song, C. H., Choi, Y.-S., Lee, K.-H., Yoo, J.-M., Jeong, M.-
1301 J., Park, S. K., Lee, K.-M., Song, C.-K., Kim, S.-W., Kim, Y. J., Kim, S.-W., Kim, M., Go, S., Liu, X., Chance, K., Miller, C.
1302 C., Al-Saadi, J., Veihelmann, B., Bhartia, P. K., Torres, O., Abad, G. G., Haffner, D. P., Ko, D. H., Lee, S. H., Woo, J.-H.,
1303 Chong, H., Park, S. S., Nicks, D., Choi, W. J., Moon, K.-J., Cho, A., Yoon, J., Kim, S., Hong, H., Lee, K., Lee, H., Lee, S.,
1304 Choi, M., Veefkind, P., Levelt, P. F., Edwards, D. P., Kang, M., Eo, M., Bak, J., Baek, K., Kwon, H.-A., Yang, J., Park, J.,
1305 Han, K. M., Kim, B.-R., Shin, H.-W., Choi, H., Lee, E., Chong, J., Cha, Y., Koo, J.-H., Irie, H., Hayashida, S., Kasai, Y.,

1306 Kanaya, Y., Liu, C., Lin, J., Crawford, J. H., Carmichael, G. R., Newchurch, M. J., Lefter, B. L., Herman, J. R., Swap, R. J.,
1307 Lau, A. K. H., Kurosu, T. P., Jaross, G., Ahlers, B., Dobber, M., McElroy, C. T., and Choi, Y.: New Era of Air Quality
1308 Monitoring from Space: Geostationary Environment Monitoring Spectrometer (GEMS), <https://doi.org/10.1175/BAMS-D-18->
1309 0013.1, 2020.

1310 Koster, R. D., Darmenov, A. S., and da Silva, A. M.: The Quick Fire Emissions Dataset (QFED): Documentation of Versions
1311 2.1, 2.2 and 2.4: Technical Report Series on Global Modeling and Data Assimilation - Volume 38, 2015.

1312 Kowalewski, M. G. and Janz, S. J.: Remote sensing capabilities of the GeoCAPE Airborne Simulator, in: Earth Observing
1313 Systems XIX, Earth Observing Systems XIX, 496–507, <https://doi.org/10.1117/12.2062058>, 2014.

1314 Kuhlmann, G., Koene, E., Meier, S., Santaren, D., Broquet, G., Chevallier, F., Hakkarainen, J., Nurmela, J., Amorós, L.,
1315 Tamminen, J., and Brunner, D.: The *ddeg* Python library for point source quantification from remote sensing images (version
1316 1.0), Geoscientific Model Development, 17, 4773–4789, <https://doi.org/10.5194/gmd-17-4773-2024>, 2024.

1317 Kumar, R., Naja, M., Pfister, G. G., Barth, M. C., Wiedinmyer, C., and Brasseur, G. P.: Simulations over South Asia using the
1318 Weather Research and Forecasting model with Chemistry (WRF-Chem): chemistry evaluation and initial results, Geoscientific
1319 Model Development, 5, 619–648, <https://doi.org/10.5194/gmd-5-619-2012>, 2012.

1320 Kurokawa, J. and Ohara, T.: Long-term historical trends in air pollutant emissions in Asia: Regional Emission inventory in
1321 ASia (REAS) version 3, Atmospheric Chemistry and Physics, 20, 12761–12793, <https://doi.org/10.5194/acp-20-12761-2020>,
1322 2020.

1323 Lee, S., Bae, K., Janz, S. J., Judd, L. M., Xiong, S., Boehmler, J., Jung, Y., Lee, H.-J., Hong, H., Chang, L.-S., Kang, M., Ahn,
1324 M.-H., Song, C.-K., and Park, S. S.: Sensitivity analysis of NO₂ differential slant column density according to spatial resolution
1325 using GCAS data from the SIJAQ 2022 campaign, Atmospheric Environment, 335, 120723,
1326 <https://doi.org/10.1016/j.atmosenv.2024.120723>, 2024.

1327 Lennartson, E. M., Wang, J., Gu, J., Castro Garcia, L., Ge, C., Gao, M., Choi, M., Saide, P. E., Carmichael, G. R., Kim, J., and
1328 Janz, S. J.: Diurnal variation of aerosol optical depth and PM_{2.5} in South Korea: a synthesis from AERONET, satellite (GOCI),
1329 KORUS-AQ observation, and the WRF-Chem model, Atmospheric Chemistry and Physics, 18, 15125–15144,
1330 <https://doi.org/10.5194/acp-18-15125-2018>, 2018.

1331 Li, M., Kurokawa, J., Zhang, Q., Woo, J.-H., Morikawa, T., Chatani, S., Lu, Z., Song, Y., Geng, G., Hu, H., Kim, J., Cooper,
1332 O. R., and McDonald, B. C.: MIXv2: a long-term mosaic emission inventory for Asia (2010–2017), Atmospheric Chemistry
1333 and Physics, 24, 3925–3952, <https://doi.org/10.5194/acp-24-3925-2024>, 2024.

- 1334 Liu, J., Gao, H., Jia, R., Wang, R., Han, D., Liu, L., Xu, X., and Qiao, Z.: A downscaling framework with WRF-UCM and
1335 LES/RANS models for urban microclimate simulation strategy: Validation through both measurement and mechanism model,
1336 *Building and Environment*, 269, 112361, <https://doi.org/10.1016/j.buildenv.2024.112361>, 2025.
- 1337 Makkwao, K. and Prueksasit, T.: PM10 Concentration Emitted from Blasting and Crushing Processes of Limestone Mines in
1338 Saraburi Province, Thailand, 2021.
- 1339 Meier, S., Koene, E. F. M., Krol, M., Brunner, D., Damm, A., and Kuhlmann, G.: A lightweight NO₂-to-NO_x conversion model
1340 for quantifying NO_x emissions of point sources from NO₂ satellite observations, *Atmospheric Chemistry and Physics*, 24,
1341 7667–7686, <https://doi.org/10.5194/acp-24-7667-2024>, 2024.
- 1342 Miyazaki, K., Eskes, H., Sudo, K., Boersma, K. F., Bowman, K., and Kanaya, Y.: Decadal changes in global surface NO_x
1343 emissions from multi-constituent satellite data assimilation, *Atmospheric Chemistry and Physics*, 17, 807–837,
1344 <https://doi.org/10.5194/acp-17-807-2017>, 2017.
- 1345 Miyazaki, K., Sekiya, T., Fu, D., Bowman, K. W., Kulawik, S. S., Sudo, K., Walker, T., Kanaya, Y., Takigawa, M., Ogochi,
1346 K., Eskes, H., Boersma, K. F., Thompson, A. M., Gaubert, B., Barre, J., and Emmons, L. K.: Balance of Emission and
1347 Dynamical Controls on Ozone During the Korea-United States Air Quality Campaign From Multiconstituent Satellite Data
1348 Assimilation, *Journal of Geophysical Research: Atmospheres*, 124, 387–413, <https://doi.org/10.1029/2018JD028912>, 2019.
- 1349 Miyazaki, K., Bowman, K., Sekiya, T., Eskes, H., Boersma, F., Worden, H., Livesey, N., Payne, V. H., Sudo, K., Kanaya, Y.,
1350 Takigawa, M., and Ogochi, K.: Updated tropospheric chemistry reanalysis and emission estimates, TCR-2, for 2005–2018,
1351 *Earth System Science Data*, 12, 2223–2259, <https://doi.org/10.5194/essd-12-2223-2020>, 2020.
- 1352 Mues, A., Kuenen, J., Hendriks, C., Manders, A., Segers, A., Scholz, Y., Hueglin, C., Builtjes, P., and Schaap, M.: Sensitivity
1353 of air pollution simulations with LOTOS-EUROS to the temporal distribution of anthropogenic emissions, *Atmospheric*
1354 *Chemistry and Physics*, 14, 939–955, <https://doi.org/10.5194/acp-14-939-2014>, 2014.
- 1355 Nocedal, J. and Wright, S. J.: *Numerical optimization*, 2nd ed., Springer, New York, 664 pp., 2006.
- 1356 Oda, T., Maksyutov, S., and Andres, R. J.: The Open-source Data Inventory for Anthropogenic CO₂ , version 2016
1357 (ODIAC2016): a global monthly fossil fuel CO₂ gridded emissions data product for tracer transport simulations and surface
1358 flux inversions, *Earth Syst. Sci. Data*, 10, 87–107, <https://doi.org/10.5194/essd-10-87-2018>, 2018.

- 1359 Park, J., Choi, Y., Jung, J., Lee, K., and Yeganeh, A. K.: First top-down diurnal adjustment to NO_x emissions inventory in
1360 Asia informed by the Geostationary Environment Monitoring Spectrometer (GEMS) tropospheric NO₂ columns, *Sci Rep*, 14,
1361 24338, <https://doi.org/10.1038/s41598-024-76223-1>, 2024.
- 1362 Park, J., Hong, H., Lee, H., Kim, S.-W., Kim, J., Van Roozendaal, M., Fayt, C., Ahn, M.-H., Jacob, D. J., Seo, S., Kim, K.-
1363 M., Kim, D., Choi, W., Lee, W.-J., Lee, D.-W., Wagner, T., Richter, A., Krotkov, N. A., Lamsal, L. N., Ko, D. H., Lee, S. H.,
1364 and Woo, J.-H.: Tropospheric nitrogen dioxide levels vary diurnally in Asian cities, *Commun Earth Environ*, 6, 389,
1365 <https://doi.org/10.1038/s43247-025-02272-7>, 2025.
- 1366 Park, R. J., Oak, Y. J., Emmons, L. K., Kim, C.-H., Pfister, G. G., Carmichael, G. R., Saide, P. E., Cho, S.-Y., Kim, S., Woo,
1367 J.-H., Crawford, J. H., Gaubert, B., Lee, H.-J., Park, S.-Y., Jo, Y.-J., Gao, M., Tang, B., Stanier, C. O., Shin, S. S., Park, H.
1368 Y., Bae, C., and Kim, E.: Multi-model intercomparisons of air quality simulations for the KORUS-AQ campaign, *Elementa:
1369 Science of the Anthropocene*, 9, 00139, <https://doi.org/10.1525/elementa.2021.00139>, 2021.
- 1370 Pörtner, H.-O., Roberts, D. C., Tignor, M. M. B., Poloczanska, E. S., Mintenbeck, K., Alegría, A., Craig, M., Langsdorf, S.,
1371 Lösche, S., Möller, V., Okem, A., and Rama, B. (Eds.): *Climate Change 2022: Impacts, Adaptation and Vulnerability.*
1372 *Contribution of Working Group II to the Sixth Assessment Report of the Intergovernmental Panel on Climate Change.*, 2022.
- 1373 Rey-Pommier, A., Héraud, A., Chevallier, F., Ciais, P., Christoudias, T., Kushta, J., and Sciare, J.: Global gridded NO_x
1374 emissions using TROPOMI observations, *Earth System Science Data*, 17, 3329–3351, [https://doi.org/10.5194/essd-17-3329-
1375 2025](https://doi.org/10.5194/essd-17-3329-2025), 2025.
- 1376 Ridley, B. A. and Grahek, F. E.: A Small, Low Flow, High Sensitivity Reaction Vessel for NO Chemiluminescence Detectors,
1377 1990.
- 1378 Ridley, B. A., Grahek, F. E., and Walega, J. G.: A Small High-Sensitivity, Medium-Response Ozone Detector Suitable for
1379 Measurements from Light Aircraft, 1992.
- 1380 Saide, P. E., Gao, M., Lu, Z., Goldberg, D. L., Streets, D. G., Woo, J.-H., Beyersdorf, A., Corr, C. A., Thornhill, K. L.,
1381 Anderson, B., Hair, J. W., Nehrir, A. R., Diskin, G. S., Jimenez, J. L., Nault, B. A., Campuzano-Jost, P., Dibb, J., Heim, E.,
1382 Lamb, K. D., Schwarz, J. P., Perring, A. E., Kim, J., Choi, M., Holben, B., Pfister, G., Hodzic, A., Carmichael, G. R., Emmons,
1383 L., and Crawford, J. H.: Understanding and improving model representation of aerosol optical properties for a Chinese haze
1384 event measured during KORUS-AQ, *Atmospheric Chemistry and Physics*, 20, 6455–6478, [https://doi.org/10.5194/acp-20-
1385 6455-2020](https://doi.org/10.5194/acp-20-6455-2020), 2020.

- 1386 Santaren, D., Hakkarainen, J., Kuhlmann, G., Koene, E., Chevallier, F., Ialongo, I., Lindqvist, H., Nurmela, J., Tamminen, J.,
1387 Amorós, L., Brunner, D., and Broquet, G.: Benchmarking data-driven inversion methods for the estimation of local CO₂
1388 emissions from synthetic satellite images of XCO₂ and NO₂, *Atmospheric Measurement Techniques*, 18, 211–239,
1389 <https://doi.org/10.5194/amt-18-211-2025>, 2025.
- 1390 Seinfeld and Pandis: *Atmospheric Chemistry and Physics: From Air Pollution to Climate Change*, 3rd Edition | Wiley, 2016.
- 1391 Shetty, S. S., D, D., S, H., Sonkusare, S., Naik, P. B., N, S. K., and Madhyastha, H.: Environmental pollutants and their effects
1392 on human health, *Heliyon*, 9, <https://doi.org/10.1016/j.heliyon.2023.e19496>, 2023.
- 1393 Sicard, P., Agathokleous, E., Anenberg, S. C., De Marco, A., Paoletti, E., and Calatayud, V.: Trends in urban air pollution
1394 over the last two decades: A global perspective, *Science of The Total Environment*, 858, 160064,
1395 <https://doi.org/10.1016/j.scitotenv.2022.160064>, 2023.
- 1396 Skamarock, W. C., Klemp, J. B., Dudhia, J., Gill, D. O., Liu, Z., Berner, J., Wang, W., Powers, J. G., Duda, M. G., Barker, D.
1397 M., and Huang, X.-Y.: A Description of the Advanced Research WRF Model Version 4, <https://doi.org/10.5065/1DFH-6P97>,
1398 2019.
- 1399 Smith, S. J., van Aardenne, J., Klimont, Z., Andres, R. J., Volke, A., and Delgado Arias, S.: Anthropogenic sulfur dioxide
1400 emissions: 1850–2005, *Atmospheric Chemistry and Physics*, 11, 1101–1116, <https://doi.org/10.5194/acp-11-1101-2011>, 2011.
- 1401 St. Clair, J. M., Swanson, A. K., Bailey, S. A., and Hanisco, T. F.: CAFE: a new, improved nonresonant laser-induced
1402 fluorescence instrument for airborne in situ measurement of formaldehyde, *Atmospheric Measurement Techniques*, 12, 4581–
1403 4590, <https://doi.org/10.5194/amt-12-4581-2019>, 2019.
- 1404 Thailand Office of the National Economic and Social Development Board, World Bank: *Industrial Change in the Bangkok
1405 Urban Region*, 2017.
- 1406 Tuccella, P., Curci, G., Grell, G. A., Visconti, G., Crumeyrolle, S., Schwarzenboeck, A., and Mensah, A. A.: A new chemistry
1407 option in WRF-Chem v. 3.4 for the simulation of direct and indirect aerosol effects using VBS: evaluation against IMPACT-
1408 EUCAARI data, *Geoscientific Model Development*, 8, 2749–2776, <https://doi.org/10.5194/gmd-8-2749-2015>, 2015.
- 1409 Uttamang, P., Aneja, V. P., and Hanna, A. F.: Assessment of gaseous criteria pollutants in the Bangkok Metropolitan Region,
1410 Thailand, *Atmospheric Chemistry and Physics*, 18, 12581–12593, <https://doi.org/10.5194/acp-18-12581-2018>, 2018.

1411 Uttamang, P., Campbell, P. C., Aneja, V. P., and Hanna, A. F.: A multi-scale model analysis of ozone formation in the Bangkok
1412 Metropolitan Region, Thailand, *Atmospheric Environment*, 229, 117433, <https://doi.org/10.1016/j.atmosenv.2020.117433>,
1413 2020.

1414 Uttamang, P., Choomanee, P., Phupijit, J., Bualert, S., and Thongyen, T.: Investigation of Secondary Organic Aerosol
1415 Formation during O₃ and PM_{2.5} Episodes in Bangkok, Thailand, *Atmosphere*, 14, 994,
1416 <https://doi.org/10.3390/atmos14060994>, 2023.

1417 Valin, L. C., Russell, A. R., Hudman, R. C., and Cohen, R. C.: Effects of model resolution on the interpretation of satellite
1418 NO₂ observations, *Atmospheric Chemistry and Physics*, 11, 11647–11655, <https://doi.org/10.5194/acp-11-11647-2011>, 2011.

1419 Verreyken, B. W. D., Harkins, C., Li, M., Angevine, W., Stockwell, C. E., Xu, L., Coggon, M., Gilman, J., Warneke, C.,
1420 Strobach, E., Brown, S., McCarty, B., Marchbanks, R., Baidar, S., Brewer, A., Pfannerstill, E. Y., Arata, C., Goldstein, A. H.,
1421 Brioude, J., and McDonald, B. C.: Top-Down Evaluation of Volatile Chemical Product Emissions Using a Lagrangian
1422 Framework, *Environ. Sci. Technol.*, 59, 7211–7221, <https://doi.org/10.1021/acs.est.4c10117>, 2025.

1423 Ye, J., Liu, L., Wang, Q., Hu, S., and Li, S.: A Novel Machine Learning Algorithm for Planetary Boundary Layer Height
1424 Estimation Using AERI Measurement Data, *IEEE Geoscience and Remote Sensing Letters*, 19,
1425 <https://doi.org/10.1109/lgrs.2021.3073048>, 2021.

1426 Yu, K. A., Li, M., Harkins, C., He, J., Zhu, Q., Verreyken, B., Schwantes, R. H., Cohen, R. C., McDonald, B. C., and Harley,
1427 R. A.: Improved Spatial Resolution in Modeling of Nitrogen Oxide Concentrations in the Los Angeles Basin, *Environ. Sci.*
1428 *Technol.*, 57, 20689–20698, <https://doi.org/10.1021/acs.est.3c06158>, 2023.

1429 Zhao, C., Liu, X., Leung, L. R., Johnson, B., McFarlane, S. A., Gustafson, W. I. J., Fast, J. D., and Easter, R.: The spatial
1430 distribution of mineral dust and its shortwave radiative forcing over North Africa: modeling sensitivities to dust emissions and
1431 aerosol size treatments, *Atmospheric Chemistry and Physics*, 10, 8821–8838, <https://doi.org/10.5194/acp-10-8821-2010>, 2010.

1432 Zoogman, P., Liu, X., Suleiman, R. M., Pennington, W. F., Flittner, D. E., Al-Saadi, J. A., Hilton, B. B., Nicks, D. K.,
1433 Newchurch, M. J., Carr, J. L., Janz, S. J., Andraschko, M. R., Arola, A., Baker, B. D., Canova, B. P., Chan Miller, C., Cohen,
1434 R. C., Davis, J. E., Dussault, M. E., Edwards, D. P., Fishman, J., Ghulam, A., González Abad, G., Grutter, M., Herman, J. R.,
1435 Houck, J., Jacob, D. J., Joiner, J., Kerridge, B. J., Kim, J., Krotkov, N. A., Lamsal, L., Li, C., Lindfors, A., Martin, R. V.,
1436 McElroy, C. T., McLinden, C., Natraj, V., Neil, D. O., Nowlan, C. R., O'Sullivan, E. J., Palmer, P. I., Pierce, R. B., Pippin, M.
1437 R., Saiz-Lopez, A., Spurr, R. J. D., Szykman, J. J., Torres, O., Veeffkind, J. P., Veihelmann, B., Wang, H., Wang, J., and
1438 Chance, K.: Tropospheric emissions: Monitoring of pollution (TEMPO), *Journal of Quantitative Spectroscopy and Radiative*
1439 *Transfer*, 186, 17–39, <https://doi.org/10.1016/j.jqsrt.2016.05.008>, 2017.

1440

1441

1442

1443

1444